AN APPROXIMATE MODEL FOR THE PERFORMANCE AND ACOUSTIC PREDICTIONS OF COUNTERROTATING PROPELLER CONFIGURATIONS

A Thesis

by

BRETT WILLIAM DENNER

Submitted to the Office of Graduate Studies of
Texas A&M University
in partial fulfillment of the requirements for the degree of

MASTER OF SCIENCE

December 1989

Major Subject: Aerospace Engineering

AN APPROXIMATE MODEL FOR THE PERFORMANCE AND ACOUSTIC PREDICTIONS OF COUNTERROTATING PROPELLER CONFIGURATIONS

A Thesis

by

BRETT WILLIAM DENNER

Submitted to the Office of Graduate Studies of
Texas A&M University
in partial fulfillment of the requirements for the degree of

MASTER OF SCIENCE

December 1989

Major Subject: Aerospace Engineering

AN APPROXIMATE MODEL FOR THE PERFORMANCE AND ACOUSTIC PREDICTIONS OF COUNTERROTATING PROPELLER CONFIGURATIONS

A Thesis

by

BRETT WILLIAM DENNER

Approved as to style and content by:

Kenneth D. Korkan
(Chair of Committee)

Anwar Ahmed
(Member)

David L. Rhode
(Member)

Walter E. Haisler
(Head of Department)

December 1989

ABSTRACT

An Approximate Model for the Performance and Acoustic Predictions
of Counterrotating Propeller Configurations. (December 1989)
Brett William Denner, B.S., Texas A&M University
Chair of Advisory Committee: Dr. Kenneth D. Korkan

An approximate method was developed to analyze and predict the acoustics of a counterrotating propeller configuration. The method employs the analytical techniques of Lock and Theodorsen as described by Davidson to predict the steady performance of a counterrotating configuration. Then, a modification of the method of Lesieutre is used to predict the unsteady forces on the blades. Finally, the steady and unsteady loads are used in the numerical method of Succi to predict the unsteady acoustics of the propeller. The numerical results are compared with experimental acoustic measurements of a counterrotating propeller configuration by Gazzaniga operating under several combinations of advance ratio, blade pitch, and number of blades. In addition, a constant-speed commuter-class propeller configuration was designed with the Davidson method and the acoustics analyzed at three advance ratios. Noise levels and frequency spectra were calculated at a number of locations around the configuration. The directivity patterns of the harmonics in both the horizontal and vertical planes were examined, with the conclusion that the noise levels of the even harmonics are relatively independent of direction whereas the noise levels of the odd harmonics are extremely dependent on azimuthal direction in the horizontal plane. The equations of Succi are examined to explain this behavior.

To my family, for their love and encouragement.

ACKNOWLEDGMENT

The author would like to thank Dr. K.D. Korkan for his assistance and guidance throughout my graduate career. Thanks also to Drs. Ahmed and Rhode for their interest in this research and to Mr. J.A. Gazzaniga for the use of his experimental data. This research was sponsored by NASA Lewis Research Center Grant NAG 3-354. Thanks are extended to Drs. Groeneweg and Dittmar at NASA Lewis Research Center for funding and supporting my education and research.

NOMENCLATURE

a, b, c	see Eq. (38)
a_0	sonic velocity
A_n	Fourier cosine coefficients
b	see Eq. (16)
B	number of propeller blades
B_n	Fourier sine coefficients
c	blade chord
C_D	section drag coefficient
$C(k)_{\text{cir}}$	circulatory component of Theodorsen function
C_L	section lift coefficient
C_{L_D}	design lift coefficient
C_{L_g}	unsteady lift coefficient due to sinusoidal gust n
$C_{L_{g,\text{osc}}}$	general unsteady lift coefficient due to gust
C_{L_n}	Fourier Series component of unsteady lift coefficient
$C_{L_{\text{QS}}}$	quasi-steady lift coefficient
C_{L_α}	lift curve slope
C_n	Fourier coefficient (see Eq. (65))
CRPTR	Counterrotating Propeller Test Rig
D	propeller diameter
f	position of body surface at time τ
$\vec{F}_i$	net force on medium due to pressure on surface of source

F_Q	torque force on source; acts opposite to velocity of source
F_T	thrust force on source; acts in flight direction of propeller
$H(f)$	Heaviside function of body surface
$\hat{\imath}, \hat{\jmath}, \hat{k}$	Cartesian unit vectors
i	$\sqrt{-1}$
I	see Eq. (37)
J	advance ratio, V_∞/nD
J_n	Bessel function of the first kind of order n
k	reduced frequency, $\omega c/2V_\infty$
k'	Betz coefficient; number with same value at all blade sections
$K(r_c)$	circulation function used by Theodorsen
l	length of vortex
l_i	aerodynamic force per unit area on fluid at body surface
L_g	lift due to sinusoidally oscillating vertical gust
M	Mach number
$\vec{M}_i$	source Mach number, $(\partial\tilde{y}/\partial\tau)/a_0$
M_n	local normal component of Mach number
$\dot{M}_n$	time derivative of M_n
M_r	relative Mach number between source and observer
$\dot{M}_r$	time derivative of M_r
M_R	radial component of Mach number
$\vec{M}_t$	local tangential component of Mach number
n	blade rotation speed (rev/sec); harmonic number; summation index

n_i	surface normal
n_M	component of surface normal in Mach number direction
$\dot{n}_M$	time derivative of n_M
n_r	component of surface normal in $\hat{r}$ direction
$\dot{n}_r$	time derivative of n_r
N	number of compact acoustic sources
OASPL	Overall Sound Pressure Level; see Eq. (68)
p	pressure minus the mean pressure (acoustic pressure)
p', q', r', s'	elementary functions of propeller parameters and functions (see Eq. (12))
p_{ij}	pressure tensor minus the mean pressure
dP	power absorbed by blade elements
p_{L_n}	loading noise pressure
P_n	pressure amplitude of nth harmonic
P_{ref}	reference pressure, 20 μ Pa
P_{rms}	root-mean-square of acoustic pressure
p_{T_n}	thickness noise pressure
q	dynamic pressure, $\frac{1}{2}\rho_0 V_\infty^2$
Q	torque
dQ	torque on blade elements
Q_F	torque-force; $Q_F = Q/r$
r	radial coordinate; distance between between the source at $\tilde{y}$ and observer at $\tilde{x}$
$\tilde{r}$	vector from source to observer

r_c	r/R_{tip}
r_i	radius of helical vortex
$\hat{r}_i$	unit vector from source to observer
r_j	radial coordinate of field point
R	radius of rotation of acoustic source; distance from source to observer in Eq. 1
$\vec{R}_{ijk}$	distance from field point to point on vortex
R_{tip}	propeller tip radius
RPM	revolutions per minute
S	body surface area
dS	incremental surface area of blade element
S_c	control surface
SPL	Sound Pressure Level of harmonic
t	time
$(t/c)_{\text{max}}$	maximum blade thickness-to-chord radio
T	blade passing period
dT	thrust on blade elements
T_{ij}	Lighthill stress tensor
T_L	blade loading period
$\vec{v}_{ijk}$	total induced velocity
dV	incremental volume of blade element
V_n	velocity component normal to surface

u, v	components of interference velocity of front propeller on back propeller or back propeller on front propeller (Fig. 1)
u_i	fluid velocity
u_1, u_2, u_3	induced velocity components
v_i	source surface velocity
$\vec{v}_{ijk}$	induced velocity vector
V_∞	flight velocity
$\mathcal{V}(\tau)$	volume of source
$\bar{w}$	$= W/V$
W	resultant velocity at blade elements
W_0	amplitude of gust; W for light loading limit (Fig. 2)
w_1	interference velocity at either propeller on itself
$W_g(t)$	vertical velocity due to sinusoidal gust
$W_{\text{gust}}(t)$	vertical velocity due to general gust
x, y, z	coordinate axes
$x(\theta'), y(\theta'), z(\theta')$	coordinates of helical vortex
$\tilde{x}$	vector to observer
$x', y', z',$	coordinates of field point
X_0	Lock's tip loss factor (see Eq. (11))
x_L, y_L, z_L	coordinates of inner end of bound vortex segment
x_o, y_o, z_o	coordinates of observer
x_T, y_T, z_T	coordinates of outer end of bound vortex segment
$\tilde{y}$	vector to source

Y_n	Bessel function of the second kind of order n
Z_i	axial coordinate of disk plane of either propeller
z_j	axial field point location
α	section angle of attack
β	total induced angle (see Eq. (15))
Γ	circulation strength of vortex
Γ_i	circulation strength of elemental vortex
δ	Dirac delta function
δ_{ij}	Kroneker delta function
ζ_0	see Eq. (17)
θ	blade angle
θ'	angular coordinate of point on helical vortex
κ	number of blade, $\kappa = 0, ..., B-1$
$d\vec{\lambda}_{ijk}$	elemental vortex
ν	angle between $\hat{r}_i$ and axis of rotation
π	pi
ρ	instantaneous fluid density at a point
$\tilde{\rho}$	fluctuating component of density, $\rho - \rho_0$
ρ_0	freestream fluid density
σ	propeller blade solidity, $Bc/\pi rD$
$\dot{\sigma}$	describes deformation of control surface with respect to time
τ	source time, $t - r/c$
ϕ	flow angle with plane of rotation

Φ	velocity potential (acoustic pressure)
$\dot{\Phi}$	time derivative of Φ
ϕ_0	advance angle; see Fig. (1)
ϕ_κ	angle between blade κ and reference blade
Φ_n	derivative of local pressure with respect to outer surface
ϕ_{q0}	resolving scalar (see Eq. (13))
$\varphi(k)$	Sears function relationship normal
ψ	angle of blade with respect to x-axis
Ψ	angle between blade passages
$\Delta\psi$	incremental blade rotation angle
ψ_j	angular coordinate of field point
ψ_i^N	angular coordinate of blade
ω	circular frequency, $2\pi/T$
Ω	rotation speed of propeller (rad/sec)

Subscripts

F	front propeller blade
B	aft propeller blade
rms	root-mean-square
ref	reference value

TABLE OF CONTENTS

LIST OF FIGURES

Figure Page

Figure Page

Figure Page

Figure Page

Figure Page

Figure Page

CHAPTER I

INTRODUCTION

Turbomachines, which consist of lifting surfaces rotating about an axis, are designed to transfer energy between themselves and a surrounding fluid medium. Kinetic energy is either extracted from the fluid and used to drive a shaft, as with a windmill, or imparted to the surrounding fluid, as with fans, propellers, and rotors. In the latter, this energy transfer creates an equal and opposite force on the lifting surfaces which can be used to provide thrust for an airplane or lift for a helicopter. As a result of the dynamic interaction between a propeller or rotor and the surrounding fluid, a certain amount of energy is lost. This energy is in the form of turbulence and fluid rotation behind the propeller, and translates directly to a reduction in the propulsive efficiency. Another result of rotor–fluid interaction is that small pressure fluctuations are imparted to the fluid which radiate in all directions. These fluctuations are discernible as noise and are a major consideration in the operation of propellers and rotors.

Aircraft propeller noise can have significant physiological and economic consequences. Operation of many propeller-driven aircraft from airports located near residential areas is restricted to daylight or evening hours by local and/or Federal Aviation Authority (FAA) regulations.[1] Additionally, the prospect of travel in acoustically unsatisfactory aircraft can encourage prospective passengers to seek other modes of

---

Journal model is *AIAA Journal of Aircraft*.

transportation. Currently, aircraft designers attempt to reduce the cabin noise which reaches passengers by inserting special acoustic materials in the skin of the aircraft. These serve to absorb and deaden the noise which reaches the interior of the fuselage, but at the cost of increased aircraft weight and reduced payload.

Despite their disadvantages, high speed propellers and especially counterrotating propellers hold distinct promise in the area of fuel efficiency. Although fuel costs are currently a smaller percentage of direct operating costs than in previous years, it is not expected that this trend will continue. Consequently, improvements in the operating efficiency of propulsive devices will be required in the near future. Recent studies have indicated that counterrotating propeller configurations, which consist of two propellers in tandem rotating in opposite directions, offer higher propulsive efficiency in the high subsonic and transonic cruise flight regimes than single-disk propellers, turbofans, or turbojet engines. In addition, counterrotating propeller configurations have significantly higher efficiencies when operated in off-design or non-cruise conditions.

Despite the promises of improved efficiency and reduced operating costs, counterrotating propellers present more problems in the area of noise than single disk propellers. Under certain flight conditions, both single-disk and counterrotating propeller geometries can experience fluctuating loads which result in a highly directional unsteady acoustic component that may be in excess of the steady acoustic component. These unsteady forces arise from numerous sources, e.g., the aircraft flying at an angle of attack relative to the propeller axis of rotation, or operation of the propeller

in a nonuniform wake due to a nacelle or some other obstruction. In addition, counterrotating propellers always experience unsteady loads due primarily to interaction between the front and aft propeller blades. As the blades of the counterrotating configuration rotate in close proximity with each other, aerodynamic interference alters the magnitude and velocity of the airflow over their surfaces, resulting in a periodic variation of the thrust and torque-force. These fluctuating forces create a highly directional noise component that dominates the noise pattern in front of and behind the counterrotating configuration.

In an effort to examine more closely the acoustics of a counterrotating propeller, the object of this thesis is to develop an approximate method by which to model the acoustic characteristics associated with these configurations. The advantage of this approach will be in quickly and easily predicting the acoustics associated with a counterrotating configuration without requiring the extensive computer time and cost associated with more complicated analytical methods.

CHAPTER II

PROPELLER ACOUSTIC PREDICTION METHODS

Since the early 1900's, researchers have attempted to theoretically predict the acoustics associated with rotating propellers. In 1936, Gutin[2] published an acoustic model for a stationary propeller that was later expanded by Garrick and Watkins[3] to include the effects of forward flight. In either method, the thrust and torque distribution along the radius of the propeller blades must be known *a priori* from experimental measurements or theoretical predictions. Then, the acoustic pressures P_n at the harmonics of the fundamental frequency are obtained by integrating the thrust and torque distribution along the radius of the propeller blade and multiplying by appropriate flow parameters. The Gutin formulation is shown as an example:

$$P_n = \frac{nB\Omega}{2\pi a_0 R}\int_0^{R_{\text{tip}}}\left(-\frac{dT}{dr}\cos\nu + \frac{a_0}{\Omega r^2}\frac{dQ}{dr}\right)J_{nB}\left(\frac{\Omega r}{a_0}\sin\nu\right)dr. \tag{1}$$

Note that no information is obtainable concerning the phase relationship between the harmonics, and thus the pressure time-history cannot be calculated. This approach, as are others which yield only the acoustic frequency spectra of a propeller, is therefore referred to as a frequency-domain solution.

In 1952, the Lighthill Acoustic Analogy was published as a means of predicting the sound pressure field generated by a fluid in motion. This analogy incorporates three mechanisms by which sound is produced: fluctuations in mass, fluctuations in momentum or rate of mass flux, and variations in the rate of momentum flux. These acoustic sources are, respectively, referred to as: monopoles, from which pressure

fluctuations radiate uniformly in all directions; dipoles, which act as two monopole sources 180° out of phase and which radiate sound directionally; and quadrupoles, which radiate sound as two dipoles of equal and opposite strengths and are highly directional. Lighthill's formulation is written as:

$$4\pi a_0^2(\rho-\rho_0)(\tilde{x},t) = \frac{\partial}{\partial t}\int\left[\frac{\rho_0 V_n}{r|1-M_r|}\right]dS - \frac{\partial}{\partial x_i}\int\left[\frac{l_i}{r|1-M_r|}\right]dS + \frac{\partial^2}{\partial x_i \partial x_j}\int\left[\frac{T_{ij}}{r|1-M_r|}\right]dV. \tag{2}$$

An extension of the Lighthill Analogy was developed by Ffowcs Williams and Hawkings[4] for an arbitrary solid boundary moving through space and is presented in the next Chapter. A major contribution was its formulation in terms of general functions, which allow evaluation of highly singular integrals that would otherwise be impossible to solve using conventional functions. In addition, they permit extension of frequency-domain solutions to time-domain solutions. A discussion of generalized functions was presented by Lighthill.[5]

Nearly all modern approaches to propeller acoustic prediction stem from the method of Ffowcs Williams and Hawkings. These include the methods of Farassat,[6] Hawkings and Lowson,[7] Hanson,[8] Woan and Gregorek,[9] and Jou,[10] each whom assumed non-compact acoustic sources, and the method of Succi,[11] who assumed compact sources. This latter assumption, i.e., compact sources, tends to simplify the mathematics for subsonic flight regimes. A common feature among all of these methods is that the motion of the propeller blades and their associated loads must be specified in advance. The acoustic pressure at a particular observer location is then obtained using the collapsing sphere method which is discussed in the next Chapter.

For a complete summary of each of the preceding acoustic methods, the reader is referred to White.[12]

Another approach to predicting the acoustics of a propeller is through use of a numerical flow field solution generated by modern computational methods. With the advent of high speed computers, the full three-dimensional flow field around a complicated body may be calculated with varying degrees of accuracy. These flow field solutions are typically generated by solving a governing set of equations, such as those of Euler or Navier-Stokes, within a computational grid. The flow past a propeller with an axi-symmetric nacelle can be calculated by numerically solving the governing equations between two adjacent blades. The azimuthal variation of the pressure along an arc at a specified axial and radial position within the computational grid is then converted to the acoustic pressure in the time-domain for a stationary observer. The pressure time-history can be numerically analyzed to obtain the overall noise level and the associated frequency spectrum. This method was outlined by Korkan, et.al.,[13] and application to various numerical flow field solvers has been performed by several researchers, including White, Denner,[14] Forsyth,[15] Jaeger,[16] and Korkan, et.al.[17]

An advantage of this approach is that once a flow field solution is obtained, an acoustic solution can quickly and easily be obtained for many observer locations within the computational boundary, referred to as the "near field." In addition, these numerical methods are capable of calculating the flow fields of transonic and supersonic propeller configurations, thereby allowing noise calculations for flow fields containing shock waves. The chief disadvantage of these methods is the high cost associated with obtaining an accurate numerical flow field solution, since they currently

require costly amounts of computer time on large mainframe computers. Also, the accuracy of these flow field solvers tends to diminish in regions near the computational boundary because of grid resolution. Finally, direct calculation of acoustic conditions using this method is limited to observer locations within the computational domain.

For calculation of far field acoustic conditions, a method was suggested by Farassat and Myers.[18] Using generalized functions, a version of the Hawkings method[19] applicable to propellers operating at transonic Mach numbers was developed. The method of Farassat and Myers assumes a non-rotating control cylinder which has surface pressure fluctuations generated by the interior propeller configuration. Numerically, the surface pressure fluctuations are taken from the flow field solution at a specified radius from the axis of rotation. The acoustic pressure at a specified observer in the far field is given by:

$$\Phi(\tilde{x},\tau) = \frac{1}{4\pi}\iint_{S_c}\left[\frac{E_1}{r(1-M_R)}\right]_{\text{ret}} dS_c + \frac{1}{4\pi}\iint_{S_c}\left[\frac{\Phi E_2}{r^2(1-M_R)}\right]_{\text{ret}} dS_c, \tag{3}$$

where:

$$\begin{aligned} E_1 = {} & (M_n^2-1)\Phi_n + M_n\tilde{M}_t\cdot\nabla_2\Phi - \frac{M_n\dot{\Phi}}{a_o} + \\ & \frac{1}{a_o(1-M_R)\left[(\dot{n}_r - \dot{M}_n - \dot{n}_M)\Phi + (\cos\theta - M_n)\dot{\Phi} + (\cos\theta - M_n)\Phi\dot{\sigma}\right]} + \\ & \frac{1}{a_o(1-M_R)^2}\left[\dot{M}_R(\cos\theta - M_n)\Phi\right], \end{aligned} \tag{4}$$

and:

$$\begin{aligned} E_2 = {} & \cos\theta + \frac{1}{1-M_R}\left[2M_R\cos\theta - M_nM_R - M_n\right] \\ & + \frac{1}{(1-M_R)^2}\left[(\cos\theta - M_n)(M_R^2 - M^2)\right]. \end{aligned} \tag{5}$$

Several complications arise when using a numeric flow field solver to calculate the acoustics of a counterrotating propeller. In the flow field solution methods, the

presence of a second propeller transforms the problem from a steady to an unsteady solution, thereby significantly increasing the difficulty of accurately calculating the flow field. Attempts have been made at obtaining time-invariant solutions by averaging the flow conditions on a plane between the front and aft propeller and have yielded good comparison with Overall Sound Pressure Levels (OASPL) and frequency spectra, as presented by Kim.[20] However, deficiencies have been noted in the prediction of acoustic pressure-time histories.

A numerical method which solves the Euler equations to compute the unsteady, three-dimensional, transonic flow field about a single or counterrotating propfan was presented by Whitfield.[21] This method has demonstrated good overall agreement between theoretical predictions and experimental propfan performance measurements, and consequently could prove viable to predict the unsteady near field acoustics of a counterrotating propeller. However, the associated computer costs are even greater than those for steady flow field solvers, inhibiting its use for routine acoustic predictions.

In the development of the approximate counterrotating propeller acoustic model used in this thesis, preference was given to speed and ease of calculation. Consequently, use of a numerical flow field solution method was eliminated due to their large requirements of computer time and the associated cost. It was therefore decided to employ one of the methods based on the Ffowcs Williams-Hawkings equation discussed at the beginning of this Chapter to predict the counterrotating configuration acoustics.

Of the several methods presented, the compact acoustic source method of Succi was selected as the basis of the acoustic calculation. This methodology was created to predict the acoustics of a lightly loaded subsonic propeller, and requires that the forces on the blades be known in advance. Extension to the counterrotating configuration involves calculating the performance and acoustics of each propeller separately and summing to obtain their combined effect.

Several approaches, including the method of Davidson,[22] have been developed to obtain the performance of a counterrotating propeller configuration by calculating average interference effects between the propellers. A preliminary study using the methods of Davidson and Succi to investigate the steady noise in the disk plane of a counterrotating propeller configuration with different front/aft rotation speeds was presented by Denner and Korkan.[23] From an acoustic perspective however, since the unsteady forces on the blades are not modeled, this approach by itself does not provide enough information to predict the complete noise characteristics around the entire propeller.

At least two related approaches have been developed to calculate the unsteady loads of a counterrotating propeller configuration. These are the Local Circulation Method of Watanabe,[24] and the vortex lattice formulation of Lesieutre,[25] which calculate the inviscid, incompressible, unsteady aerodynamics of a counterrotating propeller.

To provide the unsteady forces of a subsonic counterrotating configuration for use in the Succi acoustic methodology, it was decided to combine the methods of Davidson and Lesieutre. That is, the Davidson method is used to calculate the mean

subsonic performance of the configuration and the method of Lesieutre is used to calculate the variation of the blade forces about their mean levels.

Combination of these three methods should allow simple approximation of the acoustics of a counterrotating configuration. The next Chapter will discuss the implementation of the methods of Davidson, Lesieutre, and Succi as they pertain to the acoustic model. Then, theoretical predictions from this model will be compared with experimental counterrotating propeller acoustic measurements. Finally, the noise characteristics of a hypothetical commuter-class counterrotating propeller configuration will be examined in detail, pertaining to the directivity of the harmonics in the near field around the propeller.

CHAPTER III

APPROXIMATE ACOUSTIC MODEL

The method developed in this thesis to predict the acoustics of a counterrotating propeller configuration is an extension of the compact acoustic source method of Succi. The Succi approach simplifies the calculation of propeller acoustics by dividing the blades into many small segments, called compact acoustic sources. The acoustic pressure time-history generated by each source is calculated, and these are then summed to obtain the acoustic signature of the entire propeller. This method requires specification of the propeller geometry, rotation speed, and surface pressure forces on the blades as functions of time. The pressure forces, or loads, on the blades are obtained by first calculating the mean load distribution along the propeller radius with the Davidson performance prediction method for counterrotating propellers. Then, the unsteady variation of the loads about their mean values is obtained through use of a modified version of the unsteady propeller performance approach of Lesieutre.

III.1 Acoustic Prediction Method

The acoustic method of Succi for compact sources was developed to simplify prediction of the acoustic signature of a rotating propeller. It is an adaptation of the Ffowcs-Williams Hawkings equation, written as:

$$\frac{\partial^2}{\partial \tau^2}\tilde{\rho}H(f) - a_0^2\frac{\partial^2}{\partial y_i^2}\tilde{\rho}H(f) = \frac{\partial}{\partial \tau}\Big[\rho_0 v_i n_i |\nabla f|\delta(f)\Big] - \frac{\partial}{\partial y_i}\Big[p_{ij}n_j|\nabla f|\delta(f)\Big] + \frac{\partial^2}{\partial x_i \partial x_j}\Big[(p_{ij} + \rho_0 u_i u_j - a_0^2\tilde{\rho}\delta_{ij})H(f)\Big]. \tag{6}$$

Developed from the Lighthill analogy for the sound pressure field of a moving fluid, this Equation gives the acoustic pressure generated by a body moving through a fluid. Due to its nonlinear nature, exact solutions of Eq. (6) are essentially impossible to obtain.

Succi undertook to make the solution of the Ffowcs Williams-Hawkings equation more tractable; i.e., through application of Green's function, Eq. (6) can be written for subsonic conditions as:

$$4\pi p(\tilde{x},t) = -\frac{\partial}{\partial x_i}\int_S \left\{\frac{p_{ij}n_j}{r|1-M_r|}\right\}_{\text{ret}} dS + \frac{\partial}{\partial t}\int_S \left\{\frac{\rho_0 v_i n_i}{r|1-M_r|}\right\}_{\text{ret}} dS. \qquad (7)$$

Here, $p(\tilde{x},t)$ is the acoustic pressure experienced by the observer and "ret" indicates that the integrands are to be evaluated at the retarded time, $\tau = t - r/a_0$.

To understand the retarded time concept, consider a stationary acoustic source and stationary observer at two points in a fluid separated by a distance r. At a time τ, the source imparts a pressure fluctuation to the fluid which radiates in all directions at the acoustic velocity a_0 and ultimately reaches the observer at time t. Equating the time interval $(t-\tau)$ to (r/a_0) gives the definition of the retarded time.

If either the source and/or the observer are in motion or the pressure fluctuations of the source vary with time, the retarded time definition remains unchanged. Now, however, r is the distance between the point where the pressure fluctuation is created by the source at time τ and the point where it is "heard" by the observer at time t. That is, r is the straight-line distance traveled by the pressure fluctuation from the source to the observer. This distance is affected neither by motion of the source after the sound is created nor by movement of the observer before the sound is observed.

When several acoustic sources are present, the retarded time of each source will in general be different. The cumulative effect of these sources on the total acoustic pressure experienced by an observer may be understood by imagining a sphere of infinite radius centered on the observer. At a time infinitely far in the past, the sphere begins to collapse towards the observer at the speed of sound. As the surface of the sphere passes through each of the acoustic sources, pressure fluctuations are accumulated at the corresponding retarded times, τ_i, and are carried toward the observer. At time t, the radius of the sphere is zero and the sum of the pressure fluctuations accumulated by the sphere is the acoustic pressure experienced by the observer. During a time interval Δt, an infinite number of spheres will have collapsed onto the observer and the resulting variation in the acoustic pressure is what is interpreted as sound.

Although in a more manageable form, Eq. (7) is still quite difficult to solve numerically. For a large complicated body moving through a fluid, such as a propeller, the shape of the body as well as the pressure distribution over its surface is normally very difficult to express mathematically. To simplify the mathematics, Succi rewrote Eq. (7) for acoustically compact sources. By definition, the greatest physical dimension of a compact source must be much smaller than its closest distance to the observer, giving an appearance of a point source. This allows the motion of every point in the body to be approximated by the motion of its center, eliminates rotation effects, and allows the pressure on the surface of the source to be considered constant. The cumulative result is considerable simplification of the mathematics.

Rewritten for N compact sources, Eq. (7) has the form:

$$4\pi p(t) = 4\pi \sum_{n=1}^{N} \Big\{ p_{L_n}(\tau) + p_{T_n}(\tau) \Big\}_{\text{ret}}, \tag{8}$$

where the loading noise, p_L, observed at time t emanating from blade element n is given by:

$$\begin{aligned} 4\pi p_{L_n}(\vec{x},t) = \Bigg\{ & \frac{1}{(1-M_r)^2 r} \Big[\frac{\hat{r}_i}{a_0} \cdot \frac{\partial \vec{F}_i}{\partial \tau} + \frac{(\hat{r}_i \cdot \vec{F}_i)}{(1-M_r)} \Big(\frac{\hat{r}_i}{a_0} \cdot \frac{\partial \vec{M}_i}{\partial \tau} \Big) \Big] \\ & + \frac{1}{(1-M_r)^2 r^2} \Big[(\hat{r}_i \cdot \vec{F}_i) \frac{(1 - \vec{M}_i \cdot \vec{M}_i)}{(1-M_r)} - \vec{F}_i \cdot \vec{M}_i \Big] \Bigg\}_{\text{ret}}, \end{aligned} \tag{9}$$

and the thickness noise, p_T, is given by:

$$4\pi p_{T_n}(\vec{x},t) = \rho_0 \Bigg\{ \frac{1}{r} \frac{1}{(1-M_r)} \frac{\partial}{\partial \tau} \frac{1}{(1-M_r)} \frac{\partial}{\partial \tau} \frac{\mathcal{V}(\tau)}{|1-M_r|} \Bigg\}_{\text{ret}}. \tag{10}$$

From Eqs. (9) and (10), the acoustic pressure at time t from one compact acoustic source is seen to depend on its motion, M_r and $\vec{M}_i$, its distance from the observer, r, the pressure forces on its surface, $\vec{F}_i$, and its volume, $\mathcal{V}(\tau)$, all at the retarded time τ. The geometry associated with this rotating compact source is shown in Fig. 1.

To calculate the acoustics of a counterrotating propeller configuration, the blades are divided into many compact acoustic sources. The terms in Eqs. (9) and (10) must be known for each of these N compact sources. The geometric and velocity terms, including r, $\hat{r}_i$, M_r, and $\vec{M}_i$, describe the motion and position of the sources and are defined by the motion of the propeller. Therefore, to calculate the noise of a counterrotating propeller configuration it remains only to determine the loads on the front and aft propellers as functions of time. This is accomplished by first calculating the mean or average loads along the span of the propeller blades and then

the fluctuations of these loads about their mean values as functions of radial position and time.

III.2 Performance Analysis

The performance of a counterrotating propeller configuration is calculated using the analysis method of Davidson as modified by Korkan and Playle[26] and Playle, et.al.[27] This strip-analysis method generates the time-averaged radial distributions of velocity, angle of attack, and differential thrust, torque, and horsepower absorbed. It assumes that the induced velocities are small, and neglects their products and squares in formulation of the associated equations resulting in a first-order theory. This assumption, however, is not felt to be limiting in the calculation of the performance of a counterrotating configuration.

The fundamental idea behind a strip analysis method is to calculate the performance of a three-dimensional propeller by modeling the blades as two-dimensional airfoil sections placed about a pitch-change axis. By accounting for three-dimensional effects in the calculation of the radial velocity and angle of attack distributions, two-dimensional lift and drag data can be used to obtain the radial variations of thrust and torque which are integrated to obtain the total thrust and torque of the propeller.

To calculate the steady performance of a counterrotating propeller configuration with the method of Davidson, the radial velocity distribution must first be obtained. The components of this velocity, shown in Fig. 2, include the axial or flight velocity, V_∞, which is constant along the radius; the azimuthal velocity, Ωr, caused by rotation of the propeller; and the induced velocities u, v, and w_1, which result from interaction

between the propellers. Success of the method depends on accurate calculation of these latter terms.

III.2.1 Fixed-Pitch Performance Calculation

The Davidson method for calculation of the performance of a fixed-pitch counterrotating propeller configuration is iterative in nature. To summarize, at a particular radial station on both the front and aft propellers, initial values of the resultant velocity, W, and angle of attack, α, are assumed. A series of calculations is then performed which results in new values for the velocity and angle of attack. These new values, which are usually different for the front and aft propellers, will likely differ from those assumed at the beginning of the iteration. If this is the case, another iteration is made using the newly generated values of W and α. This process is repeated until at the end of an iteration, the old and new velocities and angles are within a prescribed tolerance of each other, thereby indicating a converged solution. A new radial station is then selected and the iterative procedure repeated until the performance along the entire radius of the blade is calculated.

To obtain the performance of the front and aft propellers, the Davidson method requires that the radial distribution of the blade chord, c, the thickness ratio, $(t/c)_{\max}$, the design lift coefficient, C_{L_D}, and the blade twist angle, θ, be specified for both propellers. This geometry will remain unaltered during the iteration. At a selected radial station, initial estimates of the resultant velocities W_F and W_B and angles of attack α_F and α_B, shown in Fig. 2, are made. From these parameters, the two-dimensional lift and drag coefficients, C_L and C_D, of either blade segment are obtained via an airfoil data bank which contains lift and drag coefficients at discrete angles

of attack and Mach numbers from which the lift and drag at any α and M may be interpolated.

Next, the Lock[28] tip loss factor, X_0, for either propeller is calculated from the expression:

$$X_0 = \frac{q's'}{(k'/\bar{w})p' - q's'r'}, \tag{11}$$

where:

$$\begin{aligned} p' &= \frac{1}{2}\phi_{q_0}\cos\phi_0, \\ q' &= \frac{1}{2\sin\phi_0}, \\ r' &= \cos^2\phi_0 - \sin^2\phi_0, \\ s' &= \frac{J}{\pi r_c}K(r_c)\sin\phi_0, \\ (k'/\bar{w}) &= 2. \end{aligned} \tag{12}$$

Here, $K(r_c)$ is the Theodorsen circulation function[29] for dual-rotation propellers, and:

$$\phi_{q_0} = \sin\phi_0 + \frac{1}{C_L/C_D}\cos\phi_0. \tag{13}$$

X_0 varies from 1.0 on the axis of rotation to 0.0 at the tip, as shown in Fig. 3.

The advance angle, ϕ_0, for either propeller is defined by:

$$V_\infty = r\,\Omega\,\tan\phi_0, \tag{14}$$

and is the angle the flow would make with the plane of rotation of the propeller apart from three-dimensional effects. The interference angles, β, which result from the interaction between the propellers are calculated by:

$$\begin{aligned} \beta_F &= b\sigma(C_{L_F} + \zeta_{0_F}C_{L_B}), \\ \beta_B &= b\sigma(C_{L_B} + \zeta_{0_B}C_{L_F}), \end{aligned} \tag{15}$$

where:

$$b = \frac{1}{4X_0 \sin \phi_0}, \tag{16}$$

and:

$$\begin{aligned} \zeta_{0_F} &= X_0 \cos^2 \phi_0, \\ \zeta_{0_B} &= X_0(\cos^2 \phi_0 - 2 \sin^2 \phi_0). \end{aligned} \tag{17}$$

The interference angles are added to the advance angles, ϕ_0, to obtain the angles ϕ which the resultant velocities make with the plane of rotation:

$$\phi = \phi_0 + \beta. \tag{18}$$

The difference between ϕ and the blade twist angle of the airfoil section, θ, gives the updated angle of attack of the blade segment:

$$\alpha = \theta - \phi. \tag{19}$$

Next, a new resultant velocity W is obtained by calculating the interference velocities u, v and w_1 for either propeller. These are obtained by solving the following simultaneous equations for w_{1_F} and w_{1_B}:

$$\begin{aligned} w_{1_F} &= r_F \Omega_F \sec \phi_{0_F} \sin \beta_F - u_F \cos \phi_F - v_F \sin \phi_F, \\ w_{1_B} &= r_B \Omega_B \sec \phi_{0_B} \sin \beta_B - u_B \cos \phi_B - v_B \sin \phi_B, \end{aligned} \tag{20}$$

where:

$$\begin{aligned} u_F &= X_{0_B} w_{1_B} \cos \phi_B, \\ u_B &= X_{0_F} w_{1_F} \cos \phi_F, \\ v_F &= 0, \\ v_B &= -2X_0 w_{1_F} \sin \phi_F. \end{aligned} \tag{21}$$

The resultant velocities are then obtained from:

$$W_F = r_F \Omega_F \sec \phi_{0_F} \cos \beta_F + u_F \sin \phi_F - v_F \cos \phi_F,$$
$$W_B = r_B \Omega_B \sec \phi_{0_B} \cos \beta_B + u_B \sin \phi_B - v_B \cos \phi_B. \tag{22}$$

As previously discussed, the newly-generated values of α and W are compared with those of the preceding iteration, and if either is different another iteration must be made.

Once a converged solution for the blade segment performance is obtained at the specified number of stations along the radius of each propeller, the overall performance of the configuration is obtained by calculating at each radial station the differential thrust, defined as:

$$dT/dr = \pi \rho_0 r \sigma W^2 (C_L \cos \phi - C_D \sin \phi), \tag{23}$$

and differential torque, given by:

$$dQ/dr = \pi \rho_0 r^2 \sigma W^2 (C_L \sin \phi + C_D \cos \phi). \tag{24}$$

The total thrust and torque of each propeller are obtained by numerically integrating dT/dr and dQ/dr along the radius.

III.2.2 Constant-Speed Propeller Analysis

More sophisticated and more commonly used than fixed-pitch propellers are constant-speed propellers. Rather than requiring a change of RPM to alter the speed of the aircraft, the thrust of these propellers is varied by rotating their blades in the hub, allowing the engine to maintain a constant rotation speed and operate in a more fuel-efficient manner.

To calculate the performance of a counterrotating configuration with constant-speed propellers, a different iterative procedure is employed. The geometry of the configuration must first be specified as in the previous Section. In addition, the horsepower provided by the engine to the propeller must be specified. Before the first iteration, estimates of the front and aft blade-set angles are made. The blade-set angle of a propeller is the amount by which the blades are rotated in the hub and is added to the blade twist angle, θ, along the entire radius of the blade. Using this modified twist distribution, the performance of the configuration is analyzed exactly as described for a fixed-pitch configuration. When completed, the differential power absorbed at each radial station of the propeller is calculated by:

$$dP/dr = \frac{1}{2}\pi\rho_0 r\sigma D\frac{(C_L \sin\phi + C_D \cos\phi)}{\cos^2\phi}. \tag{25}$$

This power distribution is then integrated to obtain the total horsepower absorbed by the propeller.

With constant-speed propellers, the horsepower provided by the engine must be completely absorbed by the propeller. If the horsepower provided is different from the horsepower absorbed, the blade-set angles of the propeller is adjusted and the analysis procedure repeated. After each iteration, the total horsepower absorbed is compared with the horsepower of the engine, and if necessary the procedure is repeated until the horsepower provided by the engine and the horsepower absorbed by the propeller agree within a prescribed tolerance.

III.2.3 Performance Design

A design method, whereby an optimum propeller for a given set of input conditions may be designed, is also described by Davidson. This approach makes use of the Betz condition for dual rotation, defined as:

$$k' = \frac{\frac{d}{d(\sigma C_L)}\left(\frac{dP_F}{dr} + \frac{dP_B}{dr}\right)}{\Omega \frac{d}{d(\sigma C_L)}\left(\frac{dQ}{dr}\right)}. \tag{26}$$

This relationship is derived by requiring the total power loss of the propeller be minimal while still absorbing the horsepower provided by the engine. Equation (26) must be satisfied along the entire radius of the propeller blade, and indeed k' is a constant which is everywhere the same for a given propeller. However, k' will in general be different for the front and aft propellers, and must be determined iteratively by requiring that the power absorbed by the propeller match the power output by the engine.

Through analysis of Eq. (26), Davidson arrived at the following expression for the blade section solidity-lift coefficient of an optimum propeller using calculus of variations:

$$\sigma C_L = \frac{\frac{1}{2}k'\phi_{q_0}\cos\phi_0 - \frac{C_D}{C_L}}{\frac{1}{2\sin\phi_0}\left(\frac{1}{X_0} + \cos^2\phi_0 - \sin^2\phi_0\right)}. \tag{27}$$

To design a propeller using Eq. (27), the radial distribution of blade thickness and design lift coefficient must be specified along with such flight parameters as propeller rotation speed, velocity, engine horsepower, and atmospheric conditions. Then, initial estimations of the radial distribution of chord and blade twist angle are made; these values need only be approximate as they will change during the design process. Initial

values of k' for the propellers are then selected. This assumed propeller geometry is analyzed as described for the fixed-pitch propeller, with the added stipulation that the angles of attack at each radial station be selected so as to correspond to the maximum local L/D ratio.

After completion of one design iteration, a new solidity-lift coefficient distribution is obtained with Eq. (27) from which a new chord distribution is calculated. The power absorbed by the propeller is calculated from Eq. (25) and compared with the horsepower provided by the engine. If the engine horsepower and that absorbed by the propeller are different, a new value of k' for each propeller is selected and the design procedure repeated using the chord and blade twist distributions resulting from the most recent iteration until sufficient agreement between horsepower provided and absorbed is attained.

III.3 Unsteady Propeller Loads

As discussed at the beginning of this Chapter, the Succi compact source model for propeller acoustic prediction requires that the radial thrust and torque-force distribution on the propeller blades be known as functions of time. However, the blade loads that are calculated with the Davidson performance model as described in the previous Section are averaged over one rotation. No information can directly be obtained from this method concerning the time-dependent variation. To completely describe the blade loads, some other method must be used to approximate the unsteady loading on the blades of the counterrotating propeller. The unsteady loads are added to the steady loads to reflect the time-variation of the forces on the blades of the propeller.

If the time-dependent variation of the induced velocity components u, v, and w_1 of Eqs. (20) and (21) is known, the variation of the unsteady loads can be obtained. This is accomplished by solving Eq. (20) for ϕ and subtracting from the blade twist angle (Eq. (19)) to obtain the angle of attack of the blade segment. The instantaneous lift and drag are then obtained from an airfoil data bank. This method is detailed in a following Section.

To calculate the unsteady forces on the blades for use with the Succi compact acoustic source model, a method based on the vortex lattice formulations of Sullivan[30] and Lesieutre is employed. The variation of the induced velocities on the blades of the counterrotating propeller configuration will be calculated and then converted to the unsteady forces as described in the next Section.

III.3.1 Induced Velocity Calculation

It can be demonstrated from momentum considerations that a vortex of strength Γ in a uniform flow of velocity V_∞ and density ρ_0 experiences a force of magnitude $\rho_0 V_\infty \Gamma$ in a direction perpendicular to V_∞, as shown in Fig. 4. The Kutta-Joukowski theorem states that a cylinder of any cross section in the same flow conditions also experiences a normal force of $\rho V_\infty \Gamma$, where Γ is the circulation about the cylinder. Consequently, the effect of the lift force generated by an airfoil with circulation Γ on the flow field can be represented by replacing the airfoil with a vortex of the same circulation strength.

This analogy between an airfoil and a vortex can be used to analyze the flow field about a three-dimensional wing, i.e., one with finite span. Consider first a finite wing with constant lift across the span. The wing can be replaced by a vortex bound

to the quarter-chord line of the wing as shown in Fig. 5. The circulation strength of the vortex is obtained from the lift force on the wing as discussed in the preceding paragraph. At each wing tip, the vortex turns parallel to the flow. Downstream, at a distance $V_\infty t$ behind the airfoil where t is the time that the wing has been in flight, the ends of the vortex turn inward and rejoin to form a closed rectangular path, thereby satisfying the Helmholtz Vortex Laws. In steady flow conditions, the flight time t is assumed infinite and the downstream "starting vortex" is ignored. The remaining U-shaped vortex is called a horseshoe vortex and can be used to obtain the induced velocity at any point in the flow field around the wing.

On a real wing, however, the lift force and circulation strength vary across the span. This wing and its wake can be modeled similarly by dividing it into several segments along its span. Each segment is treated as a finite wing with constant lift and replaced by a horseshoe vortex whose circulation strength is taken from the local value of the lift force (Fig. 6). As before, the induced velocity at a point in the fluid around the wing can be obtained by summing the induced velocity of each horseshoe vortex.

This approach was developed by Sullivan to model the flow field about a rotating propeller. As with a finite wing, the blades of the propeller are divided into several radial segments which are replaced by a horseshoe vortex of circulation strength Γ_i. The vortex is bound to the blade quarter-chord and follows the helical paths traced out by the end points of the blade segment to infinity, as shown in Fig. 7. The components of the velocity induced by the horseshoe vortex at a point in the surrounding fluid,

referred to as the field point, can then be obtained by summing the velocities induced by each of the straight and helical vortex elements.

The Biot-Savart Law gives the relationship for the velocity induced at a point in space by a vortex segment of length l and circulation strength Γ. It has the general form:

$$\vec{v}_{ijk} = \frac{\Gamma}{4\pi} \int_0^l \frac{\vec{R}_{ijk} \times d\vec{\lambda}_{ijk}}{|\vec{R}_{ijk}|^3}. \tag{28}$$

To employ the Biot-Savart Law in the calculation of the velocities induced by a propeller, the terms in Eq. (28) must be defined with respect to a helical horseshoe vortex. A right-hand helical vortex is specified parametrically as:

$$\begin{aligned} x(\theta') &= r_i \cos(\theta' + \phi_\kappa), \\ y(\theta') &= r_i \sin(\theta' + \phi_\kappa), \\ z(\theta') &= Z_i + \frac{V_\infty}{\Omega}(\theta' - \psi_i^N), \end{aligned} \tag{29}$$

with the geometry shown in Fig. 7. The coordinates of the field point at which the induced velocity is to be calculated are:

$$\begin{aligned} x' &= r_j \cos\psi_j, \\ y' &= r_j \sin\psi_j, \\ z' &= z_j. \end{aligned} \tag{30}$$

The vector from a point on the helical vortex to the field point is given by:

$$\vec{R}_{ijk}(\theta') = (x - x')\hat{\imath} + (y - y')\hat{\jmath} + (z - z')\hat{k}, \tag{31}$$

and an elemental piece of the vortex is specified as:

$$d\vec{\lambda}_{ik} = \begin{pmatrix} -r_i \sin(\theta' + \phi_\kappa) \\ r_i \cos(\theta' + \phi_\kappa) \\ V_\infty/\Omega \end{pmatrix} d\theta'. \tag{32}$$

From these definitions, the three components of the induced velocity $\vec{v}_{ijk} = u_1\hat{i} + u_2\hat{j} + u_3\hat{k}$, which act in the directions (x, y, z) at the point (x', y', z'), are written as:

$$\left(\frac{u_1}{V_\infty}\right) = \frac{\Gamma_i}{4\pi V_\infty}\int_{\psi_i^N}^{\infty}\frac{V_\infty}{\Omega}\sum_{\kappa=1}^{B}\left\{\frac{r_i\sin(\theta'+\phi_\kappa) - r_j\sin(\psi_j)}{|\vec{R}_{ijk}|^3} - \frac{\left[\frac{\Omega}{V_\infty}(Z_i - z_j) + (\theta' - \psi_i^N)\right]r_i\cos(\theta'+\phi_\kappa)}{|\vec{R}_{ijk}|^3}\right\}d\theta', \tag{33}$$

$$\left(\frac{u_2}{V_\infty}\right) = \frac{\Gamma_i}{4\pi V_\infty}\int_{\psi_i^N}^{\infty}\frac{V_\infty}{\Omega}\sum_{\kappa=1}^{B}\left\{\frac{r_i\cos(\theta'+\phi_\kappa) - r_j\cos(\psi_j)}{|\vec{R}_{ijk}|^3} - \frac{\left[\frac{\Omega}{V_\infty}(Z_i - z_j) + (\theta' - \psi_i^N)\right]r_i\sin(\theta'+\phi_\kappa)}{|\vec{R}_{ijk}|^3}\right\}d\theta', \tag{34}$$

$$\left(\frac{u_3}{V_\infty}\right) = \frac{\Gamma_i}{4\pi V_\infty}\int_{\psi_i^N}^{\infty}\sum_{\kappa=1}^{B}\frac{r_i^2 - r_i r_j\cos(\theta'+\phi_\kappa-\psi_j)}{|\vec{R}_{ijk}|^3}d\theta'. \tag{35}$$

Similarly, Eq. (28) can be defined for the straight-line vortex segment, with the induced velocity components given by:

$$\begin{aligned}
\left(\frac{u_1}{V_\infty}\right)_{ij} &= \frac{-\Gamma_i}{4\pi V_\infty}\Big[(y_L - y')(z_T - z_L) - (z_L - z')(y_T - y_L)\Big]I,\\
\left(\frac{u_2}{V_\infty}\right)_{ij} &= \frac{-\Gamma_i}{4\pi V_\infty}\Big[(z_L - z')(x_T - x_L) - (x_L - x')(z_T - z_L)\Big]I,\\
\left(\frac{u_3}{V_\infty}\right)_{ij} &= \frac{-\Gamma_i}{4\pi V_\infty}\Big[(x_L - x')(y_T - y_L) - (y_L - y')(x_T - x_L)\Big]I,
\end{aligned} \tag{36}$$

where:

$$I = \frac{1}{ac - bb}\left[\frac{a+b}{\sqrt{a+2b+c}} - \frac{b}{\sqrt{c}}\right], \tag{37}$$

and:

$$\begin{aligned}
a &= (x_T - x_L)^2 + (y_T - y_L)^2 + (z_T - z_L)^2,\\
b &= (x_T - x_L)(x_T - x') + (y_T - y_L)(y_T - y') + (z_T - z_L)(z_T - z'),\\
c &= (x_L - x')^2 + (y_L - y')^2 + (z_L - z')^2,
\end{aligned} \tag{38}$$

where (x_L, y_L, z_L) and (x_T, y_T, z_T) are the coordinates of the inner and outer endpoints of the straight-line vortex segment.

To calculate the velocity induced by a propeller, the lift distribution along the radius of the propeller must be known. The blades of the propeller are divided radially into N segments and a horseshoe vortex is bound to the quarter-chord of each segment. The circulation strength of the i^{th} vortex is taken from the conditions at the radial station in the middle of the blade segment, and is calculated by:

$$\Gamma_i = \frac{1}{2} C_L W c, \tag{39}$$

The induced velocity at any field point is obtained by calculating and adding the velocity induced by each of the straight-line vortex segments and the helical vortices.

III.3.2 Calculation of Unsteady Loads

In a counterrotating propeller configuration, the propeller blades operate in a continuously varying velocity field. Superimposed over the axial and tangential velocity components are induced velocities whose magnitudes vary with time due to interference between the front and aft propeller blades. This variation results in a continuously varying angle of attack and velocity experienced by the airfoil segments of the blades. As with a two-dimensional airfoil, this approach results in a time-dependent variation of the loads experienced by the propeller.

The variation of the induced velocities of the counterrotating configuration is calculated using the horseshoe vortices and Biot-Savart Law as formulated in the previous Section. The next two subsections will detail these calculations, followed by the method of converting these induced velocities to the time-dependent loads

required by the Succi compact acoustic source method to calculate the acoustics of a counterrotating propeller.

III.3.2.1 Induced Velocities on a Counterrotating Propeller

To calculate the variation of the induced velocities experienced by the propeller blades, the orientation of the front and aft propellers at time $t = 0$ is selected so that the quarter-chord lines of the front propeller blades are aligned with those of the aft propeller blades. This orientation corresponds to an interface angle of zero degrees. The induced velocity is calculated at several radial stations along the mid-chord of one blade of both the front and aft propellers. The choice of the mid-chord will be discussed in the next subsection. Since the blades are symmetric, this induced velocity distribution will apply equally to all of the blades of that propeller.

Next, the propellers are rotated by some small angle $\Delta\psi$, the front in a clockwise direction and the aft in a counterclockwise direction. The interface angle between the formerly-adjacent blades is now equal to $2\Delta\psi$. At this new blade alignment, the induced velocity is again calculated along the mid-chord line of one blade on both propellers. This procedure is repeated several times, the interface angle being increased incrementally and the induced velocity distribution calculated. After several adjustments of the interface angle, a condition will arise where the front and aft blades are again realigned, at which time the orientation of the blades relative to each other will exactly match that at time $t = 0$. If both propellers rotate at the same speed, the angular distance traveled by each blade is given by:

$$\Psi = \frac{2\pi}{2B}, \tag{40}$$

and the time which elapses, referred to as the blade loading period, is given by:

$$T_L = \frac{1}{2nB}. \tag{41}$$

Note that this time interval is half the blade passing period:

$$T = \frac{1}{nB}. \tag{42}$$

This is because the blade passing period is the interval of time which elapses between repetitions of a given propeller orientation or alignment, and the blade loading period is the interval of time which elapses between repetitions of the velocity field experienced by the propeller. The blade loading period is dependent not upon the rotation speed of a given propeller, n, but rather upon the relative rotation speed between the front and aft propellers, $2n$.

The result of the preceding calculations is that the induced velocity is known along the mid-chord of the blade over one blade loading period T_L. As discussed, these induced velocities could be converted to angles of attack and thus lift coefficients to obtain the time variation of the forces on the blades. However, this does not consider the fact that the induced velocity will vary along the chord of a blade segment. For example, the leading edge might experience an upward velocity component relative to the direction of the resultant velocity, W, while the trailing edge experiences a downward velocity. This is due to the time lag associated with the perturbed flow passing the leading edge and proceeding down the chord of the airfoil. The result of this chordwise velocity variation is a reduction of the lift coefficient that is a function of the frequency of the induced velocity oscillations.

The general problem of an airfoil in a uniform, incompressible flow over which has been superimposed a sinusoidal vertical velocity component was investigated by Sears.[31] The results of this investigation are presented in the next Section, along with their application to the calculation of the unsteady loads on a counterrotating propeller configuration.

III.3.2.2 Unsteady Lift Coefficient of an Airfoil

The Sears function, $\varphi(k)$, is used to calculate the loads experienced by an airfoil in a sinusoidally-varying vertical gust, i.e., a uniform flow over which is superimposed a sinusoidal vertical velocity component (Fig. 8). This function $\varphi(k)$ is the total lift coefficient for a wing immersed in a harmonically oscillating gust normalized to unity by its steady-state value.

As presented by Drischler,[32] consider an airfoil in a uniform flow. Superimposed over this flow is a sinusoidal gust of amplitude W_0 and frequency ω, whose vertical velocity component, W_g, is given by:

$$W_g(t) = W_0 e^{(i\omega t)} \tag{43}$$

W_0 is the amplitude of the gust which is maximum at the mid-chord at time $t = 0$, and ω is the circular frequency of the oscillation. The unsteady lift response of this wing is given by:

$$L_g(t) = qSC_{L_\alpha} \frac{W_0 e^{i\omega t}}{V_\infty} \varphi(k). \tag{44}$$

where the real part of this quantity is associated with the in-phase lift component and the imaginary part with the out-of-phase lift. Dividing through by $q\,S$, taking the

lift curve slope C_{L_α} to be 2π, and accounting for compressibility, the lift coefficient per unit span of the wing becomes:

$$C_{L_g}(t) = \frac{2\pi}{\sqrt{1-M^2}} \frac{W_0}{V_\infty} e^{i\omega t} \varphi(k). \tag{45}$$

The Sears function $\varphi(k)$ is a complex function of the reduced frequency k:

$$k = \frac{\omega c}{2V_\infty}. \tag{46}$$

The magnitude of $\varphi(k)$ is 1 at $k = 0$, which corresponds to uniform flow, and decreases with increasing k, as shown in Fig. 9. The phase angle of $\varphi(k)$ increases with k as shown in Fig. 10.

For incompressible flow conditions, $\varphi(k)$ is defined exactly as:

$$\varphi(k)_{M=0} = \left\{ C(k)_{\text{cir}} \Big[J_0(k) - iJ_1(k) \Big] + iJ_1(k) \right\}. \tag{47}$$

where C(k) is the Theodorsen function, defined by:

$$C(k)_{\text{cir}} = \frac{-J_1(k) + iY_1(k)}{-\Big[J_1(k) + Y_0(k)\Big] + i\Big[Y_1(k) - J_0(k)\Big]}. \tag{48}$$

$J_0(k)$ and $J_1(k)$ are Bessel functions of the first kind of orders 0 and 1, and $Y_0(k)$ and $Y_1(k)$ are Bessel functions of the second kind of orders 0 and 1, respectively.

For subsonic Mach numbers, approximations of $\varphi(k)$ were presented by Mazelsky and Drischler[33] and Mazelsky:[34]

$$\varphi(k)_{M=0.5} \approx ik\left(\frac{1}{ik} - \frac{0.390}{0.0716 + ik} - \frac{0.407}{0.374 + ik} - \frac{0.203}{2.165 + ik} \right) e^{ik}, \tag{49}$$

$$\varphi(k)_{M=0.6} \approx ik\left(\frac{1}{ik} - \frac{0.328}{0.0545 + ik} - \frac{0.430}{0.257 + ik} - \frac{0.242}{1.461 + ik} \right) e^{ik}, \tag{50}$$

$$\varphi(k)_{M=0.7} \approx ik\left(\frac{1}{ik} - \frac{0.402}{0.0542 + ik} - \frac{0.461}{0.313 + ik} - \frac{0.137}{1.474 + ik}\right)e^{ik}. \qquad (51)$$

The value of $\varphi(k)$ for a compressible, subsonic Mach number is obtained by interpolating between these equations and Eq. (47). The magnitude and phase relationship of $\varphi(k)$ for subsonic Mach numbers are also shown in Figs. 9 and 10.

Equation (44) was defined for a thin, uncambered airfoil at zero angle of attack operating in a sinusoidal gust. Application of this equation to a general airfoil at a finite angle of attack will be made by taking the unsteady lift coefficient $C_{L_{g,\text{osc}}}$ as the variation of the lift coefficient around the mean. That is, the total oscillating lift coefficient of the airfoil is equal to the mean lift coefficient plus the unsteady lift coefficient as calculated by Eq. (45).

The lift response of an airfoil in a periodic, but general, gust can be modeled with a Fourier Series, which allows a complicated vertical velocity to be broken down into the sum of many sinusoidal oscillations. The unsteady lift coefficient of each of the components can be calculated as described in the preceding paragraphs and added to obtain the time-dependent variation of the total unsteady lift.

To calculate the unsteady lift of an airfoil in a general gust, the vertical velocity $W_{\text{gust}}(t)$ is represented by:

$$W_{\text{gust}}(t) = \sum_{n=1}^{\infty}\Big\{A_n \cos(n\omega t) + B_n \sin(n\omega t)\Big\}, \qquad (52)$$

where the Fourier coefficients A_n and B_n:

$$\begin{aligned} A_n &= \frac{2}{T}\int_0^T W_g(t)\cos(n\omega t)dt, \\ B_n &= \frac{2}{T}\int_0^T W_g(t)\sin(n\omega t)dt. \end{aligned} \qquad (53)$$

are the amplitudes of the sinusoidal velocity components. The unsteady lift coefficient at an angular frequency $n\omega$ is then given by:

$$C_{L_n} = \frac{2\pi}{\sqrt{1-M^2}} \frac{C_n}{V_\infty} e^{(in\omega t + \phi_n)} \varphi(nk). \tag{54}$$

where:

$$C_n = \sqrt{A_n^2 + B_n^2} \tag{55}$$

and:

$$\phi_n = \tan^{-1}\left(-\frac{B_n}{A_n}\right) \tag{56}$$

Summing the lift response for all of the angular frequencies $n\omega$ gives the lift response function for a general gust:

$$C_{L_{g,osc}} = -\frac{2\pi}{\sqrt{1-M^2}} \frac{e^{i\omega t}}{V_\infty} \sum_{n=1}^{\infty} \Big\{ A_n \cos(n\omega t) + B_n \sin(n\omega t) \Big\} \varphi(nk). \tag{57}$$

III.3.2.3 Calculation of the Sinusoidal Gust of a Propeller Blade Segment

To obtain the unsteady lift on the blade segment of a counterrotating propeller, the variation of the vertical component $W_{\text{gust}}(t)$ must be obtained. This is taken as the variation of the induced velocity component normal to the resultant velocity, W as shown in Fig. 8.

A counterrotating blade segment is assumed in the Davidson method to be subjected to three induced velocity components, as discussed previously. These are w_1 which is the velocity induced on a propeller by itself, and $u(t)$ and $v(t)$ which are the velocity components induced on a blade segment by the other propeller. As with a single-disk propeller, the self-induced velocity w_1 will be assumed to be constant.

The variation of $u(t)$ and $v(t)$ is taken from the induced velocity calculations using the modified approach of Lesieutre for a counterrotating propeller.

The induced velocity components $u(t)$ and $v(t)$ are the axial and tangential induced velocity components, respectively. They are obtained from the induced velocity components u_1, u_2, and u_3 by:

$$\begin{aligned} u(t) &= u_1(t)\sin\psi - u_2(t)\cos\psi, \\ v(t) &= u_3(t), \end{aligned} \tag{58}$$

where ψ is the angle which the blade makes with the horizontal and is given by:

$$\psi = \omega t \tag{59}$$

From Fig. 2, it can be shown that the flow angle, $\phi(t)$, is equal to:

$$\tan\phi(t) = \frac{V_\infty + u(t) + w_1\cos\phi(t)}{r\Omega - v(t) - w_1\sin\phi(t)}. \tag{60}$$

This equation can be rewritten as:

$$(r\Omega - v(t))\sin\phi(t) - (V_\infty + u(t))\cos\phi(t) - w_1 = 0. \tag{61}$$

The instantaneous value of $\phi(t)$ is obtained by solving Eq. (61) for $\phi(t)$ using the induced velocity components $u(t)$ and $v(t)$ as calculated. The blade twist angle θ is then subtracted from $\phi(t)$ to obtain the angle of attack of the airfoil, as in Eq. (19). Finally, the vertical velocity component $W_{\text{gust}}(t)$ is calculated with:

$$W_{\text{gust}}(t) = V_\infty \tan\alpha(t) \tag{62}$$

This calculation is repeated at several discrete times over the blade loading period, T_L to obtain the vertical component of the velocity as a function of time. This velocity variation is then used with Eq. (57) to calculate the unsteady loads.

III.4 Acoustic Analysis

To obtain the acoustic signature of a rotating propeller, each blade is assumed to be divided in the radial and chordwise directions. This results in a number of acoustically compact blade segments, shown in Fig. 11. The acoustic compactness requirement is met by dividing the blade into segments whose maximum dimension is much smaller than their closest distance to the observer. Bumann[35] has shown that the exact number of radial and chordwise divisions has relatively little effect on the noise characteristics because the dimension of the blade segments is much smaller than the wavelength of the emitted sound. The volumes, velocities, and aerodynamic loads on each of these segments are then used with Eqs. (8), (9), and (10) to obtain the acoustic pressure at the observer time created by a given blade segment. This calculation is repeated for each compact source on the propeller for a given observer time t to obtain the total acoustic pressure. This procedure is repeated for many discrete observer times over the period T to obtain the acoustic pressure time-history.

To convert the periodic acoustic pressure time-history to a frequency spectrum, a standard Fourier Series representation is used, i.e.:

$$p(t) = \frac{A_0}{2} + \sum_{n=1}^{\infty} A_n \cos(n\omega t) + \sum_{n=1}^{\infty} B_n \sin(n\omega t), \tag{63}$$

where:

$$\begin{aligned} A_n &= \frac{2}{T}\int_0^T p(t)\cos(n\omega t)dt, \\ B_n &= \frac{2}{T}\int_0^T p(t)\sin(n\omega t)dt. \end{aligned} \tag{64}$$

The acoustic pressure at each harmonic is then given by:

$$C_n^2 = (A_n^2 + B_n^2)/2, \tag{65}$$

and the sound pressure level (SPL) at the n^{th} harmonic is given by:

$$\mathrm{SPL}_n = 10\log_{10}\left(\frac{C_n}{P_{\mathrm{ref}}}\right)^2, \tag{66}$$

where the reference pressure, P_{ref}, is taken as $20\,\mu$Pa. The OASPL may then be computed from:

$$P_{\mathrm{rms}}^2 = \frac{1}{T}\int_0^T p^2(t)\,dt, \tag{67}$$

$$\mathrm{OASPL} = 10\log_{10}\left(\frac{P_{\mathrm{rms}}}{P_{\mathrm{ref}}}\right)^2, \tag{68}$$

or

$$\mathrm{OASPL} = 10\log_{10}\sum_{n=1}^{\infty} 10^{\left(\frac{\mathrm{SPL}_n}{10}\right)}. \tag{69}$$

In conclusion, the acoustics of a counterrotating configuration are obtained by calculating the mean performance of the blade with the Davidson method. Then, the unsteady loads are obtained with a modified formulation of the Lesieutre method for counterrotating propellers. Finally, the noise characteristics are obtained with the compact acoustic source model of Succi. The next two Chapters will present comparisons of the theoretical noise model with experimental acoustic measurements, and a study of the directivity patterns of the acoustic emissions of a hypothetical commuter-class counterrotating propeller configuration.

CHAPTER IV

COMPARISONS WITH EXPERIMENT

Numerical computer programs were already available to perform two of the three components of the approximate acoustic prediction methodology detailed in the previous Chapter. These consisted of the counterrotating performance prediction scheme of Davidson and the compact acoustic source model of Succi. In addition, the modified method of Lesieutre was written into a numerical analysis to predict the unsteady forces on a counterrotating propeller configuration. Each of the three computer programs was written or modified to run independently while either generating data files to be used by another program or making use of data previously available.[36] Thus employed, the theoretical acoustics of a counterrotating propeller can be quickly and easily predicted once the geometry and flight conditions are known.

In an effort to corroborate this approximate acoustic method, theoretical acoustic predictions are compared with experimental acoustic measurements of a counterrotating propeller configuration. These experimental measurements were conducted in the Texas A&M University 5×6 ft. open-return subsonic wind tunnel by Gazzaniga.[37] The configuration consisted of two propellers 20 inches in diameter operating at the same RPM. The wind tunnel was powered by a five blade constant-speed propeller operating at 1200 RPM, and generated a flow velocity of 147 fps. In order to inhibit acoustic reflections, the walls of the tunnel were lined with one-inch sheets of 4 lb/ft^3 polystyrene and 60° polystyrene wedges aligned with the flow direction as shown in

Fig. 12. Acoustic measurements of this arrangement indicated efficient low frequency absorption with a gradual efficiency decrease below 400 Hz.

The composite blades used in the Counterrotating Propeller Test Rig (CRPTR) consisted of 27 layers of graphite and fiberglass cloth. These were modeled after commercially-available aircraft propellers and modified in the shank region. Blade geometry is shown in Figs. 13 through 16, and the untwisted or developed blade planform in Fig. 17. The propellers were powered by an air turbine rated at 55 horsepower at 16,000 RPM, and instrumentation employed to monitor the configuration included pressure transducers for the inlet and exhaust, accelerometers to detect vibrations, tachometers to measure shaft RPM, and thermocouples for turbine inlet/exhaust temperature(s). For a discussion of the acoustic test facility, the CRPTR, and details of the experimental measurements, the reader is referred to Gazzaniga.

Noise levels and frequency spectra for this configuration were measured experimentally at two observer locations, i.e. 2.25 inches from the propeller tip in the disk-plane, and 9.25 inches in front of the disk-plane on the axis of rotation, as shown in Fig. 18. Acoustic measurements were made over a range of rotations speeds from approximately 3,000 to 6,000 RPM, corresponding to advance ratios of 1.76 to 0.88. Comparison between the experimental measurements and theoretical predictions obtained using the method described in the previous Chapter will be presented for the three blades front-and-aft and the four blades front-and-aft counterrotating propeller configurations.

IV.1 Three-by-Three Propeller Configuration

Theoretical performance calculations were made for the three-by-three blade counter-rotating propeller configuration using the Davidson performance method as previously described. Blade tip angles were varied from 40° to 50° in five degree increments,and advance ratios over a range from 0.6 to 1.6. These limits were selected to correspond approximately with the acoustic measurements made by Gazzaniga. The maximum efficiency was seen to vary inversely with the blade tip angle (Fig. 19), with a peak efficiency of approximately 92 percent at 40° and decreasing to 87 percent at the 50° blade tip angle. In addition, the typical flat efficiency curve expected for counterrotating propeller configurations was noted, i.e the propulsive efficiency was relatively independent of rotation speeds over a wide range of advance ratios.

The thrust and power coefficients of the 3×3 configuration are seen to be directly proportional to the blade tip angle for a given advance ratio as shown in Figs. 20 and 21. In addition, the thrust coefficient and power coefficient are seen to be inversely related, i.e., C_T decreases and C_P increases with advance ratio over the range noted. This behavior is due to the change of the direction of the blade lift vector with varying rotation speed. For example, as advance ratio decreases, the flow angle ϕ decreases and the lift vector points in a more axial direction (see Eq. (18)). Since the differential thrust is dependent upon $\cos\phi$, the decrease of ϕ due to a decreased advance ratio results in more thrust. Similarly, the differential torque, related to the power-absorbed, is related to $\sin\phi$, and the decrease in ϕ results in less power absorbed.

IV.1.1 Disk-Plane Noise Characteristics

Theoretical predictions of the acoustics in the disk-plane of the three blade front-aft counterrotating propeller configuration were made at combinations of blade tip angle and advance ratio selected to match those used in the acoustic measurements of Gazzaniga. The microphone, designated the x-microphone, was located 2.25 inches beyond the tip of the propellers in the disk-plane, which lies midway between the front and aft planes of rotation as shown in Fig. 18 At the 40° blade tip angle, the predicted OASPL demonstrated acceptable agreement with the experimentally measured values as given in Fig. 22. Both the experimental and theoretical noise levels demonstrate a slight decrease with an increase in advance ratio. This is expected since the advance ratio varies inversely with rotation speed and a slower-rotating propeller is expected to generate less noise. At blade tip angles of 45° and 50°, the same inverse relationship between noise level and advance ratio is observed as shown in Figs. 23 and 24. However, the theoretical predictions and experimental measurements begin to diverge at the higher advance ratios. This behavior was noted by Bumann for single-disk propellers in comparisons between theoretical acoustic predictions using the model of Succi and the experimental measurements of Gazzaniga.

Comparison of typical theoretical and experimental frequency spectra is made in Fig. 25 at a 40° blade tip angle and an advance ratio of 0.86. This reveals that the SPL of the fundamental is in excess of the experimentally determined value by approximately six percent. Since the fundamental tends to dominate the total noise level, OASPL is overpredicted.

IV.1.2 On-Axis Noise Characteristics

Additional acoustic measurements were made with a microphone located upstream from the CRPTR configuration 9.25 inches from the disk-plane on the axis of rotation. This is referred to as the y-microphone and is shown in Fig. 18. Theoretical predictions and experimental measurements are shown in Figs. 26 through 28 for three blade tip angles and a range of advance ratios. As contrasted with the x-microphone, the theoretical noise levels are less than the experimental values by three to five decibels. However, the trend of decreasing noise level with increasing advance ratio is also demonstrated.

Finally, Fig. 29 shows the comparison of the experimental and theoretical frequency spectra under the same operating conditions as Fig. 25. While there is significant disagreement between theory and experiment for the frequency spectra, the important feature to note is that only the even harmonics are present. In the theoretical predictions, the odd harmonics are practically nonexistent, having SPL magnitudes of approximately zero dB. In the experimental measurements, the odd harmonics are indistinguishable from the broadband or background noise and it is not possible to determine their exact magnitudes. However, these odd harmonics are small enough to be insignificant when compared to the even harmonics. Despite the lack of agreement between the experimental and theoretical frequency spectra, it is encouraging that the absence of the odd harmonics is theoretically predicted.

This result contrasts significantly with the on-axis noise of a single-disk propeller, wherein the theoretical noise level is zero. This result was confirmed experimentally by Gazzaniga with no discernible harmonics showing above the background

noise. As will be discussed, the reason for the presence of the even-numbered harmonics in the counterrotating configuration is due to the time-dependent loads on the propeller blades.

IV.2 Four by Four Propeller Configuration

As with the 3×3 blade configuration, theoretical performance calculations were made for a 4×4 blade configuration over the same ranges of blade tip angles, namely 40° to 50°, and advance ratios of 0.6 to 1.6. The maximum efficiency was approximately 94 percent and 90 percent for the 40° and 50° blade tip angles, respectively, as shown in Fig. 30. Compared to the 3×3 counterrotating propeller configuration, this resulted in an improvement of the operating efficiency of two to three percent.

In addition, the thrust and power coefficients of the 4×4 configuration are seen to be behave similarly to those of the 3×3 configuration as shown in Figs. 31 and 32. At a given blade angle and advance ratio, the thrust and power coefficients are seen to be approximately 15 to 30 percent higher than the corresponding values for the 3×3 propeller configuration. Since the pitch of the experimental propeller blades is constant, this result is directly attributable to the presence of the additional blade on each disk of the 4×4 combination.

IV.2.1 Disk-Plane Noise Characteristics

Theoretical noise levels in the disk-plane were calculated for the 4×4 blade arrangement at blade tip angles and advance ratios to duplicate the experimental conditions of Gazzaniga and are compared in Figs. 33 through 35. Slightly better agreement

was seen between the theoretical and experimental OASPL than for the 3 × 3 propeller configuration. However, the theoretical noise levels are still in excess of the experimental noise levels by approximately two to four decibels. Comparison of the theoretical and experimental frequency spectra for the 40° tip angle case at J=0.98 shown in Fig. 36 reveals acceptable agreement among the first three harmonics with divergence in the higher harmonics. The fundamental is over-predicted by approximately four decibels, accounting for the overprediction of the OASPL as contrasted with the experimentally measured noise levels. This behavior was typical for all of the theoretical and experimental frequency spectra.

The theoretical underprediction of the higher harmonics appears to be the result of the simplicity of the unsteady model. This was noted in the previous Section in the comparison of the on-axis frequency spectra, to which only the unsteady noise levels contribute. This result could be a consequence of the approximate nature of this noise model.

IV.2.2 On-Axis Noise Characteristics

Comparable results were obtained for the on-axis or y-microphone noise characteristics of the 4 × 4 blade configuration as for the 3 × 3 configuration. The trend of the decrease of noise level with increasing advance ratio was followed, except that the total noise was underpredicted by five to eight decibels as given in Figs. 37 through 39. Comparison of the frequency spectra for the 40° tip angle case shown in Fig. 40 indicates the expected behavior, i.e., the odd harmonics are eliminated, the second harmonic is relatively small, and the higher even harmonics dominate the noise.

The results of this comparison between the theoretical and experimental noise levels are mixed. In the disk-plane of the propeller, the theoretical noise levels tend to overpredict experimental values by approximately two to five decibels. This is within the range of acceptable agreement. However, on the axis of rotation the agreement is poor with noise levels differing by approximately three to eight dB.

There are several possible explanations for the differences in the theoretical predictions and experimental measurements of the acoustic characteristics. First, the data bank used in the model of Davidson to calculate the steady performance of the experimental counterrotating propeller configuration was written for NACA four digit airfoils and taken from a work by McCormick.[38] Examination of the cross-sections of the propeller blades used by Gazzaniga reveal that the trailing edges of the airfoil sections are considerably rounded. At radial stations near the blade tip, the trailing edge radius is of the same order of magnitude as the leading edge. The lack of a sharp trailing would tend to significantly decrease the lift force on the blades of the experimental propeller. In addition, the blades would be expected to stall at lower angles of attack. Examination of the radial angle of attack distributions calculated by the Davidson performance method revealed that α commonly varied between approximately -5 degrees at the hub to $+12$ degrees at the tip at most operating conditions. The McCormick airfoil data bank does predict maximum lift coefficient for a NACA four digit airfoil, however the maximum lift coefficients of the experimental blade segments are expected to be less.

The effect of an overprediction of the lift force on the noise level is seen by examining the equation of Succi for the loading noise, e.g. Eq. (9). The variation

of the acoustic pressure, P_{rms}, linearly depends on the forces on the blade segment. However, the noise level is related to the logarithm of the square of the root-mean-square pressure, by:

$$\text{OASPL} = 10 \log_{10} \left(\frac{P_{\text{rms}}}{P_{\text{ref}}} \right)^2 \tag{70}$$

Consequently, any error in predicting the loads on the propeller are significantly amplified in calculating the noise level. For example, assume that the loads on the propeller blade are uniformly overpredicted by 30 percent, a realistic result if the blades are either not generating their full lift due to a rounded trailing edge or are prematurely stalled due to operating at excessive angles of attack. In this case, the the root-mean-square pressure will be in error by 69 percent, which translates to an overprediction of the noise level by 2.3 dB. This result indicates that the acoustics of a propeller are much more sensitive then the total performance, i.e. thrust and torque, to the loads on its blades.

A second possible source of disagreement between the theoretical and experimental noise levels is due to the CRPTR gearing arrangement of the front and aft propeller disks. In the experimental investigations of Gazzaniga, the propellers were made to rotate at the same speed. However, they were powered by separate sources and no mechanism was used to insure that the blades maintained their relative orientation to each other. In the theoretical model, it was assumed that the two blades of the front and aft propellers passed the x-microphone located in the disk-plane at the same time. That is, that the front and aft blades were in phase with each other. If, however, the blades were out of phase in the experimental measurements, this would

result in partial cancellation of the acoustic pressure from the front and aft propellers and a consequent decrease in the noise level.

A third possible explanation for the difference in the noise levels lies in the application of the Sears function $\varphi(k)$ to the propeller blades. The assumption in the formulation of the unsteady loads prediction technique developed by Sears is that the entire airfoil at a particular radial station is subjected to the same induced velocity variation. For a two-dimensional airfoil, a reference point other than the mid-chord could be selected and the appropriate equations, e.g. Eq. (54), multiplied by a phase relationship. This would not affect the magnitude of the unsteady lift, only the phase relationship. However, the magnitude of the velocity variations as calculated with the modified method of Lesieutre depend on the distance of the reference point on the chord of the blade segment from a vortex. As given by the Biot-Savart Law (Eq. (28)), the induced velocity varies inversely with the square of this distance. Due to the close proximity of the front and aft blades in a counterrotating propeller configuration, the selection of the reference point is significant to accurately obtain the unsteady loads. It is suggested that a future study be performed to examine the sensitivity of this acoustic model to the airfoil data bank implemented, the phase relationship of the front and aft propellers, and the selection of the blade reference point employed in unsteady performance calculations.

In an effort to explain the reasons for the disappearance of the odd harmonics in the frequency spectra of observer locations on the axis of rotation, the equations of Succi were examined. The results of this investigation are presented in the next

Section, examining the sensitivity of the noise levels in the disk-plane and on the axis of rotation to the steady and unsteady propeller loads.

IV.3 Contribution of Steady and Unsteady Forces to the Directional Noise Characteristics

In an effort to explain the behavior of the odd and even harmonics of the counterrotating propeller noise, the Succi formulation for the acoustic loading noise of compact acoustic sources was examined. The loading noise of a compact acoustic source is seen to depend both on its motion relative to the observer and the forces which it imparts to the surrounding fluid. Equation (9), which gives the acoustic pressure for one compact acoustic source, is repeated here for convenience:

$$4\pi p_{L_n}(\vec{x},t) = \left\{ \frac{1}{(1-M_r)^2 r}\left[\frac{\hat{r}_i}{a_0}\cdot\frac{\partial \vec{F}_i}{\partial \tau} + \frac{(\hat{r}_i\cdot\vec{F}_i)}{(1-M_r)}\left(\frac{\hat{r}_i}{a_0}\cdot\frac{\partial \vec{M}_i}{\partial \tau}\right)\right] \right.$$
$$\left. + \frac{1}{(1-M_r)^2 r^2}\left[(\hat{r}_i\cdot\vec{F}_i)\frac{(1-\vec{M}_i\cdot\vec{M}_i)}{(1-M_r)} - \vec{F}_i\cdot\vec{M}_i\right]\right\}_{\text{ret}},$$

The contribution of the loading noise terms, p_L, to the acoustic pressure experienced by an observer is found in the three terms:

$$\begin{aligned} &(a) \quad \hat{r}_i\cdot\frac{\partial \vec{F}_i}{\partial \tau}, \\ &(b) \quad \hat{r}_i\cdot\vec{F}_i, \\ &(c) \quad \vec{F}_i\cdot M_i. \end{aligned} \tag{71}$$

The forces on a compact source are denoted by $\vec{F}_i$, and consist of the thrust force, F_T, acting in the direction of the axis of rotation, and the torque-force, F_Q, which acts in a direction opposite to the rotation of the source.

If the source rotates at a distance R from the axis as shown in Fig. 1, and its angular location is given by $\psi = \omega\tau$, the force vector $\vec{F}_i$ is written as:

$$\vec{F}_i = \begin{pmatrix} F_Q \sin(\omega\tau) \\ -F_Q \cos(\omega\tau) \\ F_T \end{pmatrix}, \tag{72}$$

with its time derivative:

$$\frac{\partial \vec{F}_i}{\partial \tau} = \begin{pmatrix} F_Q \omega \cos(\omega\tau) + \frac{\partial F_Q}{\partial \tau} \sin(\omega\tau) \\ F_Q \omega \sin(\omega\tau) - \frac{\partial F_Q}{\partial \tau} \cos(\omega\tau) \\ \frac{\partial F_T}{\partial \tau} \end{pmatrix}.$$

The position of the source is given by:

$$\tilde{y} = \begin{pmatrix} R\cos(\omega\tau) \\ R\sin(\omega\tau) \\ 0 \end{pmatrix}, \tag{73}$$

and the observer location will be denoted as:

$$\tilde{x} = \begin{pmatrix} x_o \\ y_o \\ z_o \end{pmatrix}. \tag{74}$$

Now, the vector from the source to the observer $\tilde{r}$ is given by:

$$\tilde{r} = \tilde{x} - \tilde{y} = \begin{pmatrix} x_o - R\cos(\omega\tau) \\ y_o - R\sin(\omega\tau) \\ z_o. \end{pmatrix} \tag{75}$$

The magnitude of $\tilde{r}$ is equal to:

$$r = |\tilde{r}| = \left\{ \Big[x_o - R\cos(\omega\tau)\Big]^2 + \Big[y_o - R\sin(\omega\tau)\Big]^2 + z_o^2 \right\}^{1/2}, \tag{76}$$

and its unit vector is:

$$\hat{r}_i = \frac{\tilde{r}}{r}. \tag{77}$$

Finally, the Mach number of the rotating source, $\vec{M}_i$, is given by:

$$\vec{M}_i = \frac{1}{a_0}\frac{\partial \tilde{y}}{\partial \tau} = \frac{1}{a_0}\begin{pmatrix} -R\omega\sin(\omega\tau) \\ R\omega\cos(\omega\tau) \\ 0 \end{pmatrix}. \tag{78}$$

After substituting these relationships into Eq. (71), the three terms (a), (b), and (c) which contain the effects that the forces on the moving source have on the acoustic pressure become:

$$(a) \quad \hat{r}_i \cdot \frac{\partial \vec{F}_i}{\partial \tau} = \frac{1}{r}\Big\{ F_Q \omega \Big[x_o \cos(\omega\tau) + y_o \sin(\omega\tau) - R \Big] + \frac{\partial F_Q}{\partial \tau}\Big[x_o \sin(\omega\tau) - y_o \cos(\omega\tau) \Big] + z_o \frac{\partial F_T}{\partial \tau} \Big\}, \tag{79}$$

$$(b) \quad \hat{r}_i \cdot \vec{F}_i = \frac{1}{r}\Big\{ F_Q \Big[x_o \sin(\omega\tau) - y_o \cos(\omega\tau) - R \Big] + F_T z_o \Big\}, \tag{80}$$

and

$$(c) \quad \vec{F}_i \cdot M_i = -\frac{F_Q R \omega}{a_0}. \tag{81}$$

Having presented the equations which describe the contribution of the forces on a rotating acoustic source to the acoustic pressure time-history, the next subsections will examine the significance of each of these terms on the noise level experienced by an observer either in the disk-plane or on the axis of rotation.

IV.3.1 Noise Characteristics in the Disk-Plane

For an observer located in the plane of the propeller disk, i.e., the $x-y$ plane shown in Fig. 1, the coordinate location z_o is zero. Therefore, eliminating this term in Eqs. (79) through (81) gives:

$$(a) \quad \hat{r}_i \cdot \frac{\partial \vec{F}_i}{\partial \tau} = \frac{1}{r}\Big\{ F_Q \omega \Big[x_o \cos(\omega\tau) + y_o \sin(\omega\tau) - R \Big] + \frac{\partial F_Q}{\partial \tau}\Big[x_o \sin(\omega\tau) - y_o \cos(\omega\tau) \Big] \Big\}, \tag{82}$$

$$(b) \quad \hat{r}_i \cdot \vec{F}_i = \frac{1}{r}\Big\{ F_Q \Big[x_o \sin(\omega\tau) - y_o \cos(\omega\tau) - R \Big] \Big\}, \tag{83}$$

$$(c) \quad \vec{F}_i \cdot M_i = -\frac{F_Q R\omega}{a_0}. \tag{84}$$

Note that the thrust term F_T has been eliminated. This is because for an observer in the disk-plane, the thrust vector is at right angles to the vector $\hat{r}_i$. Therefore, when the inner product of these two terms is taken, the thrust disappears.

To understand the contribution of these three terms to the noise characteristics, it must be understood that noise consists of pressure fluctuations in a fluid about a mean value. The level of the noise is proportional to the magnitude of the fluctuations, and its frequency characteristics are defined by the frequency of the fluctuations. Therefore, information concerning the relative contributions of the thrust and torque forces on the blade to the noise characteristics in the disk-plane can be had by examining the amplitude and frequency characteristics of the terms in the preceding Equations.

The magnitude of the contributions to the noise level are determined by the magnitudes of the terms in Eqs. (82) through (84). Examination of these Equations indicates that the (a) is several orders of magnitude larger than Term (b), which lacks the angular frequency, ω, and term (c), which is divided by the speed of sound, a_0. Although $\frac{\partial F_Q}{\tau}$ can be several orders of magnitude larger than F_Q, the torque-force is multiplied by ω. Consequently, the level of the noise in the disk-plane is controlled by both the magnitude of the fluctuations of the torque-force and the magnitude of the fluctuations of its time-derivative.

The frequency characteristics of the noise in the disk-plane are defined by the frequency characterstics of (a). It has been noted that the torque-force is periodic over

the blade loading period, T_L. However, due to the presence of the trigonometric terms $\cos(\omega\tau)$ and $\sin(\omega\tau)$, this equation is periodic over one revolution of a propeller blade. When several blades are present, their pressure time-histories are out of phase by an amount proportional to the blade passing period. Consequently, when the pressure time-histories of these blades are summed, the result is an acoustic pressure that is periodic over one blade passing period. This will result in pressure fluctuations at frequencies that are multiples of the fundamental frequency and hence at all integer harmonics.

It has been shown that the noise level generated in the disk-plane by a counterrotating propeller is dependent primarily on the magnitude of torque-force and its time derivative. Also, this noise will manifest itself in the harmonics of the blade passing frequency. The next Section will examine the contribution of the blade forces to the acoustic characteristics on the axis of rotation.

IV.3.2 Noise Characteristics on the Axis of Rotation

For an observer located on the axis of rotation, corresponding to the z-axis in Fig. 1, the coordinates x_o and y_o become zero. Consequently, Eqs. (79) through (81) reduce to:

$$(a) \quad \hat{r}_i \cdot \frac{\partial \vec{F}_i}{\partial \tau} = \frac{1}{r} z_o \frac{\partial F_T}{\partial \tau}, \tag{85}$$

$$(b) \quad \hat{r}_i \cdot \vec{F}_i = \frac{1}{r} z_o F_T. \tag{86}$$

$$(c) \quad \vec{F}_i \cdot M_i = -\frac{F_Q R \omega}{a_0}. \tag{87}$$

As before, the largest contribution to the noise level comes from (a), the the time-derivative of the thrust force, $\frac{\partial F_T}{\partial \tau}$. F_T is several orders of magnitude smaller

than its derivative, and term (c) is divided by the speed of sound. Since no geometric terms are present, the frequency of the noise on the axis of rotation is that of F_Q. Consequently, the noise for an observer in this regions will be present at integer multiples of the blade loading frequency, T_L, which are the even harmonics of the blade passing frequency.

The result of this investigation of the unsteady and steady force contribution to the noise level of a counterrotating propeller configuration leads to two important observations. First, the noise level on the side of the propeller is dependent both on the magnitude of the fluctuations of the torque-force on the propeller as well as on the fluctuation of its time-derivative. On the axis of rotation, the noise is generated by the derivative of the thrust force. Since the blade loading frequency is twice the blade passing frequency, this noise is present only in the even harmonics.

In conclusion, it appears that this approximate acoustic model is useful to predict the noise level in the disk-plane of the propeller, and the characteristics of the frequency spectra both in the disk-plane and on the axis of rotation. Also, the trend of the variation of the OASPL with changes in advance ratio and blade tip angle is followed. Since the performance of the experimental counterrotating propeller configuration was not measured by Gazzaniga, it cannot be concluded that the acoustic segment of this theoretical noise model was deficient. That is, it may prove that if the performance of a counterrotating propeller configuration is more accurately known, better theoretical agreement with experiment would result. Consequently, further comparison of this model against counterrotating propeller configurations with known performance is suggested.

As indicated, this model appears to correctly predict the relative magnitude of the OASPL at different observer locations and varying operating conditions. Consequently, it was decided to investigate in more detail the behavior of the noise characteristics around a hypothetical commuter-class aircraft counterrotating propeller configuration. The directivity patterns of the frequency spectra are examined in both the horizontal and vertical planes and at several advance ratios.

CHAPTER V

THEORETICAL ACOUSTICS OF COUNTERROTATING COMMUTER PROPELLER DESIGN

To further investigate the applicability of this model, the performance and acoustics of a hypothetical counterrotating propeller configuration for a commuter-class aircraft were examined. This Chapter will present documentation and discussion of calculations resulting from the various steps in the approximate acoustic model, and investigate the variation and directivity of the noise level in several regions around the counterrotating propeller. First, the performance of the configuration is analyzed for three advance ratios. Then, the variation of the noise level in a plane around the propeller is examined. Next, the theoretical frequency spectra along a line one diameter from and parallel to the axis of rotation are examined, as well as the variation of the frequency spectra at varying radial distances in the disk plane. Finally, the directivity of the frequency spectra is examined in the vertical disk plane, followed by the directivity in the horizontal plane. Figure 41 shows the locations of the horizontal and disk planes.

Using the design method as described by Davidson, a counterrotating propeller for a commuter-class aircraft was designed for the following operating conditions and geometry: four-blade propeller, 7.5 ft in diameter; 1500 RPM, corresponding to a helical tip Mach number of 0.71; 900 h.p. per engine (two); and 500 fps flight speed at 10,000 ft. altitude under standard atmosphere conditions. The radial thickness-to-chord radio and design lift coefficient variation was selected as shown in Figs. 42

and 43. A NACA 16 series airfoil data bank was employed to model the blade segment performance.[39] The geometry of the resulting propeller design is shown in Figs. 44 and 45, with the corresponding radial chord and blade twist variation indicated.

V.1 Performance of Counterrotating Propeller Configuration

The performance of the commuter-class configuration was calculated for a range of advance ratios with the configuration operating as a constant-speed propeller; i.e., with propeller blades which rotate in the hub to absorb the provided horsepower. The advance ratio was varied by changing the flight speed with all other conditions remaining the same. The efficiency reaches a maximum of 93.5 % at the design advance ratio of 2.67 as indicated in Fig. 46, and decreases slowly with varying advance ratio. This ηvs.J curve is much flatter and smoother than would be the case for a single-disk propeller, and is indicative of the better off-design performance of a counterrotating propeller configuration. Similarly, the thrust coefficient given in Fig. 47 shows the expected behavior with varying advance ratio.

The radial distribution of differential thrust and torque-force obtained from the Davidson performance method for three advance ratios are contained in Figs. 48 through 51. The thrust distribution varies smoothly from nearly zero at the tip to a maximum at approximately the 0.75 radial station, and decreases to zero at the tip. Note that the magnitude of the differential thrust decreases with an increase in advance ratio, explaining the decrease in the thrust coefficient, C_T. In addition, the area under the differential thrust curves, which is in effect the total thrust of the propeller, is larger for the back propeller (Fig. 50) than for the front (Fig. 48). This is

typical for a counterrotating propeller configuration, since much of the energy of the front propeller is lost in the form of a rotational velocity component imparted to the fluid, whereas the aft propeller tends to straighten the flow and recover a significant percentage of the lost energy. In contrast, the differential torque-force distribution of either propeller is relatively unaffected by changes in advance ratio as shown in Figs. 51 and 49. This is the result of the constant-speed propeller blades absorbing the same horsepower at all three advance ratios.

Finally, the radial distribution of the lift coefficient, C_L, and circulation, Γ, are indicated for both propellers (Figs. 52 through 55). The spike in the lift coefficient near the tip is necessary to generate a proper circulation distribution. This may be explained since the chord of the propeller diminishes quickly in the tip region, and must be offset with the higher C_L to ensure a smoothly varying Γ as indicated by Eq. (39). Examples of the three components of the induced velocities of both the front and aft propellers are given as calculated with the method of Sullivan and Lesieutre (Figs. 56 through 61). These velocities are calculated for the 75 % radial station over one complete rotation of both propellers under design operating conditions. It is important to note the phase relationship of the velocity components u_1 and u_2, shown in Fig. 7. These velocity components are at right angles to each other and are hence related by:

$$u_1(t) = u_2(t + T)$$

where T is the blade passing period. For a 4×4 blade configuration, this is the amount of time which elapses during one fourth of a revolution. In addition, the

induced velocity components components have the properties:

$$u_1(t) = -u_1(t + 2T)$$

and:

$$u_2(t) = -u_2(t + 2T).$$

It will be noted that the velocity component u_3, which is the induced velocity in the axial direction, undergoes eight periodic repetitions during one complete rotation.

Finally, the variation of the induced velocities between the front and aft propellers is significant. Since the aft propeller operates in the wake of the front propeller, the induced velocities on the aft propeller blades are seen to vary much less smoothly than those on the front. This would indicate that the unsteady noise from the aft propeller is higher than on the front.

Using the relationships of Eq. (62), the time-variations of the vertical velocity component, $W_{\text{gust}}(t)$, experienced by the front and aft blade segments at the 75 % radial station are shown in Figs. 62 and 63. Note that the vertical velocity components of the front and aft propellers are inversely related, i.e., when the front propeller blade segment experience an increasing vertical velocity component, the corresponding segment on the aft propeller experiences a decreasing vertical velocity component. Consequently, the variation of the angle of attack and hence lift force on the front and aft blades tend to have opposite signs.

As discussed in the previous Chapter, the vertical velocity components experienced by the blade segments can be converted to a quasi-steady lift-coefficient, $\Delta C_{L_{\text{QS}}}$, by:

$$\Delta C_{L_{\text{QS}}}(t) = \frac{2\pi}{\sqrt{1 - M^2}} \tan^{-1}\left(\frac{W_{\text{gust}}(t)}{W}\right)$$

with the results shown in Figs. 64 and 65 for the 75 % radial station of both propellers. Also indicated are the results of the application of the Sears function, $\varphi(k)$, which significantly reduces the magnitude of the unsteady lift force. This is due to the small real component of $\varphi(k)$ by which the quasi-steady lift coefficient is multiplied. The unsteady loads of similar configurations as calculated by Lesieutre tend to be greater in magnitude than the unsteady loads presented here since only the incompressible Sears function was employed by Lesieutre. The approximations of $\varphi(k)$ for compressible Mach numbers used in this acoustic model have a smaller real component than the incompressible two-dimensional Sears function and reduce the amplitude of the unsteady forces by a corresponding amount.

The unsteady fluctuations of the thrust and torque-force of the front and aft propellers are shown in Figs. 66 through 69 as functions of radial angular blade position. The time interval is one blade passing period. That the blade loading period is half the blade passing period is noted since the variation of the unsteady loads is repeated twice during one blade passing period. Also, it will be noted again that the magnitude of the unsteady forces are greatest in the middle segment of the blades and decreases near the hub and tip. This trend corresponds to the radial variation of the steady thrust and torque-force shown in Figs. 48 through 51. Finally, the hub and tip regions of the aft propeller experience a large load fluctuation that the hub and tip of the front propeller do not. This appears to be caused by the vortex sheet of the front propeller through which the aft propeller passes. This strength of this vortex sheet is proportional to the radial variation of the circulation Γ along the blades.

V.2 Theoretical Near Field Noise Levels

The OASPL and frequency spectra for the commuter-class counterrotating propeller configuration were examined in detail to ascertain the behavior of the total noise levels and the harmonics at varying distances and directions from the configuration. The noise levels were examined for three advance ratios: 2.13, the design condition of 2.67, and 3.20. These advance ratios correspond to flight velocities of 400, 500, and 600 fps, respectively. The propeller blades, as before, were allowed to rotate in the hub to absorb the horsepower provided by the engines.

Figures 70 through 72 show the near field OASPL for three advance ratios in a plane parallel to the axis of the propeller, i.e., in a region from four propeller radii upstream to four radii downstream, and from one radius to five radii in the radial direction. As expected, the noise level decreases as the observer location progresses away from the propeller. The obvious feature in each of these Figures is the extremely high noise level at an observer position at the tips of the front and aft propeller blades. The associated noise level is very high, corresponding to approximately 149 dB. Careful examination of these Figures also reveals that the noise level is higher in the region in front of the propeller than behind. This result is apparently due to slower propagation of the acoustic pressure upstream than downstream.

V.3 Noise Variation in Disk Plane

The acoustic characteristics of the commuter class counterrotating propeller configuration were determined along a line one blade diameter from and parallel to the axis of rotation, and from five radii upstream to five radii downstream. This line was

selected to correspond approximately to the location of the fuselage of an aircraft employing a counterrotating propeller configuration.

The first four harmonics of the frequency spectra at the selected advance ratios of 2.13, 2.67, and 3.20 are shown in Figs. 73 through 75. Examination of these Figures reveal that the first and third harmonics dominate in the region near the disk plane, and decrease as the observer location moves up and downstream. However, the second and fourth harmonics are significantly less affected by the axial location. Consequently, at points approximately three radii upstream and four radii downstream, the second and fourth harmonics exceed the magnitudes of the odd harmonics and dominate the noise characteristics in these regions.

OASPL was seen to be a maximum in the disk plane of the propeller configuration, and decreased as the observer location moved away from this plane (Fig. 76). Also, there is only a slight dependency upon advance ratio since the noise in and near the disk plane of the propeller depends primarily upon the torque force, which for a constant speed propeller is relatively independent of advance ratio. In addition, in the upstream region where the odd numbered harmonics begin to dominate the noise characteristics, the OASPL decreases less rapidly. Finally, the noise upstream is seen to be significantly less than that downstream. This result can be explained since the pressure fluctuations are "swept away" behind the propeller, but tend to propagate more slowly ahead of configuration since they must move against the oncoming fluid.

V.4 Sideline Noise

At the side of the configuration, the noise characteristics for the same three advance ratios were examined in the disk plane of the propeller, over a distance from one to

five propeller radii. Although at one radius, the distance is equal to the tip radius of the propeller, the observer is centered between the propeller blades and therefore non-zero distances to the propeller tips are avoided.

The behavior of the first four harmonics as a function of the radial distance is quite similar to that expected for a single-disk propeller as shown in Figs. 77 through 79, i.e., the relative magnitudes of the harmonics is inversely proportional to the harmonic number. In addition, the OASPL is seen to decrease uniformly with increasing distance from the axis of rotation (Fig. 80). Only a slight dependence on the advance ratio is evident, since this noise is dominated by the nearly constant torque-force of the counterrotating configuration.

V.5 Disk-Plane Directivity Pattern

As explained in the previous Section, the noise characteristics of the counterrotating configuration differ significantly depending upon the location of the observer. In the plane of the propeller disk (Fig. 41), the noise characteristics are similar to those of a single-propeller disk in that the relative magnitudes of the harmonics decrease uniformly with increasing distance from the propeller. However, the characteristics of the noise in the propeller disk for a counterrotating configuration differ from a single-disk propeller in the respect that the noise of a single disk propeller at a fixed radial distance from the axis of rotation is independent of the azimuthal angle. The only effect that azimuthal location has on the noise is seen in a phase shift of the pressure time history relative to the blade position which does not affect the overall noise level. In a counterrotating configuration, however, the phase relationship of the

the front and aft propellers is significant. For example, consider the front and aft propellers of a two-by-two configuration geared so that two blades always meet in a horizontal position. An observer is located in the disk plane in a plane containing the axis of rotation of the propeller (Fig. 81a). At this location, the sound fluctuations of two propeller blades will reach the observer at approximately the same instant of time, resulting in amplification of the sound. However, if the observer is located at the same distance but a different azimuthal angle (Fig. 81b), the blades will pass the observer at different times. Their sound fluctuations will tend to partially cancel each other and result in a lower noise level.

Given this observation, the azimuthal directivity of the counterrotating propeller noise was examined by calculating the acoustic characteristics for an observer located one propeller diameter from the axis of rotation and over a full circle. The noise characteristics were periodic over a 45° arc, and the predictions were repeated around the circle.

Figures 82 through 84 show the first four harmonics of the frequency spectra for the three selected advance ratios. These harmonics also reflect an eight-lobe directivity pattern. From Fig. 85, the significant dependence of the noise level on the azimuthal direction is evident. Since in the 4×4 configuration the front and aft blades meet at eight evenly-space azimuthal locations around a circle corresponding to integer multiples of 45°, an eight-lobed direction pattern is generated. Again, only a slight dependence on advance ratio is indicated.

V.6 Horizontal-Plane Directivity Pattern

The directivity pattern of the acoustic characteristics was also calculated in the horizontal plane (Fig. 41) at a distance of one propeller diameter from the intersection of the axis of rotation and the propeller disk plane.

From Figs. 86 through 88, it will be noted that the odd harmonics tend to dominate the acoustics in and near the disk plane. However whereas the magnitudes of the odd harmonics are comparable with those of the even harmonics in the disk plane, in the axis of rotation the odd harmonics are seen to drop off completely. This corroborates the behavior of the experimental frequency spectra in that the odd harmonics disappear, and the even harmonics define the noise characteristics on the axis of rotation.

The OASPL is seen to peak at locations on the axis and in the disk plane, with slight decreases in the intermediate locations as shown in Fig. 89. Also, the OASPL is relatively independent of advance ratio except in the region immediately upstream of the propeller on the axis of rotation. Due to the disappearance of the odd harmonics in this region, the magnitude of the overall noise level is a poor indicator of the acoustic characteristics.

In conclusion, a commuter-class counterrotating propeller configuration was designed with the method of Davidson. The near field acoustic spectra and OASPL are examined leading to several observations. On the side of the counterrotating propeller configuration near the disk plane, the acoustic characteristics are similar to those of a single disk propeller. That is, the levels of the harmonics decrease with

increasing radial distance. However, several differences are noted for the counterrotating configuration. The noise levels of the harmonics as well as the OASPL exhibit a distinct multi-lobed pattern in the disk-plane due to the phase relationship of the front and aft blades. In addition for observer locations near the axis of rotation, the odd harmonics significantly diminish whereas the even harmonics exhibit high noise levels. This result is due to their dependence in this region on the time-derivative of the thrust force on the blades.

CHAPTER VI

SUMMARY AND CONCLUSIONS

The analytical method of Davidson as modified by Korkan and Playle and Playle, et.al. was used to determine the steady performance of a counterrotating propeller configuration. A method based on the unsteady propeller performance method of Sullivan and Lesieutre was used to calculate the unsteady forces on the propeller configuration. Finally, the compact acoustic source methodology of Succi was used to predict the pressure time-history at a particular observer location.

Intially, the experimental acoustic measurements of Gazzaniga were used as a basis for comparison with the theoretical results of this method. Experimental acoustic measurements were made for a three-blade front-and-aft, and a four-blade front-and-aft configuration operating at blade tip angles of 40°, 45°, and 50° operating under a range of advance ratios from approximately 0.6 to 1.8. In the plane of the propeller disk, theoretical noise levels were found to exceed experimental measurements by approximately two to five decibels for the 3×3 and 4×4 configurations. On the axis of rotation, the theoretical noise levels were found to significantly underpredict the experimental results from eight to 15 decibels. In addition, the frequency spectra showed poor agreement. However, theoretical predictions and experimental measurements both indicate that the odd harmonics disappear from the frequency spectrum on the axis of rotation. Several explanations for the differences in the theoretical and experimental noise characteristics are presented.

The theoretical compact source model of Succi is examined in detail to determine the relative effects of the steady and fluctuating components of the blade forces on the noise characteristics. In the disk plane, the noise is found to depend on the magnitude of the torque-force. However near the axis of rotation, the noise is determined almost exclusively by the time-derivative of the thrust. The frequency spectrum is found to be based on the blade loading frequency, which is twice the blade passing frequency. This results in the disappearance of the odd harmonics for this region.

A hypothetical 4×4 blade commuter-class propeller configuration was designed with the method of Davidson, and the noise characteristics examined at several advance ratios. In addition, the directivity characteristics of the noise in the disk and horizontal planes are examined. In the disk plane, the lower harmonics are the same relative order of magnitude in all directions. However, a distinct multi-lobed acoustic pattern results due to the phase relationship between the passage of the blades of the front and aft propellers. In the horizontal plane, the even harmonics are of relatively constant magnitude in all direction. However, the odd harmonics are at a maximum near the disk plane and diminish to zero on the axis of rotation.

Suggestions by which to improve the noise model contained herein include:

a. investigation of the application of a second-order performance model to the prediction of the counterrotating propeller performance;

b. determine the effects of non-uniform inflow into the propeller disk-plane;

c. examine the effects of different front/aft RPM;

d. validate the far field acoustics using the present model by comparison with experimental data;

e. examine the inclusion of a broad-band noise model;

f. following the design method of Davidson for generating an optimum propeller for same front/aft rotation speeds, determine a design method for a propeller operating with different front/aft rotation speeds;

g. examine the effects of disk spacing on performance and noise;

h. compare the sensitivity of theoretical performance and acoustic predictions using the present model against experimental acoustic measurements for which the propeller performance is accurately known.

The preceding recommendations pertain to modification of the existing acoustic method. As noted however, the acoustics of a counterrotating propeller are extremely sensitive to the unsteady loads on the propeller blades. Consequently, it is also suggested that another performance method be investigated which calculates the compressible unsteady performance of a counterrotating configuration.

REFERENCES

1 Lindsay, R.B., *Acoustics*, Dowden, Hutchinson and Ross, Inc., Strandsburg, Penn., 1979, pp. 1–94.

2 Gutin, L., "On the Sound Field of a Rotating Propeller," NACA TM 1195, 1948. (From Phys. Zeitschr. der Sowjetunion, Band 9, Heft 1, 1936., pp. 57–71.)

3 Garrick, I.E., and Watkins, C.E., "A Theoretical Study of the Effect of Forward Speed on the Free-Space Sound-Pressure Field Around Propellers," NACA TM 3018, 1953.

4 Ffowcs Williams, J.E. and Hawkings, D.L., "Sound Generated by Turbulence and Surfaces in Arbitrary Motion," *Philosophical Transactions of the Royal Society of London*, Vol. A264, 1969.

5 Lighthill, M.J., *Fourier Analysis and Generalized Functions* , Cambridge University Press, Cambridge, England, 1958.

6 Farassat, F. and Brown, T.J., "A New Capability for Predicting Helicopter Rotor and Propeller Noise Including the Effect of Forward Motion," NASA TM X-74037, 1977.

7 Hawkings, D.L., and Lowson, M.V., "Theory of Open Supersonic Rotor Noise," *J. of Sound and Vibration*, Vol. 36, 1974, pp. 1–20.

8 Hanson, D.B., "Near Field Noise of High Tip Speed Propellers in Forward Flight," AIAA Paper 76-565, 1976.

9 Woan, C.J. and Gregorek, G.M. "The Exact Numerical Calculation of Propeller Noise," AIAA Paper 78-1122, 1978.

10 Jou, W.H, "Procedure for Noise Prediction and Optimization of Advanced Technology Propellers," NASA CR 3080, 1979.

11 Succi, G.P., "Design of Quiet Efficient Propellers," SAE Paper 790548, 1979.

12 White, T.A., "Numerical Evaluation of Propeller Noise, Including Non-Linear Effects," Master of Science Thesis, Aerospace Engineering Department, Texas A&M University, August 1985.

13 Korkan, K.D., von Lavante, E., and Bober, L.J., "Numerical Evaluation of Propeller Noise Including Nonlinear Effects," *AIAA J.*, Vol. 24, No. 6, 1986, pp. 1043–1045.

14 Denner, B.W., "Application of DENTON Euler-solver to Predict Near Field Acoustics of Propellers," Research Division, Dowty Rotol, Ltd., Gloucester, England, August 1987.

15 Forsyth,D.W., "Computational Aeroacoustics of Near Field Propfan Noise Using 3-D Euler Analysis," Master of Science Thesis, Aerospace Engineering Department, Texas A&M University, December 1987.

16 Jaeger, S.M., "On the Prediction of Farfield Computational Aeroacoustics of Advanced Propellers," Master of Science Thesis, Aerospace Engineering Department, Texas A&M University, To be published in December 1989.

17 Korkan, K.D., Jaeger, S.M., and Kim, J.H., "Determination of Near and Far Field Acoustics for Advanced Propeller Configurations," AIAA Paper 89-1040, 1989.

18 Farassat, F. and Myers, M.K., "Extension of Kirchoff's Formula to Radiation from Moving Surfaces," NASA TM 87149, 1987.

19 Hawkings, D.L., "Noise Generation by Transonic Open Rotors," Research Paper No. 599, Westland Helicopters, Limited, Yeovil, Somerset, England, June 1979.

20 Kim, J., "Application of the Computational Aeroacoustics Method to an Advanced Counterrotating Propfan Configuration," Master of Science Thesis, Aerospace Engineering Department, Texas A&M University, May 1989.

21 Whitfield, D.L., Swafford, T.W., Janus, J.M., Mulac, R.A., and Belk, D.M., "Three-Dimensional Unsteady Euler Solutions for Propfans and Counter--Rotating Propfans in Transonic Flow," AIAA Paper 87-1197, June 1987.

22 Davidson, R.E., "Optimization and Performance Calculation of Dual-Rotation Propellers," NASA TP 1948, December 1981.

23 Denner, B.W. and Korkan, K.D., "Performance and Acoustic Prediction of Counterrotating Propeller Configurations," SAE Paper No. 891035, 1989.

24 Watanabe, T. and Kawachi, K., "Noise Prediction of Counterrotation Propeller," AIAA Paper 87-2658, October 1987.

25 Lesieutre, D.J., "The Theoretical Performance of Counter-Rotating Propeller Systems," Master of Science Thesis, Department of Aeronautics and Astronautics, Purdue University, May 1985.

26 Korkan, K.D., and Playle, S.C., "On the Design of Counterrotating Propellers," SAE Paper 830773, 1983.

27 Playle, S.C., Korkan, K.D., and von Lavante, E., "A Numerical Method for the Design and Analysis of Counter-Rotating Propellers," *AIAA J. of Propulsion and Power*, Vol. 2, No. 1, 1986, pp. 57–63.

28 Lock, C.N.H., and Yeatman, D., "Tables for Use in an Improved Method of Airscrew Strip Theory Calculation," R. & M. No. 1674, British A.R.C., 1935.

29 Crigler, J.L., "Application of Theodorsen's Theory to Propeller Design," NACA Rep. 924, 1949 (Supersedes NACA RM L8F30).

30 Sullivan, J.P., "The Effect of Blade Sweep on Propeller Performance," AIAA Paper 77-716, 1977.

31 Sears, W.R., "A Systematic Presentation of the Theory of Thin Airfoils in Non-Uniform Motion," Ph.D Thesis, California Institute of Technology, 1938.

32 Drischler, J.A., "Calculation and Compilation of the Unsteady-Lift Functions for a Rigid Wing Subjected to sinusoidal Gusts and to Sinusoidal Sinking Oscillations," NACA TN 3748, October 1986.

33 Mazelsky, B., and Drischler, J.A., "Numerical Determination of Indicial Lift and Moment Functions for a Two-Dimensional Sinking and Pitching Airfoil at Mach Numbers 0.5 and 0.6," NACA TN 2739, 1952.

34 Mazelsky, B., "Numerical Determination of Indicial Lift of a Two-Dimensional Sinking Airfoil at Subsonic Mach Numbers From Oscillatory Lift Coefficients With Calculations for Mach Number 0.7," NACA TN 2562, 1951.

35 Bumann, E.A., "An Acoustic Experimental Investigation of Single Rotation Propellers," Master of Science Thesis, Aerospace Engineering Department, Texas A&M University, December 1988.

36 Denner, B.W., "User's Guide/Program Listing for Acoustic Prediction of Counterrotating Propeller Configurations," Aerospace Engineering Department, Texas A&M University, July 1989.

37 Gazzaniga, J.A., "Acoustic Experimental Investigation of Counterrotating Propeller Configurations," Master of Science Thesis, Texas A&M University, To be published in December 1989.

38 McCormick, B.W., Eisenhuth, J.J., and Lynn, J.E., "A Study of Torpedo Propellers – Part I," The Pennsylvania State University, Ordnance Research Laboratory, report NOrd 16597-5, 1956.

39 McKay, B., Private Communication, Dec. 1988.

APPENDIX A

FIGURES

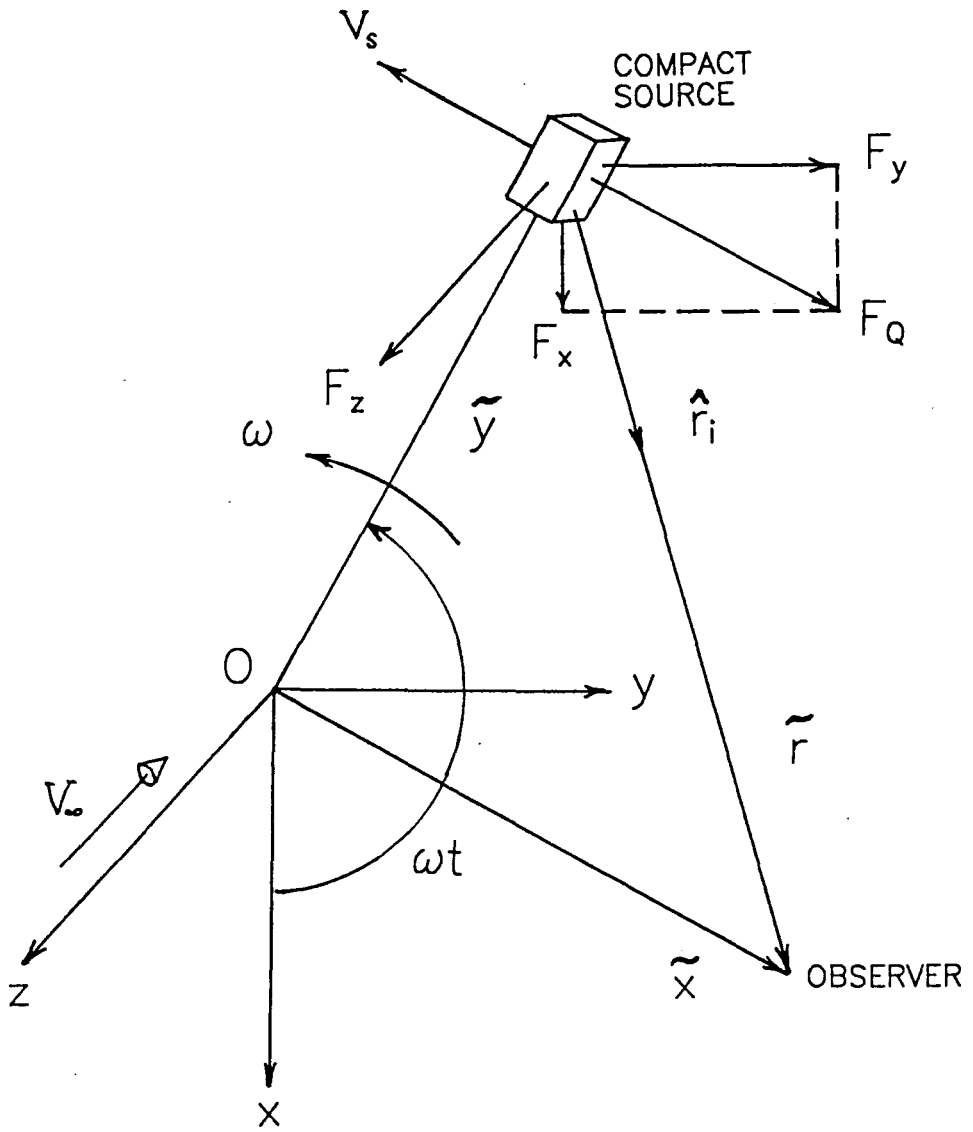

Figure 1. Geometry of One Rotating Compact Acoustic Source.

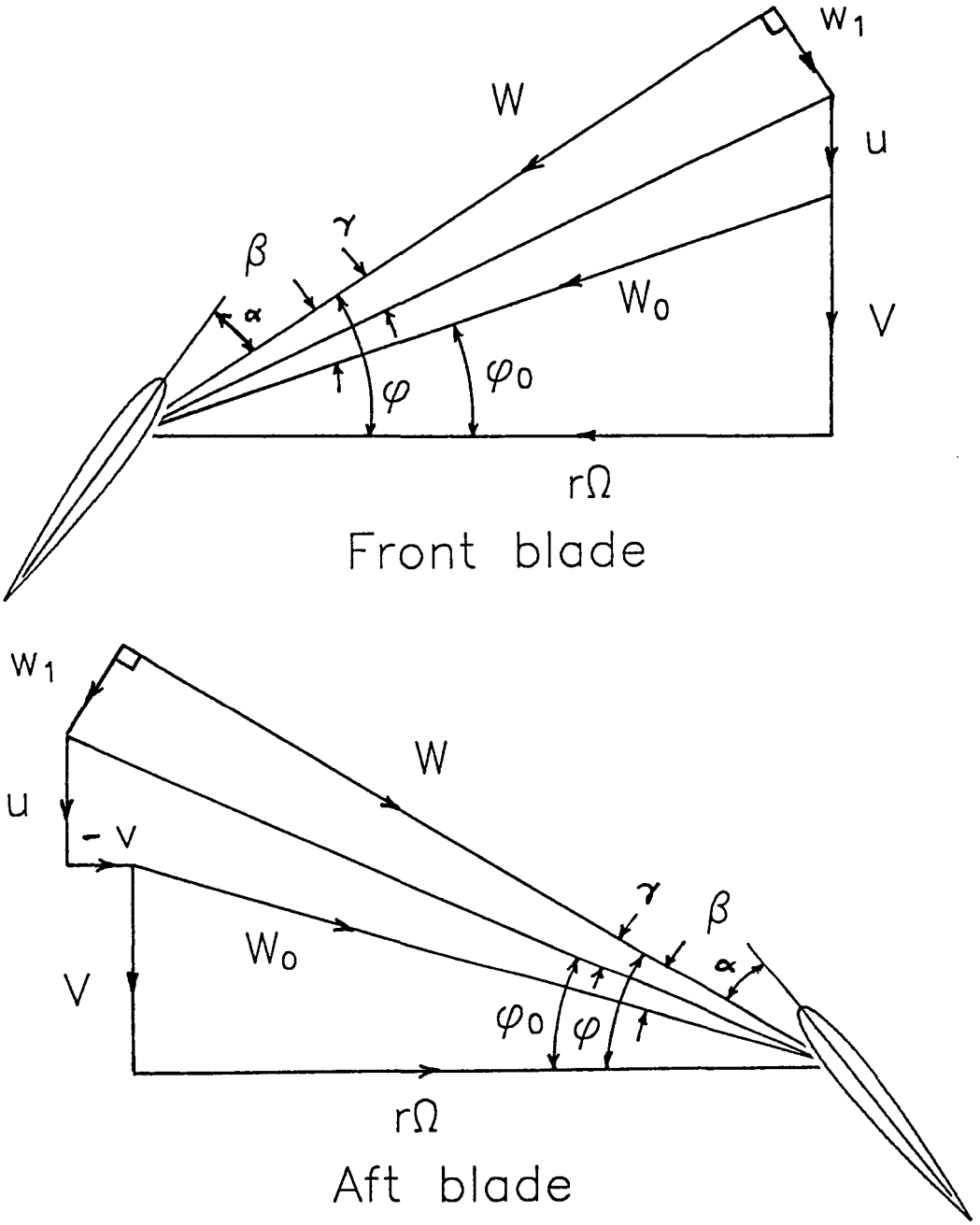

Figure 2. Velocities at Front and Back Counterrotating Propeller Blades.

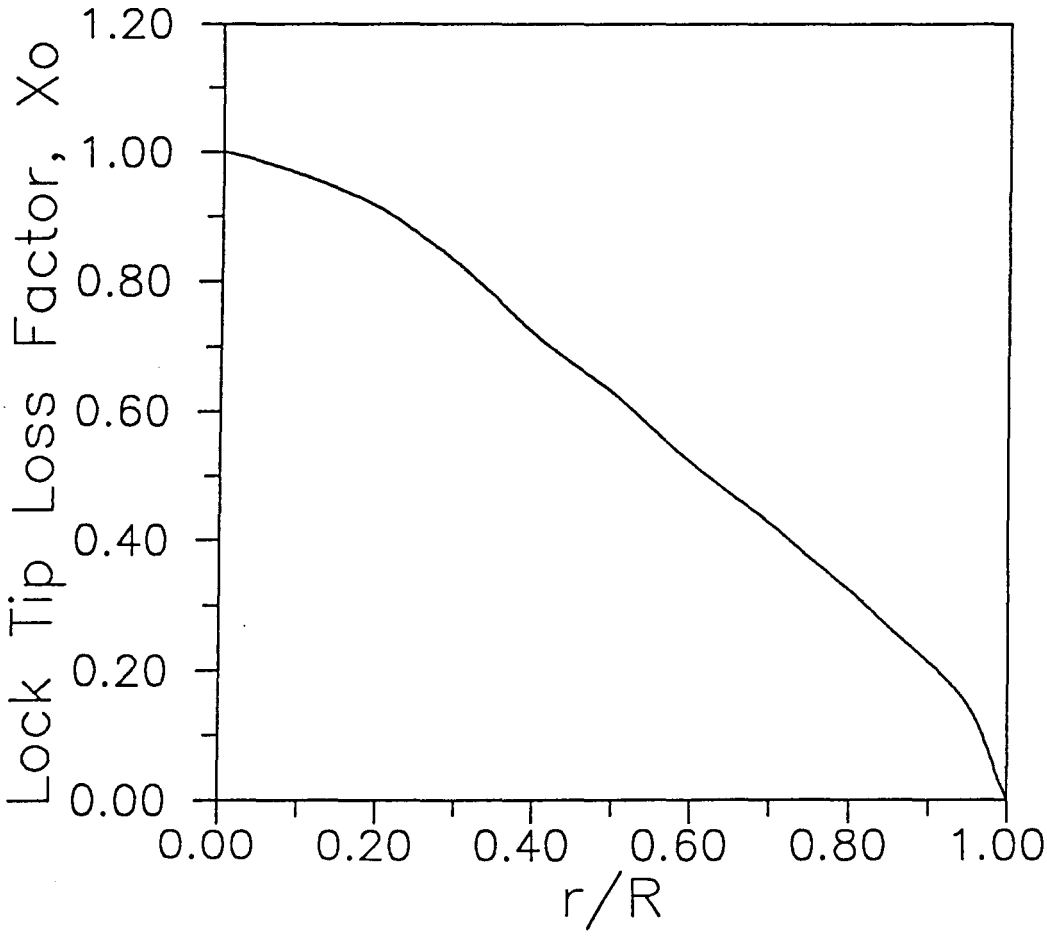

Figure 3. Example of Radial Variation of the Lock Tip Loss Factor, X_0.

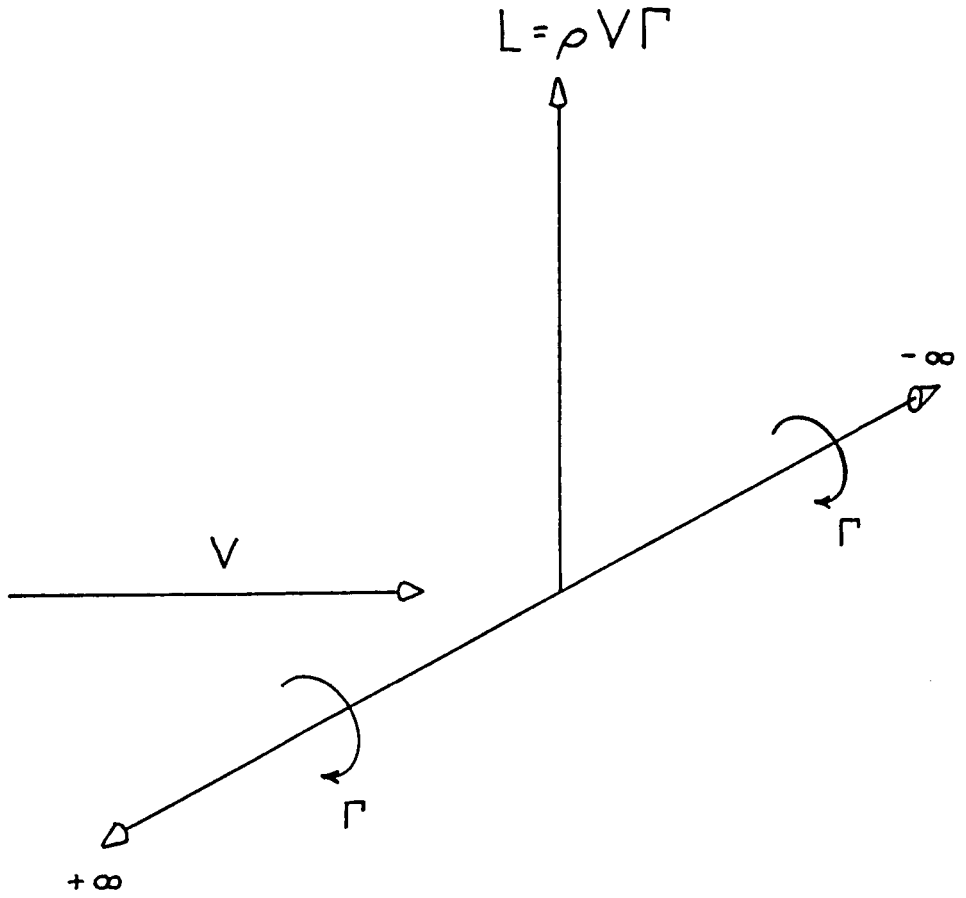

Figure 4. Vortex Filament in Uniform Flow.

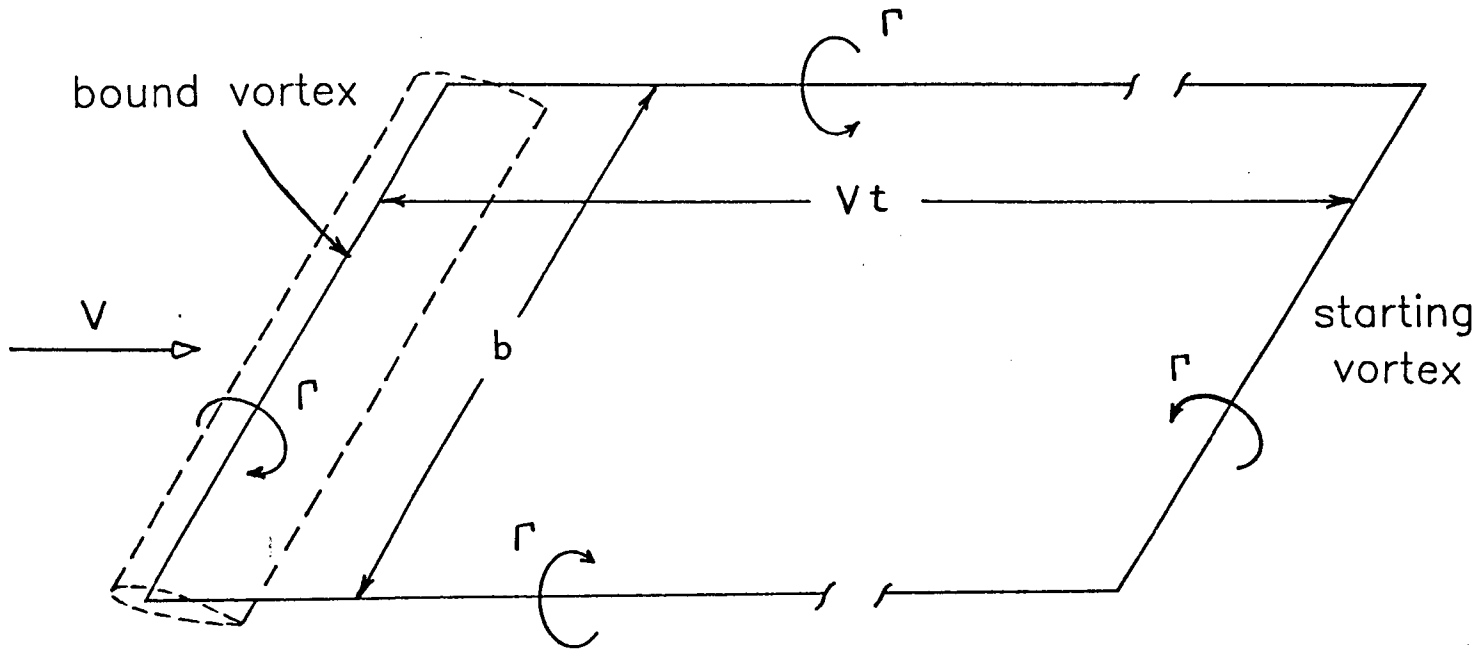

Figure 5. Bound Vortex on Wing with Constant Spanwise Lift Distribution.

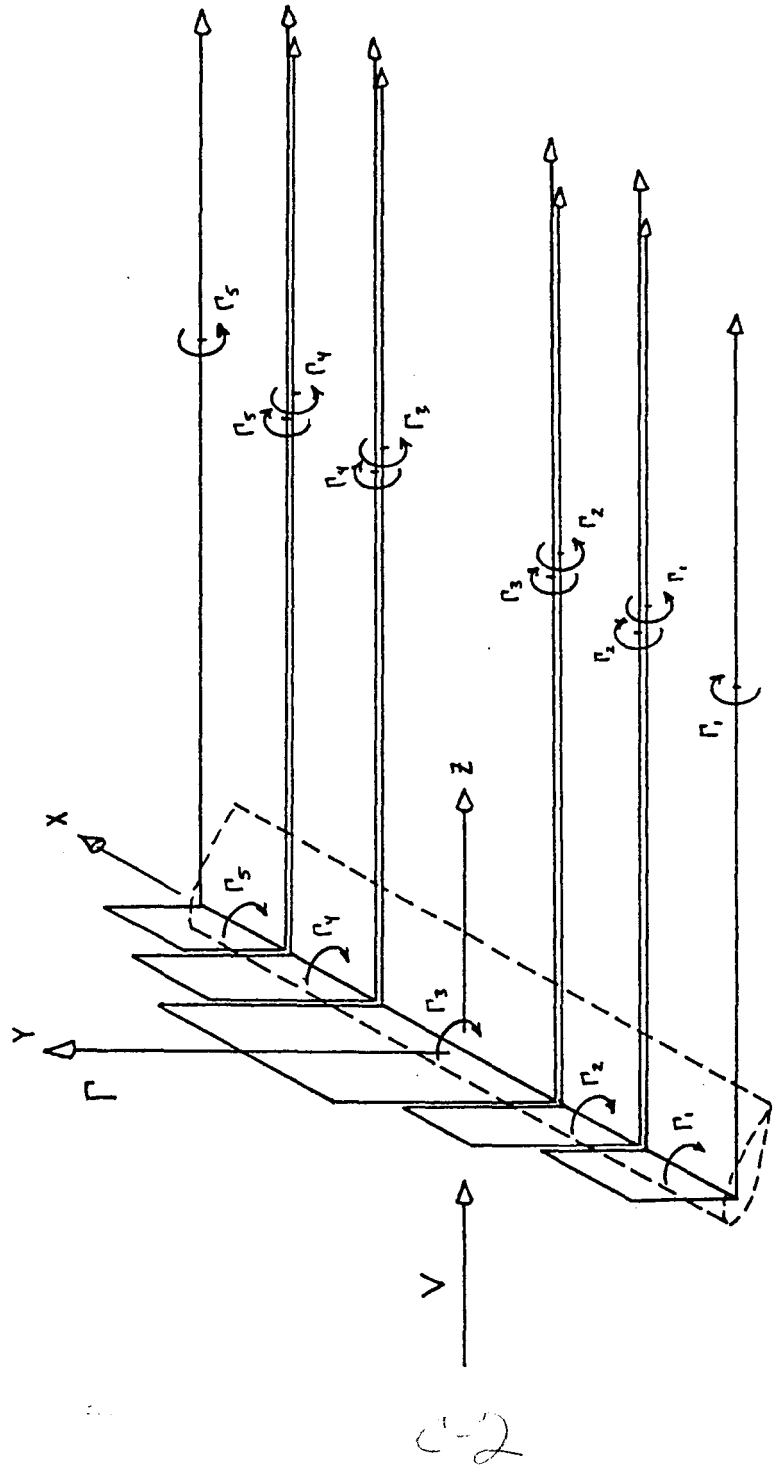

Figure 6. Horseshoe Vortices on Wing with Variable Lift Distribution.

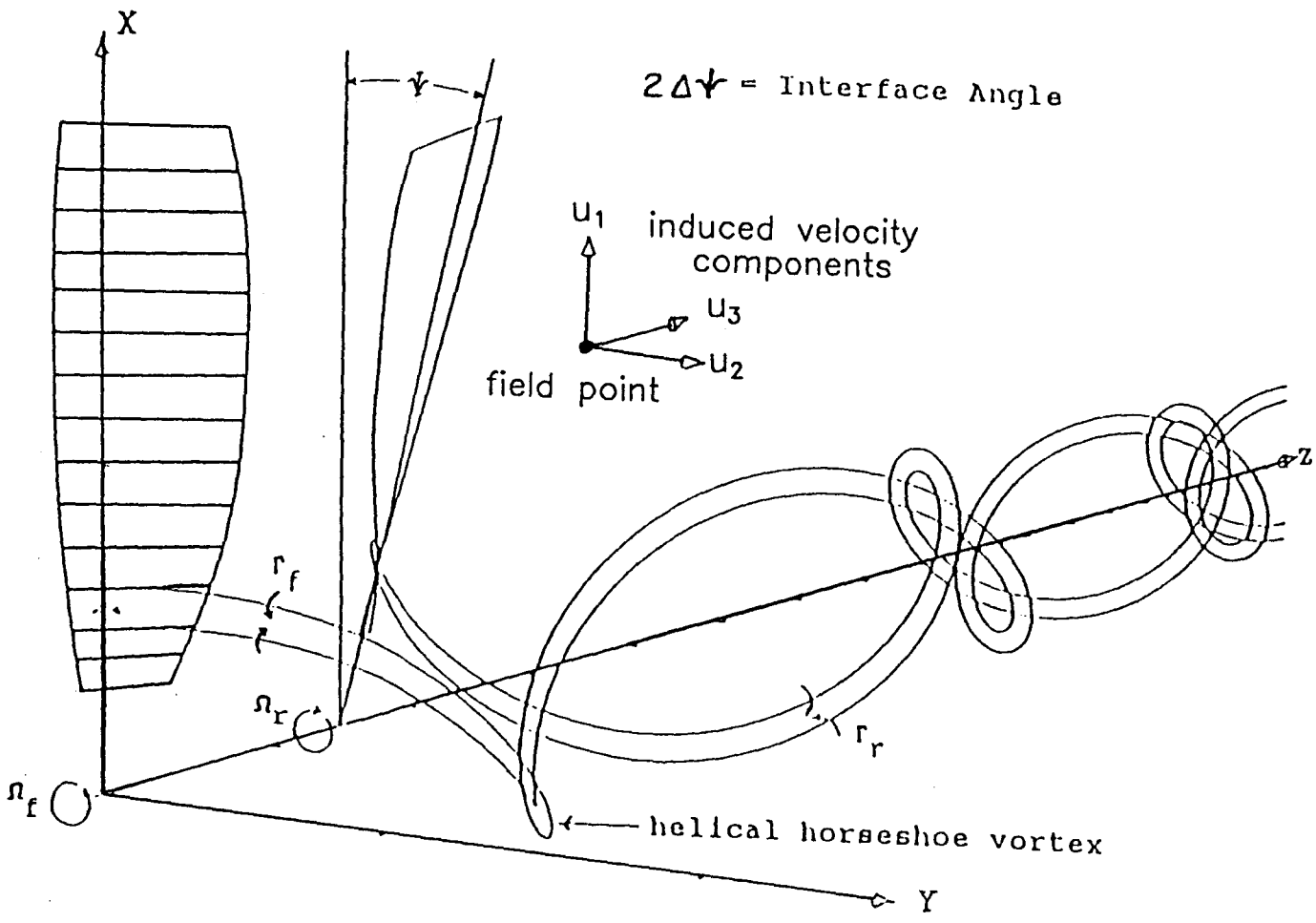

Figure 7. Helical Horseshoe Vortices on Counterrotating Propeller.

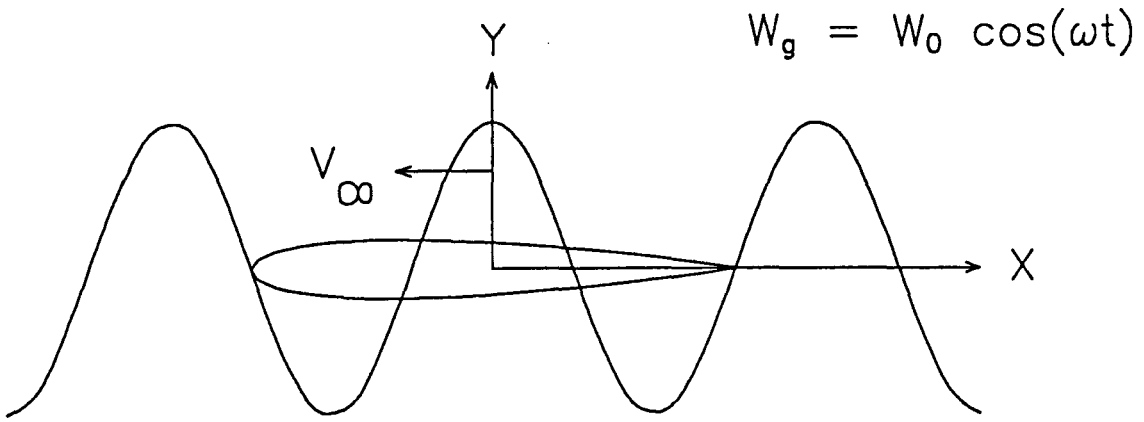

Figure 8. Airfoil in Sinusoidal Vertical Gust.

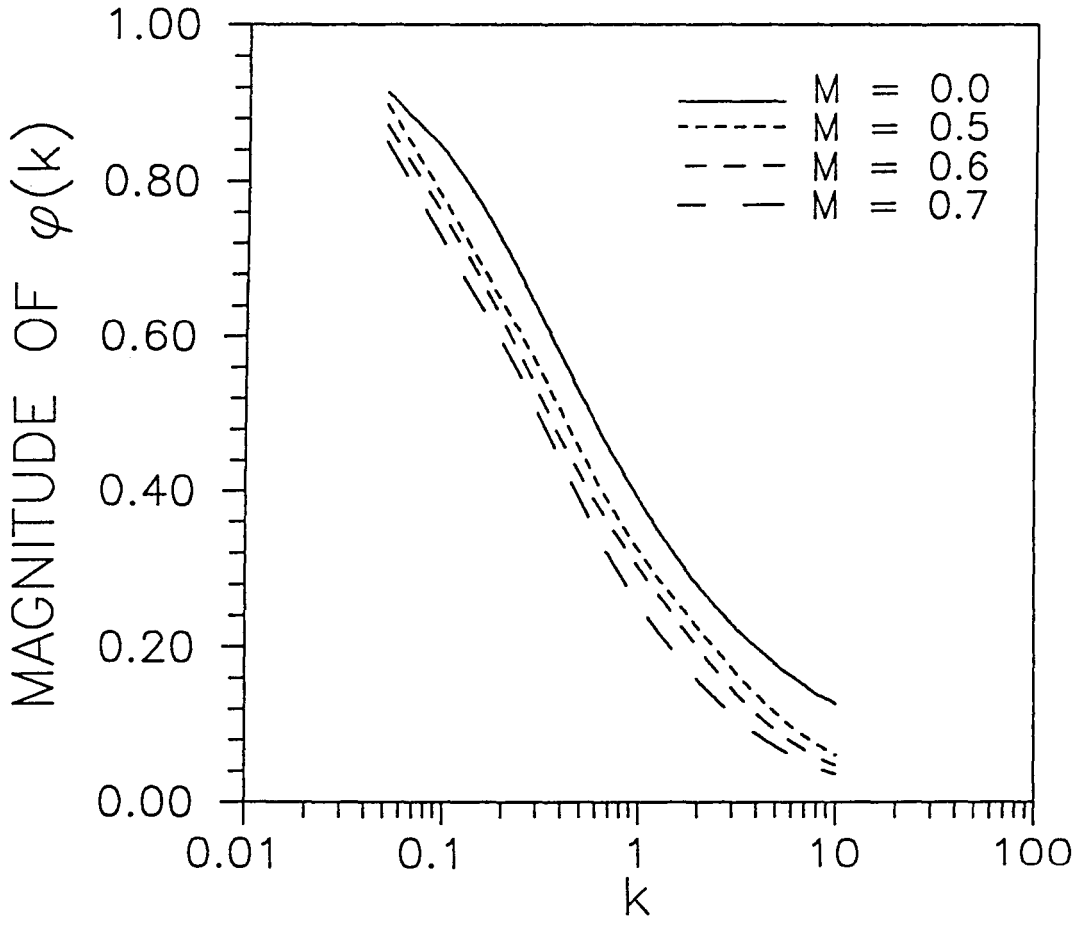

Figure 9. Magnitude of Sears Function, $\varphi(k)$.

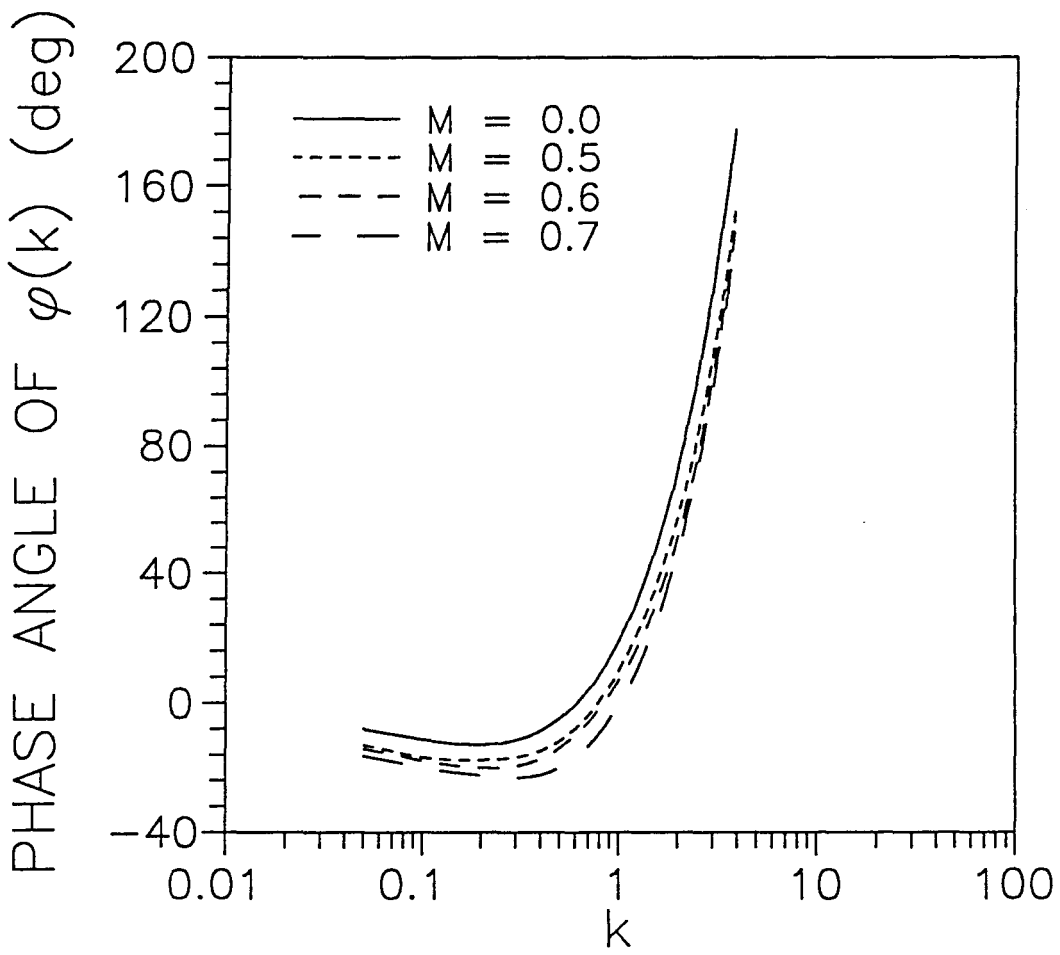

Figure 10. Phase Angle of Sears Function, $\varphi(k)$.

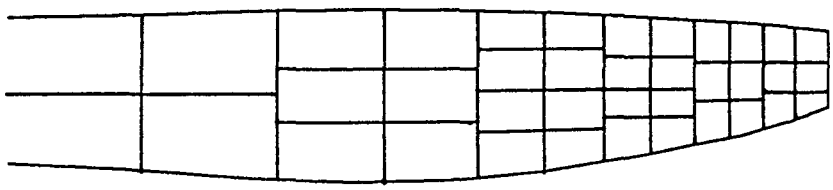

Figure 11. Division of Propeller Blade into Compact Acoustic Sources.

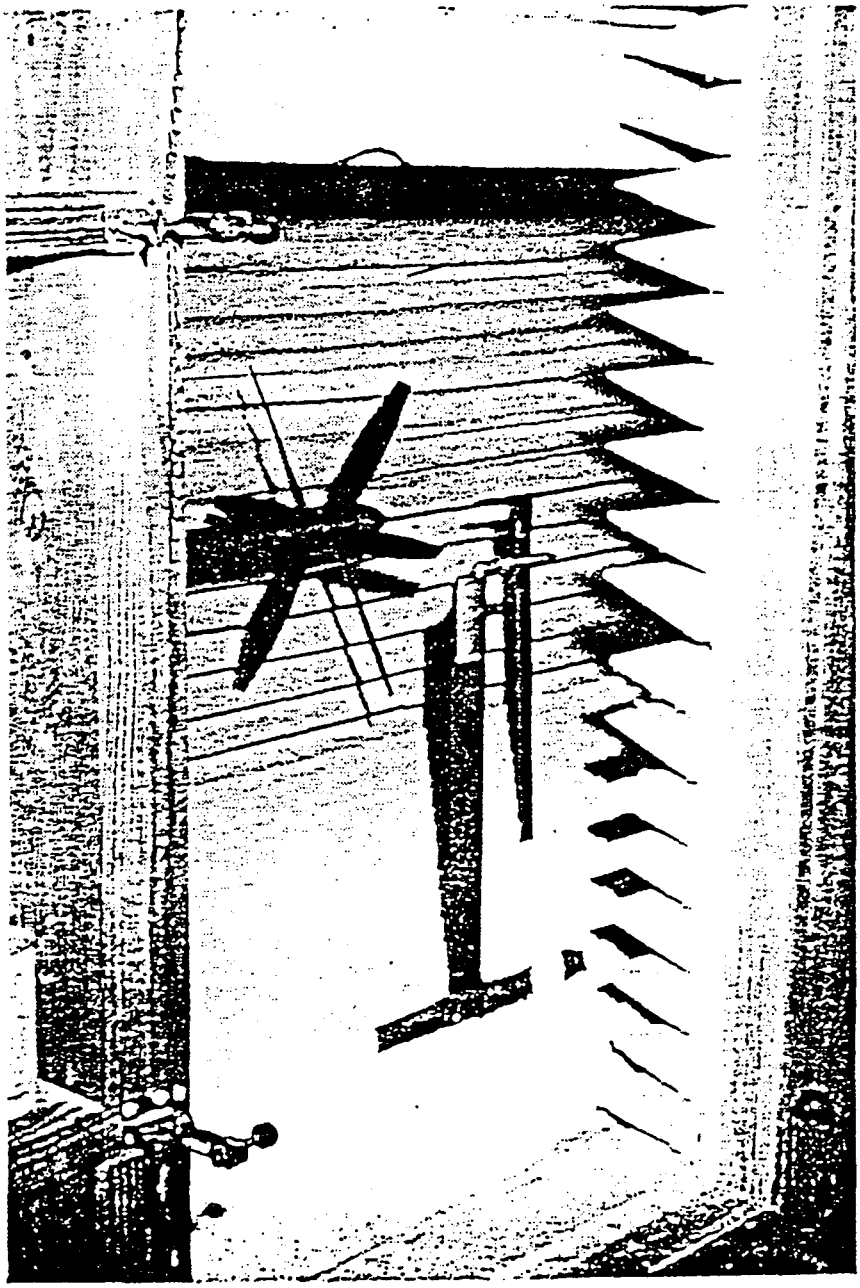

Figure 12. Experimental Counterrotating Propeller in Wind Tunnel, Showing Acoustic Wedges and Microphone Locations.

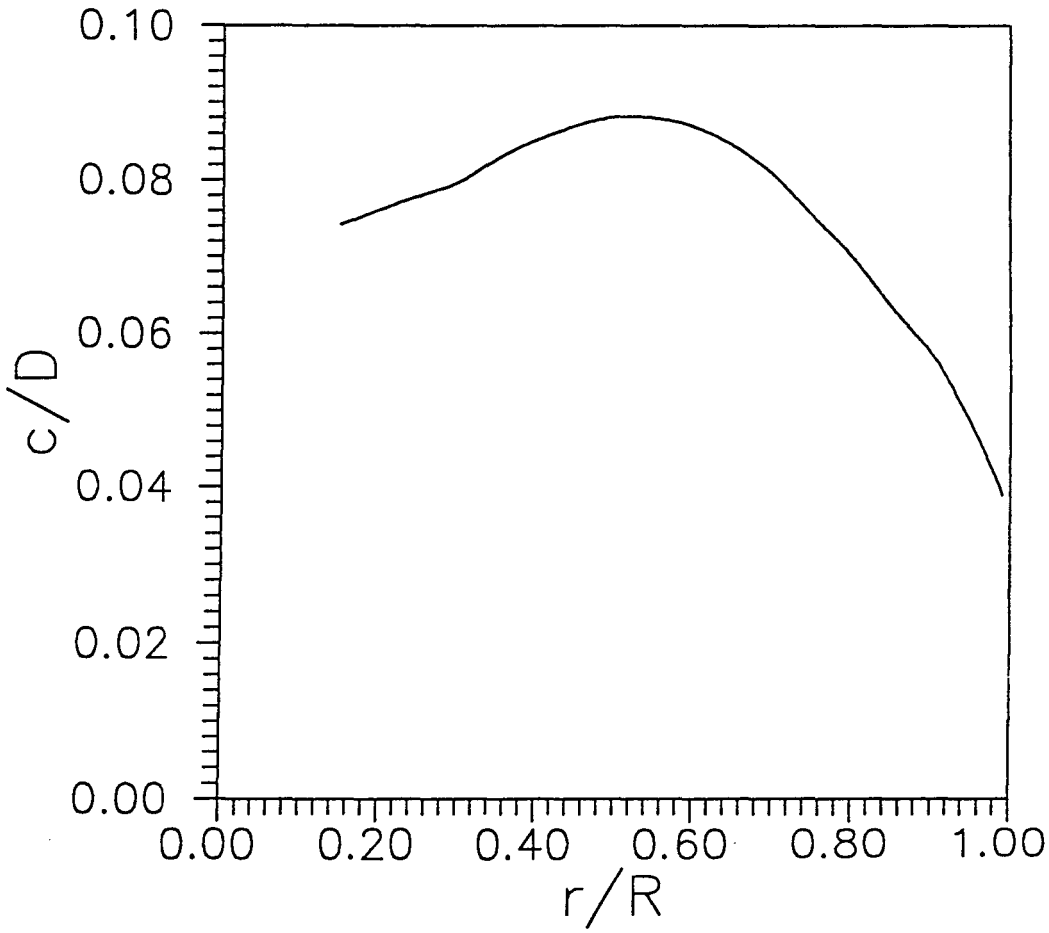

Figure 13. Radial Chord-to-Diameter Ratio Distribution of Experimental Propeller Blades.

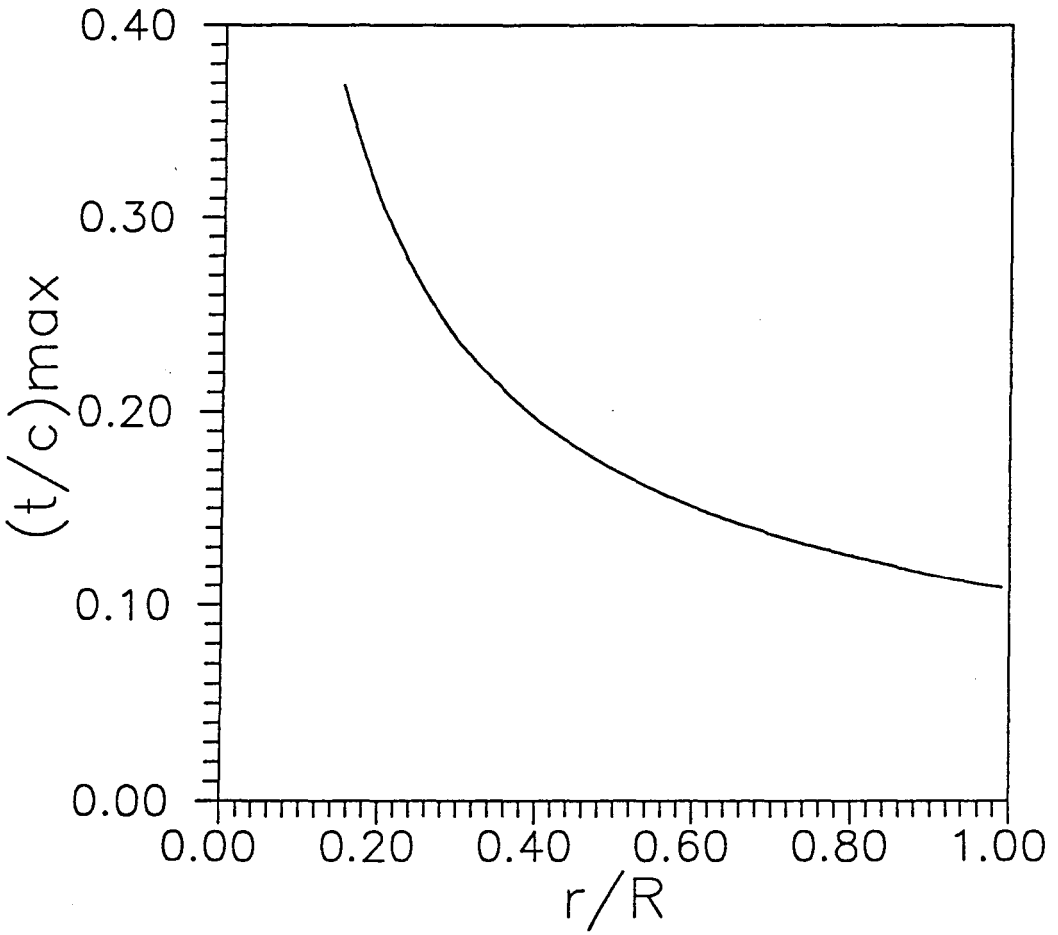

Figure 14. Radial Maximum Thickness-to-Chord Ratio Distribution of Experimental Propeller Blades.

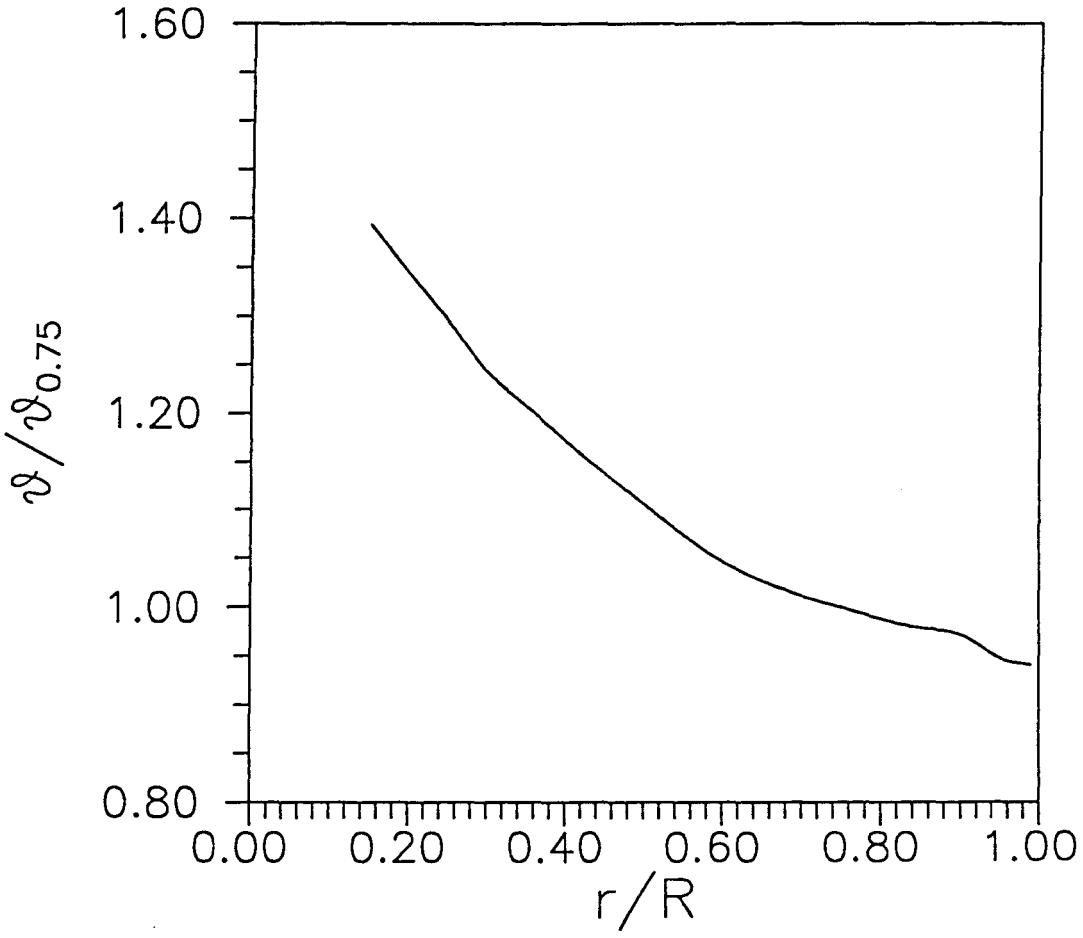

Figure 15. Radial Blade Twist Distribution of Experimental Propeller Blades Nondimensionalized by the Blade Twist at the 75 % Location.

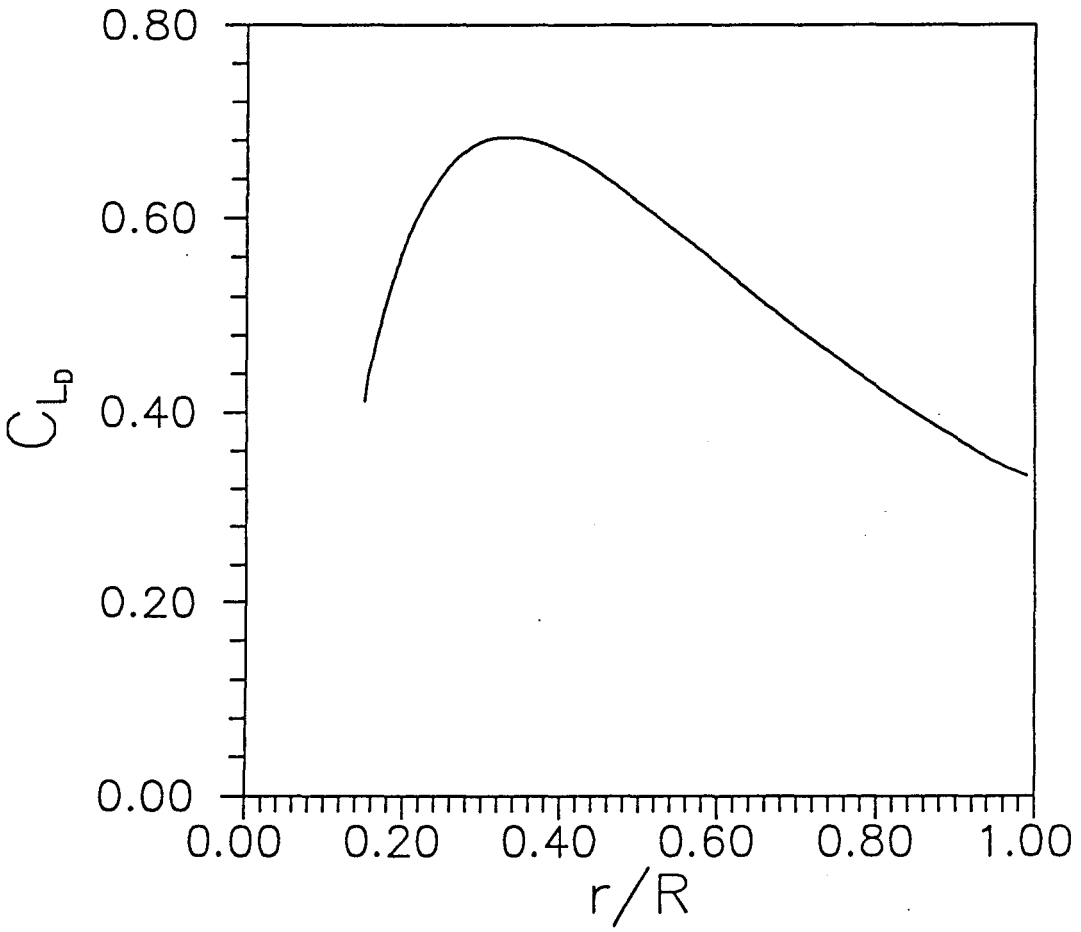

Figure 16. Radial Design Lift Coefficient Distribution of Experimental Propeller Blades.

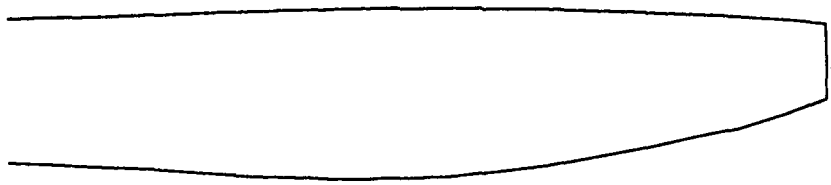

Figure 17. Developed Planform of Experimental Propeller Blade.

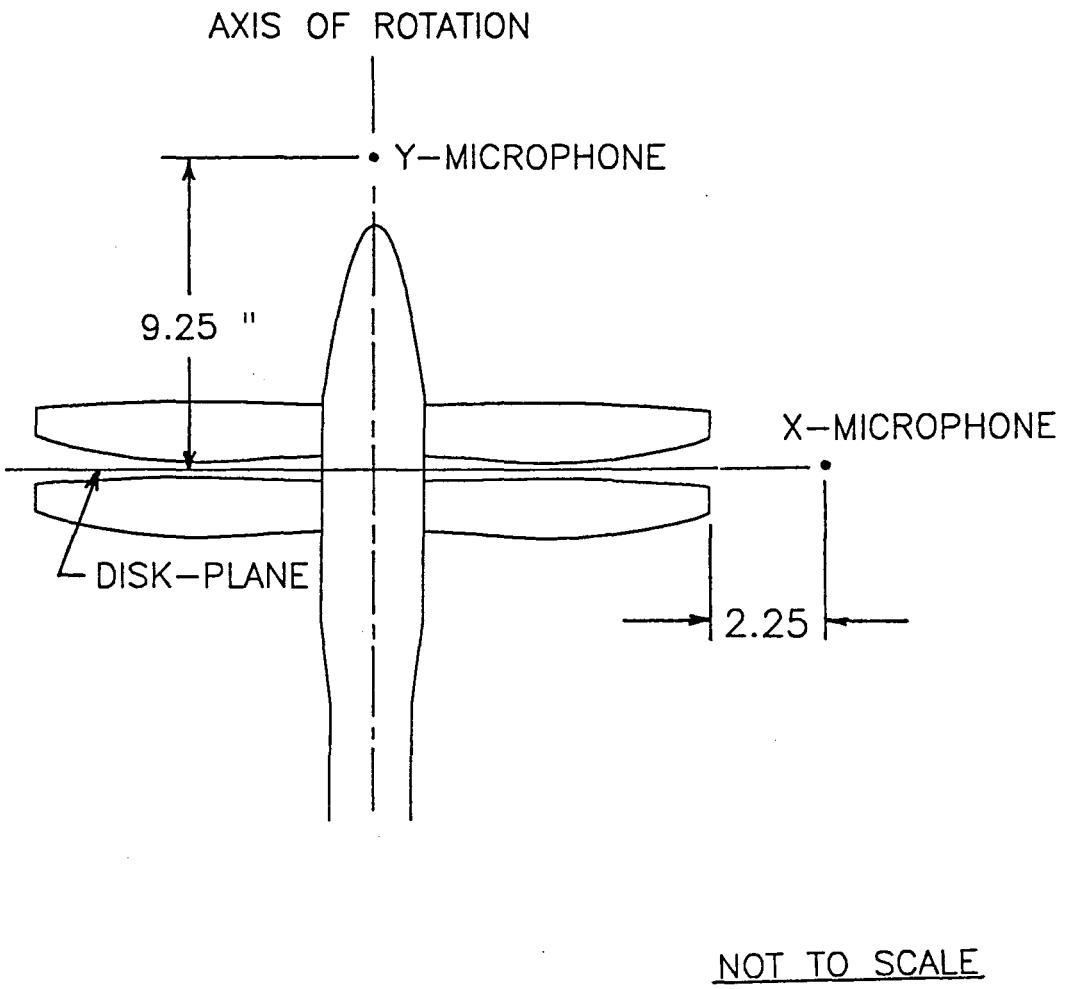

Figure 18. Location of Microphone in Experimental Measurements of Gazzaniga.

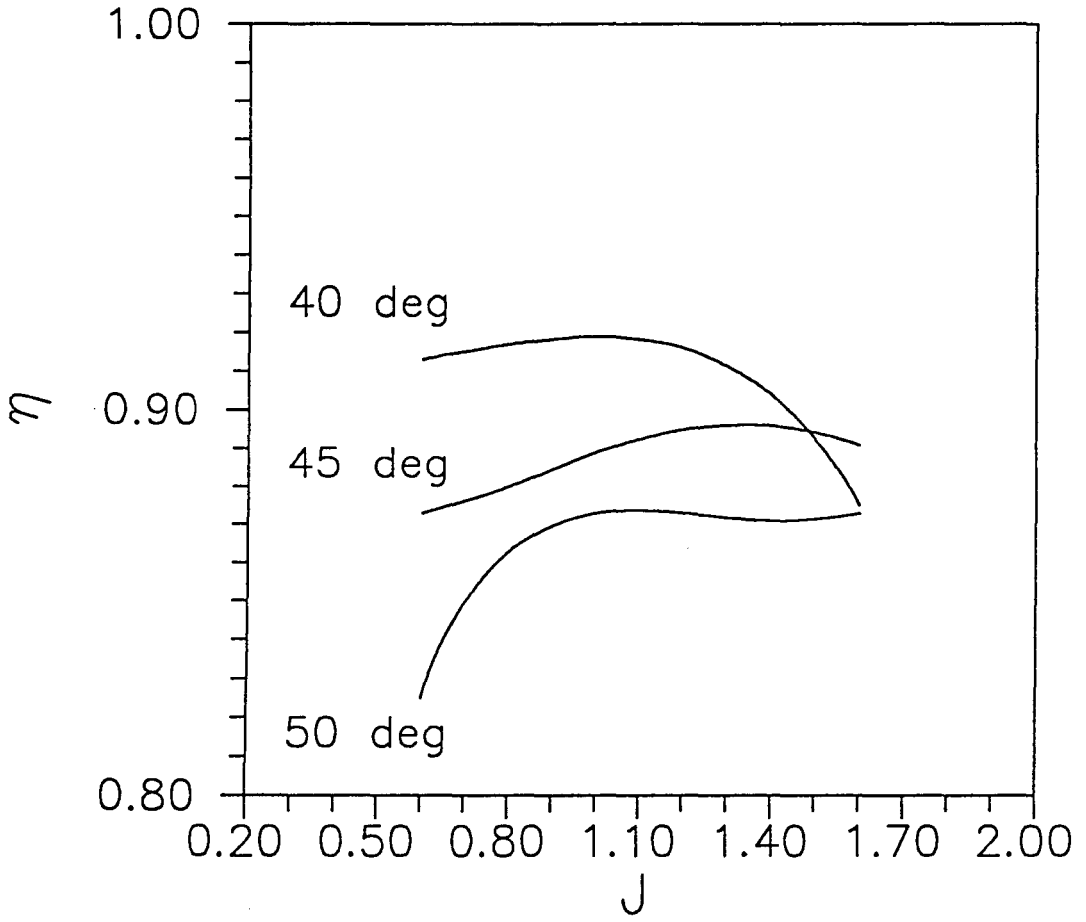

Figure 19. Total 3 × 3 Blade Experimental Propeller Efficiency Variation with Advance Ratio at 40°, 45°, and 50° Blade Tip Angle.

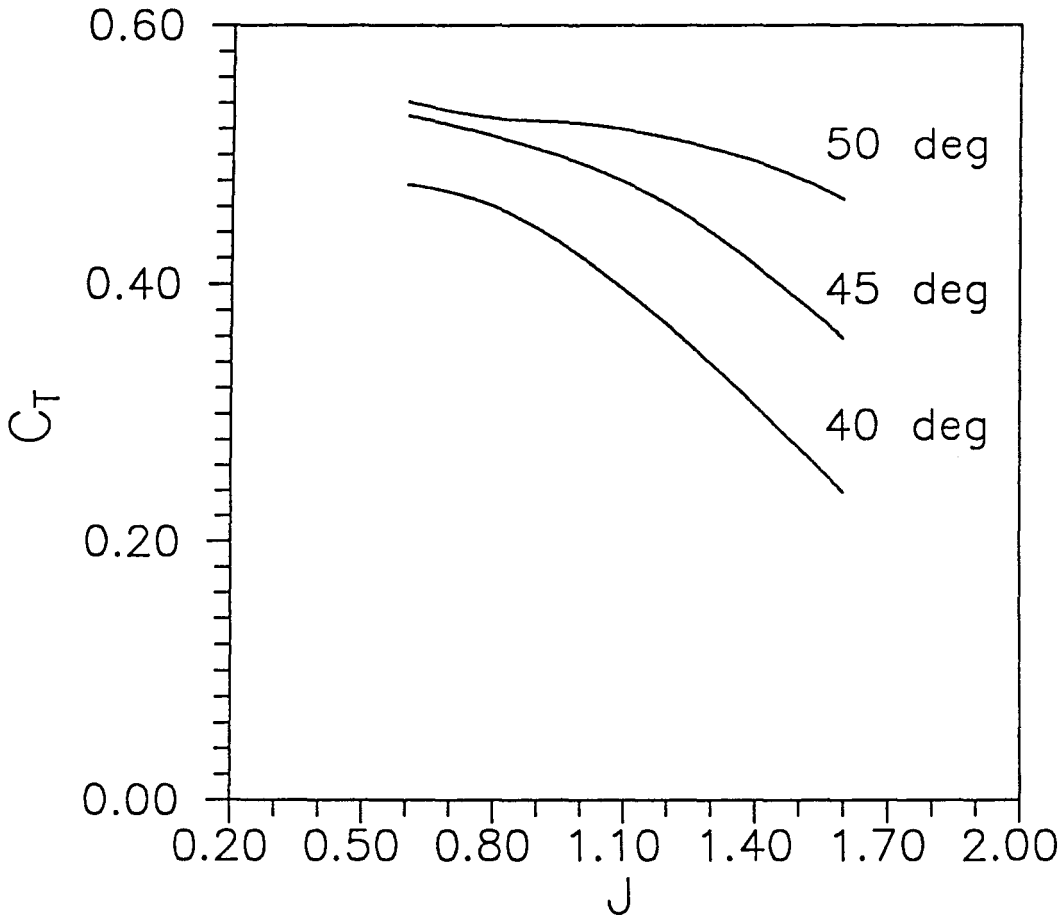

Figure 20. Total 3 × 3 Blade Experimental Propeller Thrust Coefficient Variation with Advance Ratio at 40°, 45°, and 50° Blade Tip Angle.

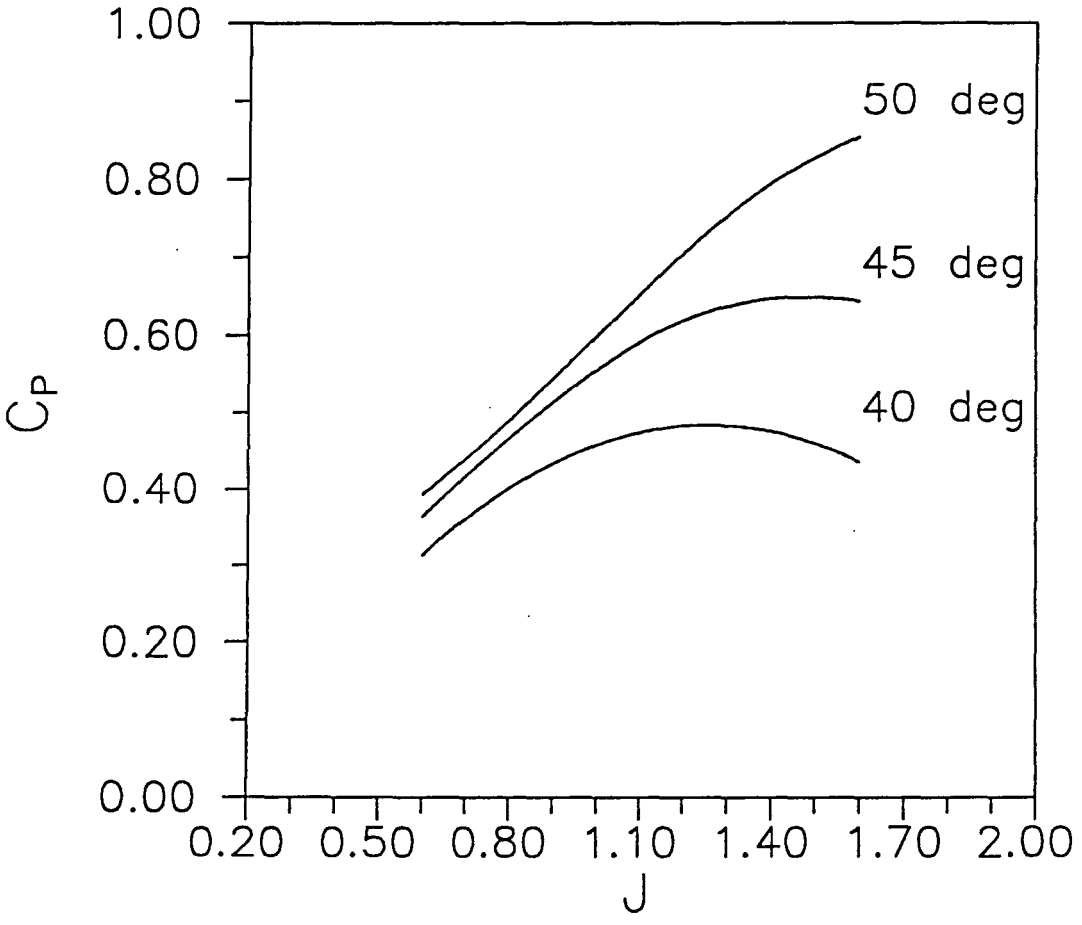

Figure 21. Total 3 × 3 Blade Experimental Propeller Power Coefficient Variation with Advance Ratio at 40°, 45°, and 50° Blade Tip Angle.

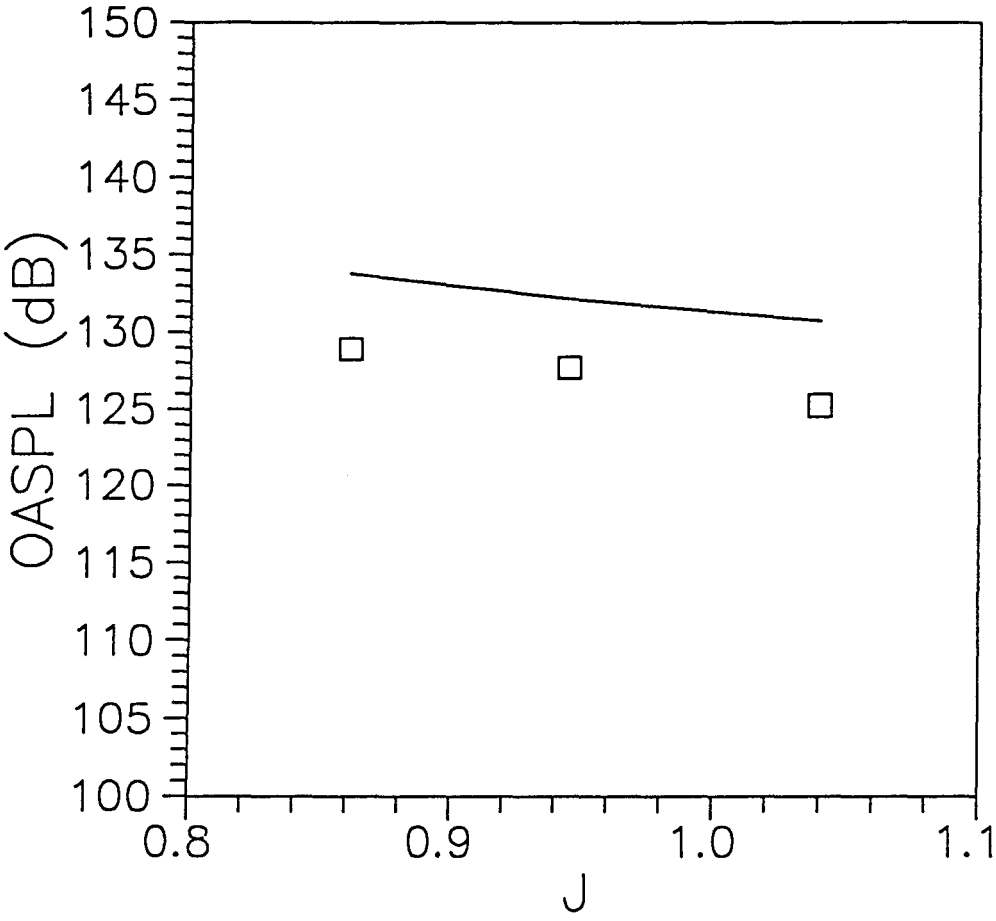

Figure 22. Theoretical and Experimental Noise Level Variation with Advance Ratio; 3×3 Blades; 40° Blade Tip Angle; X-microphone; $P_{ref} = 20\ \mu$ Pa.

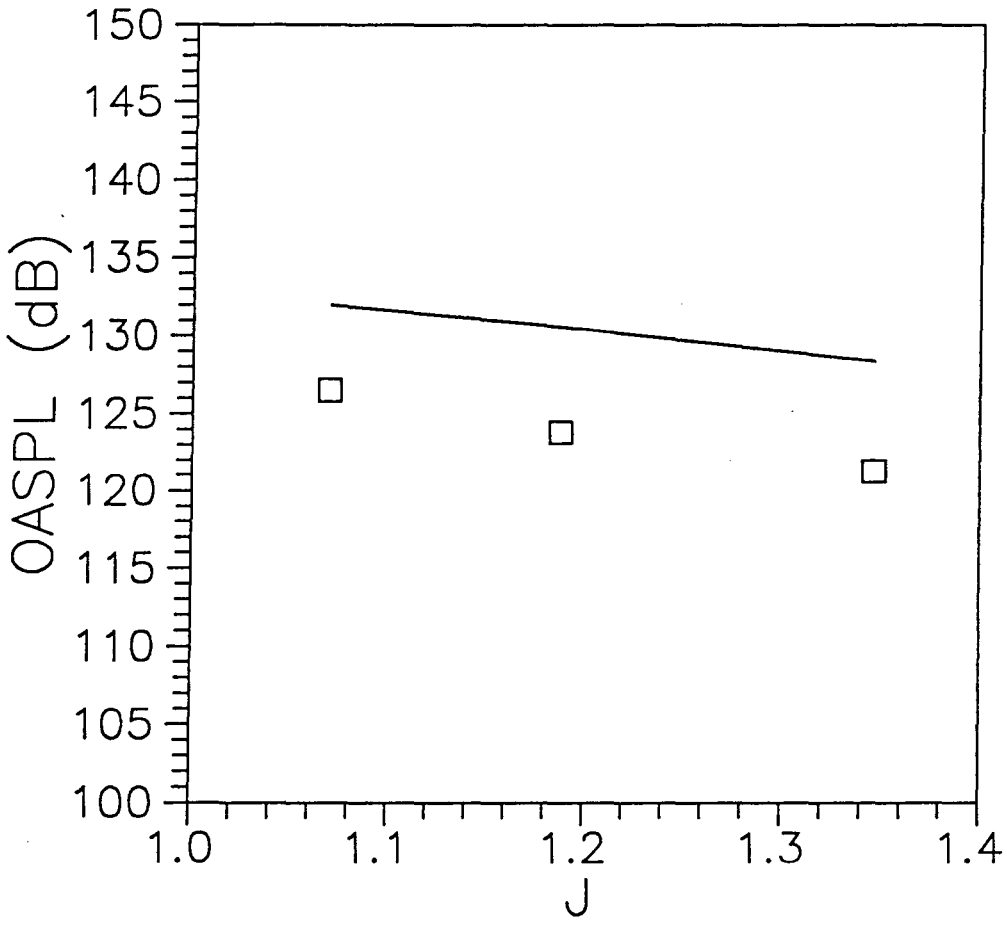

Figure 23. Theoretical and Experimental Noise Level Variation with Advance Ratio; 3×3 Blades; 45° Blade Tip Angle; X-microphone; $P_{ref} = 20\ \mu$ Pa.

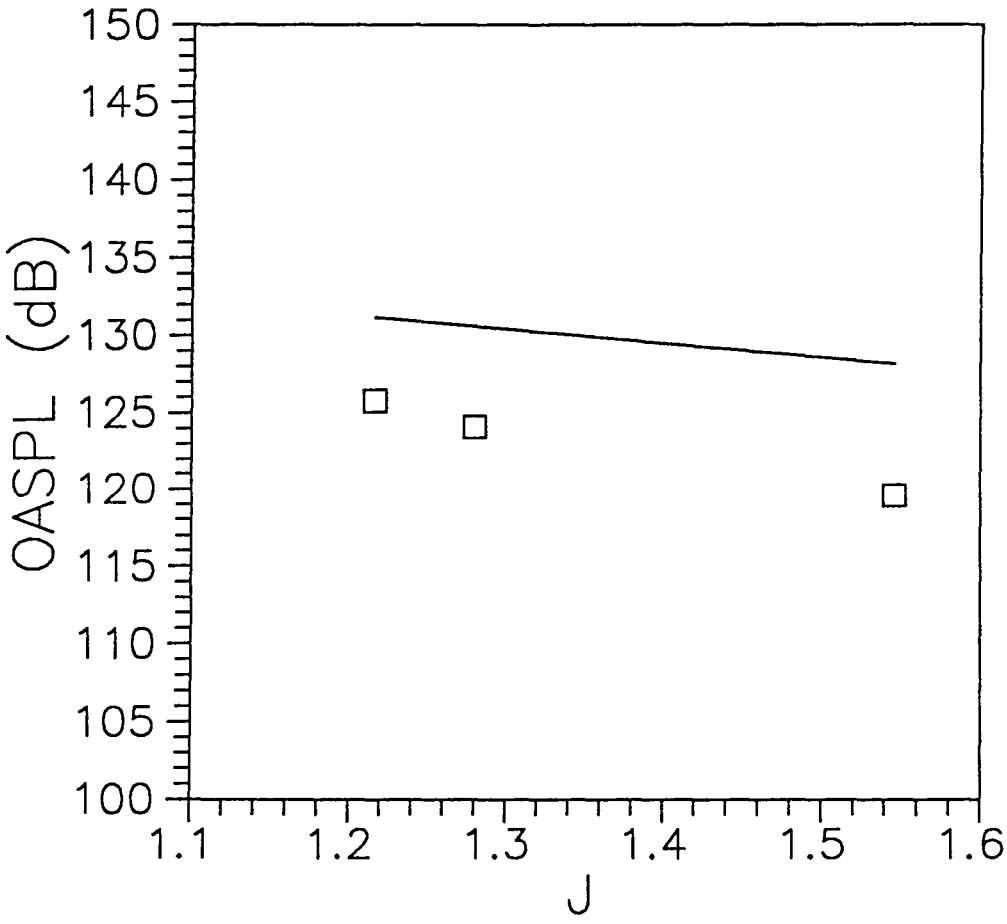

Figure 24. Theoretical and Experimental Noise Level Variation with Advance Ratio; 3×3 Blades; 50° Blade Tip Angle; X-microphone; $P_{ref} = 20\ \mu$ Pa.

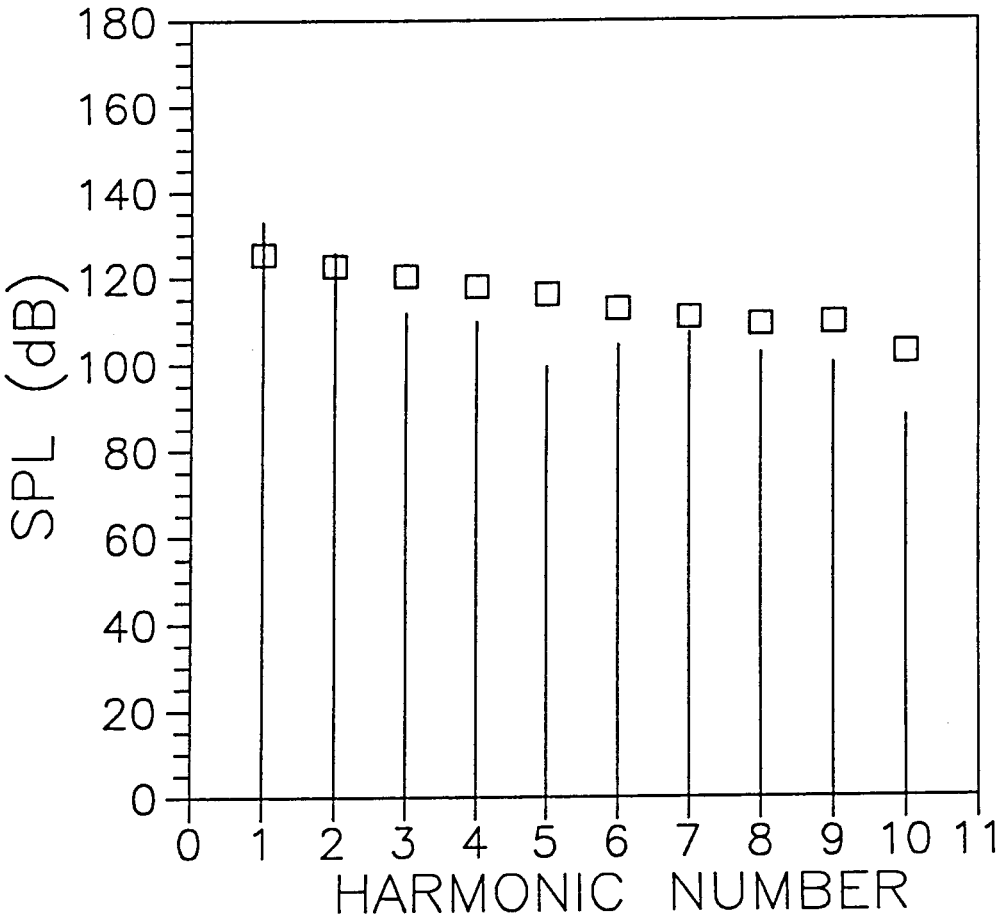

Figure 25. Theoretical and Experimental Frequency Spectra of 3×3 Blade Propeller; J=0.861; 40° Blade Tip Angle; X-microphone; P_{ref} = 20 μ Pa.

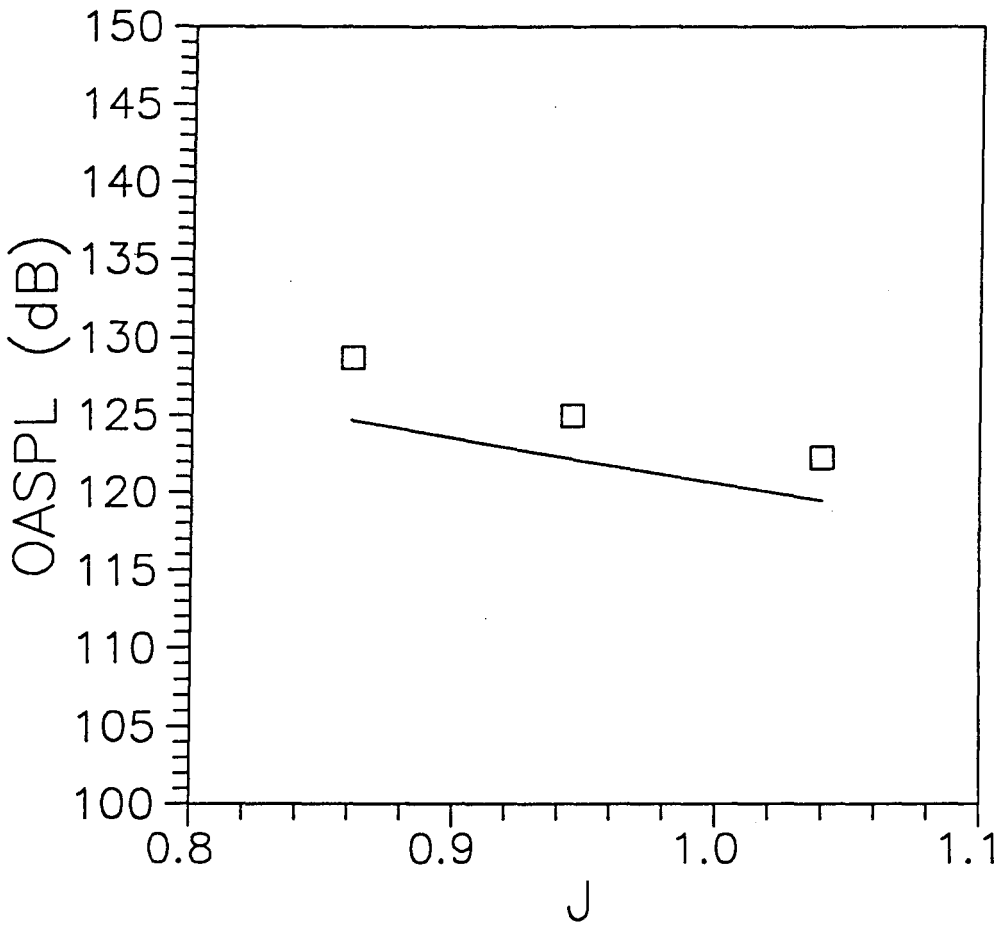

Figure 26. Theoretical and Experimental Noise Level Variation with Advance Ratio; 3×3 Blades; 40° Blade Tip Angle; Y-microphone; $P_{ref} = 20\ \mu$ Pa.

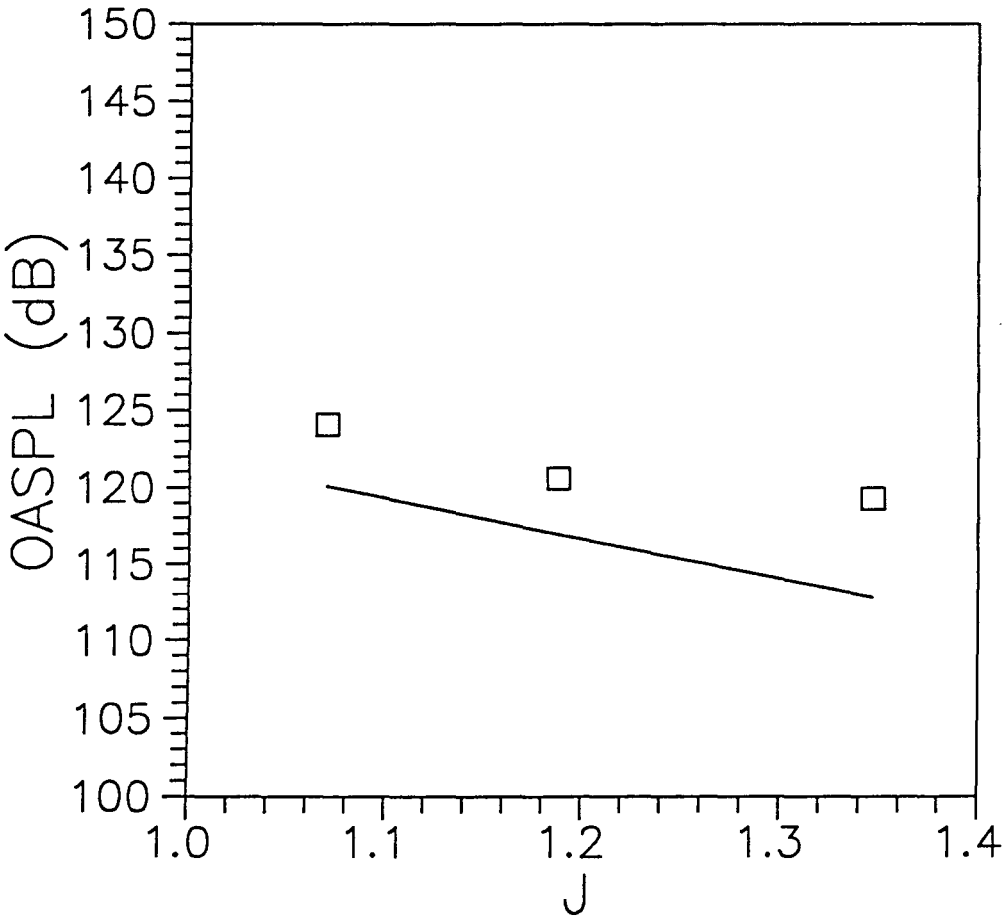

Figure 27. Theoretical and Experimental Noise Level Variation with Advance Ratio; 3×3 Blades; 45° Blade Tip Angle; Y-microphone; $P_{ref} = 20\ \mu$ Pa.

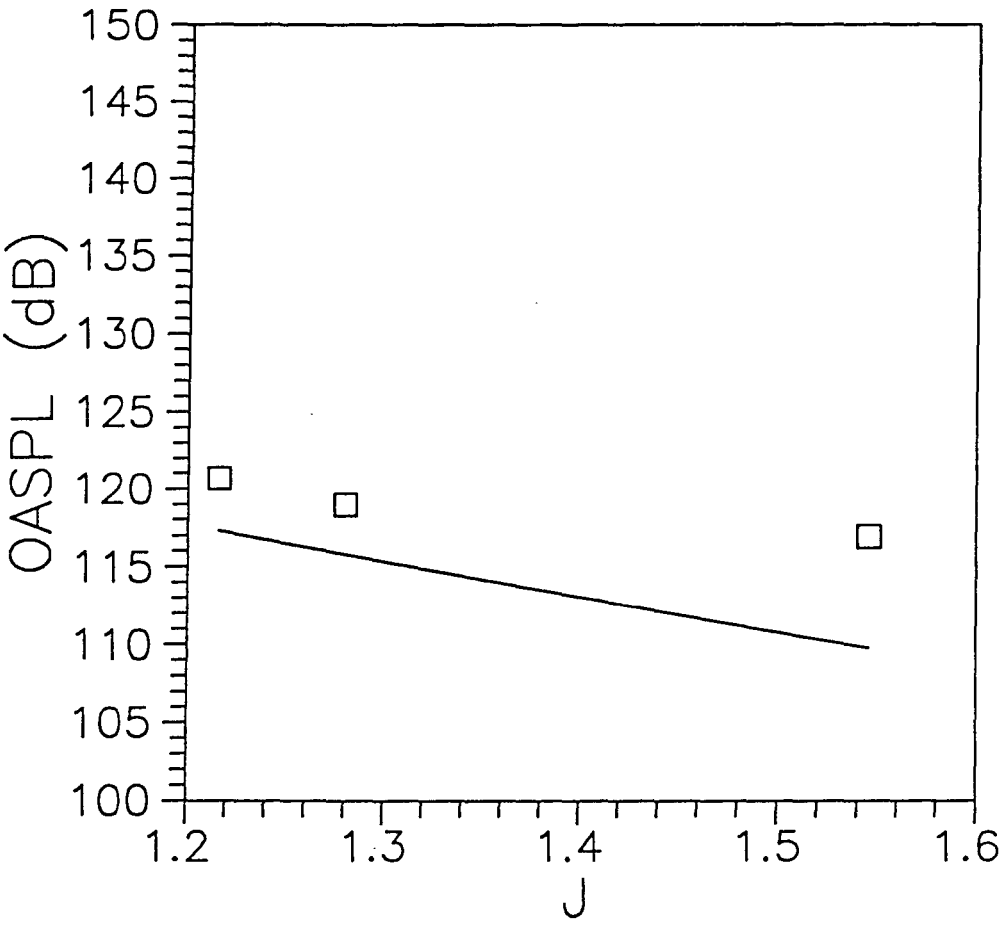

Figure 28. Theoretical and Experimental Noise Level Variation with Advance Ratio; 3×3 Blades; 50° Blade Tip Angle; Y-microphone; $P_{ref} = 20\ \mu$ Pa.

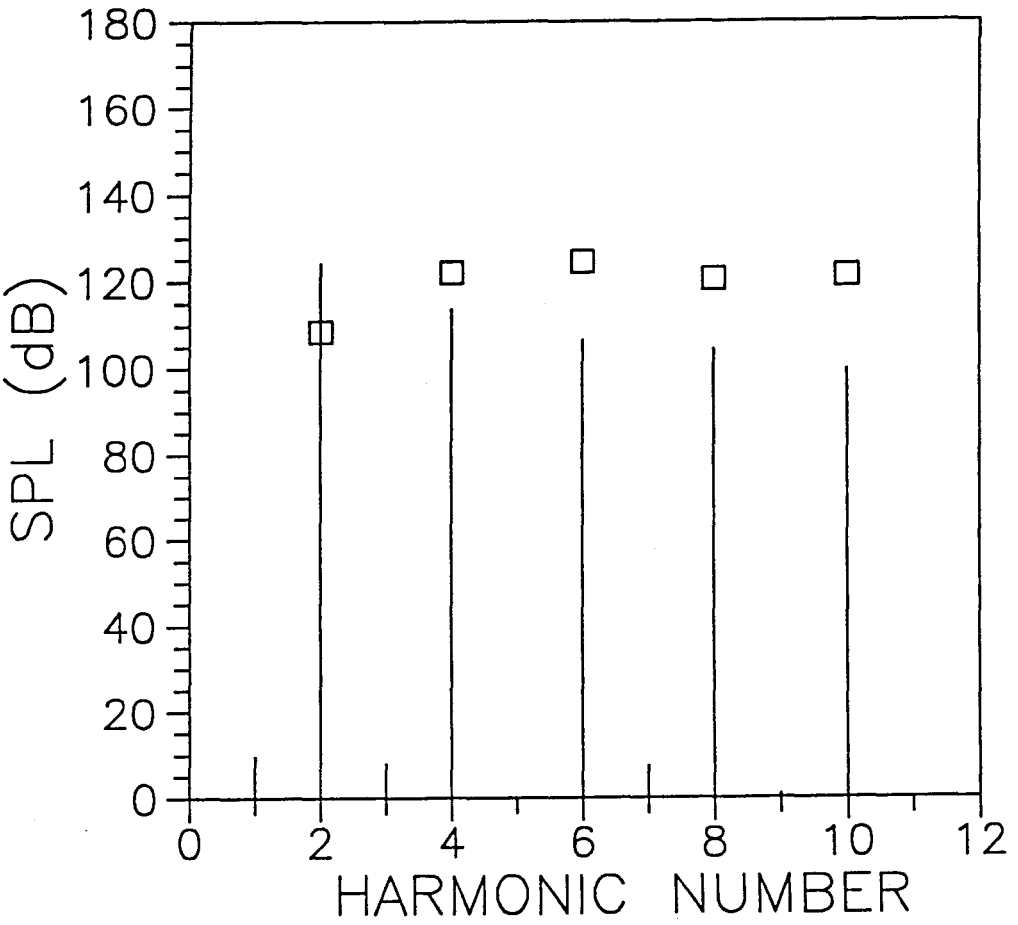

Figure 29. Theoretical and Experimental Frequency Spectra of 3 × 3 Blades Propeller; J=0.861; 40° Blade Tip Angle; Y-microphone; $P_{ref} = 20\ \mu$ Pa.

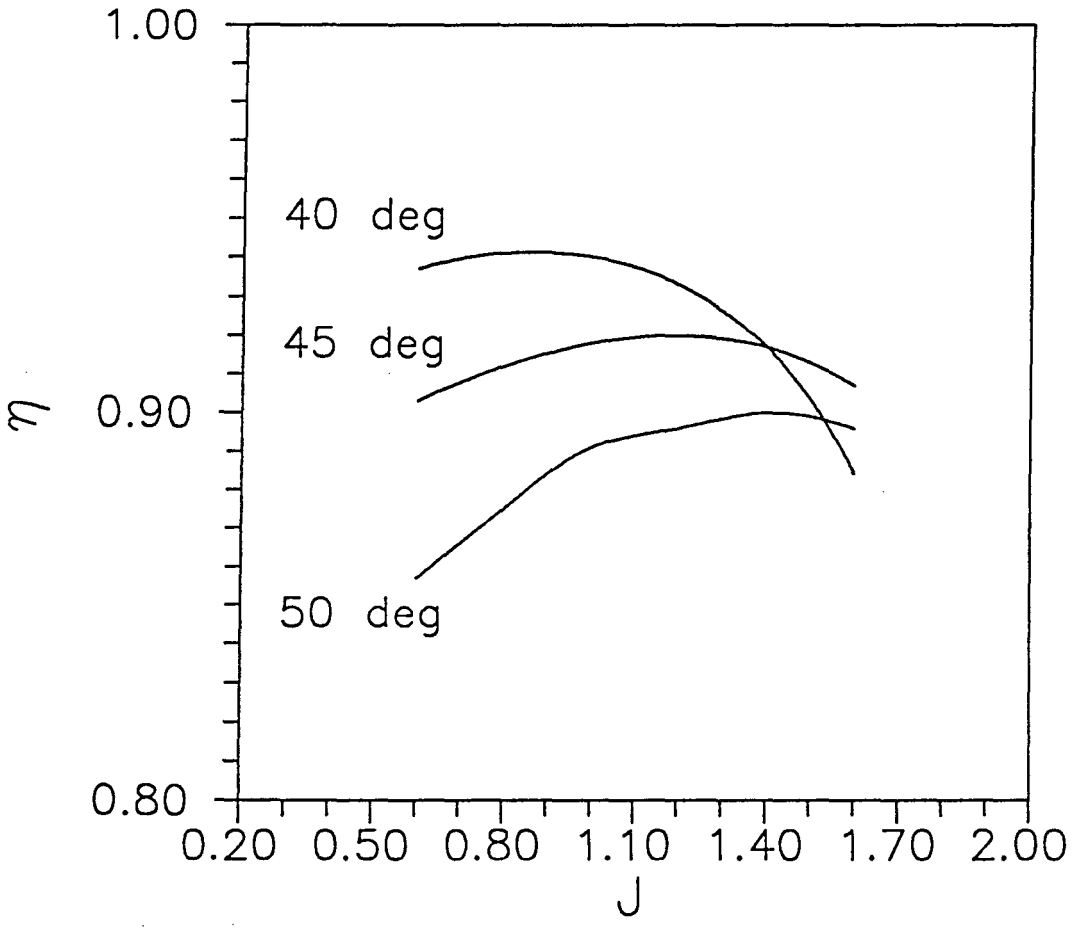

Figure 30. Total 4 × 4 Blade Experimental Propeller Efficiency Variation with Advance Ratio at 40°, 45°, and 50° Blade Tip Angle.

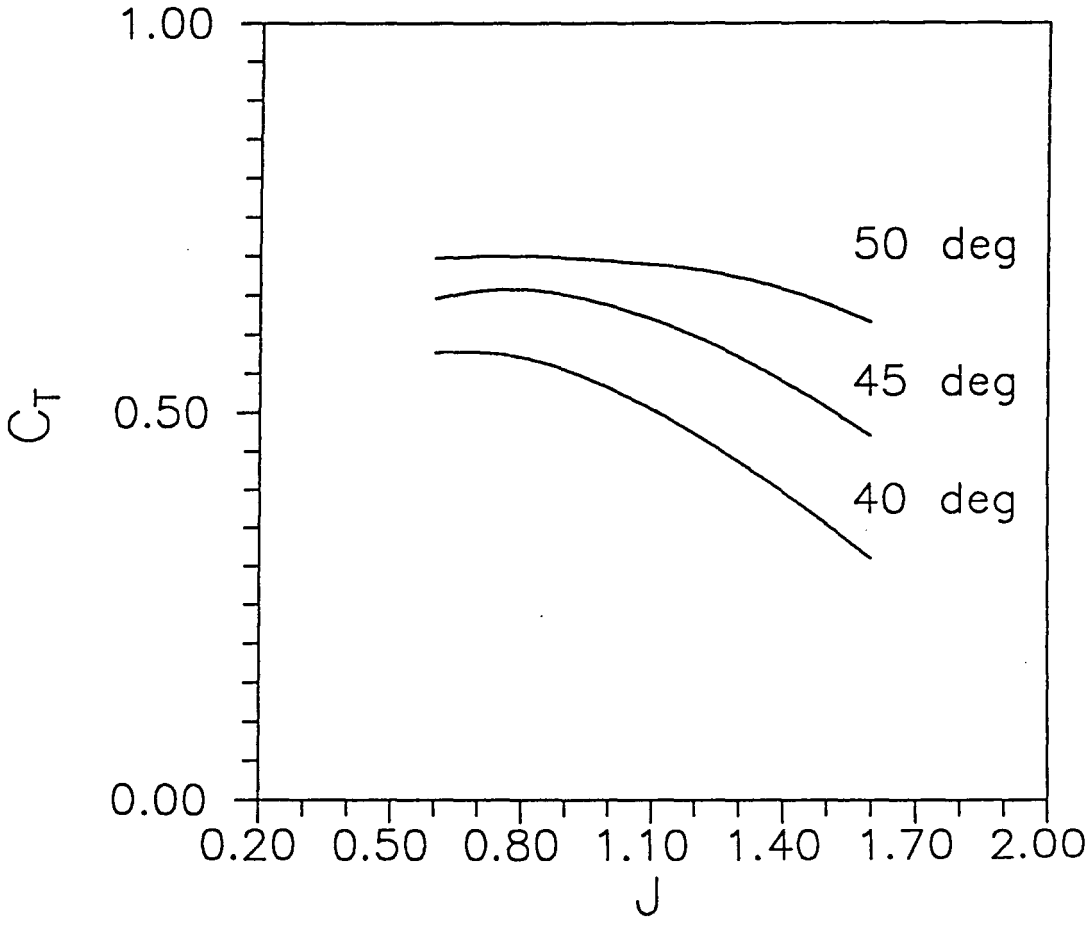

Figure 31. Total 4 × 4 Blade Experimental Propeller Thrust Coefficient Variation with Advance Ratio at 40°, 45°, and 50° Blade Tip Angle.

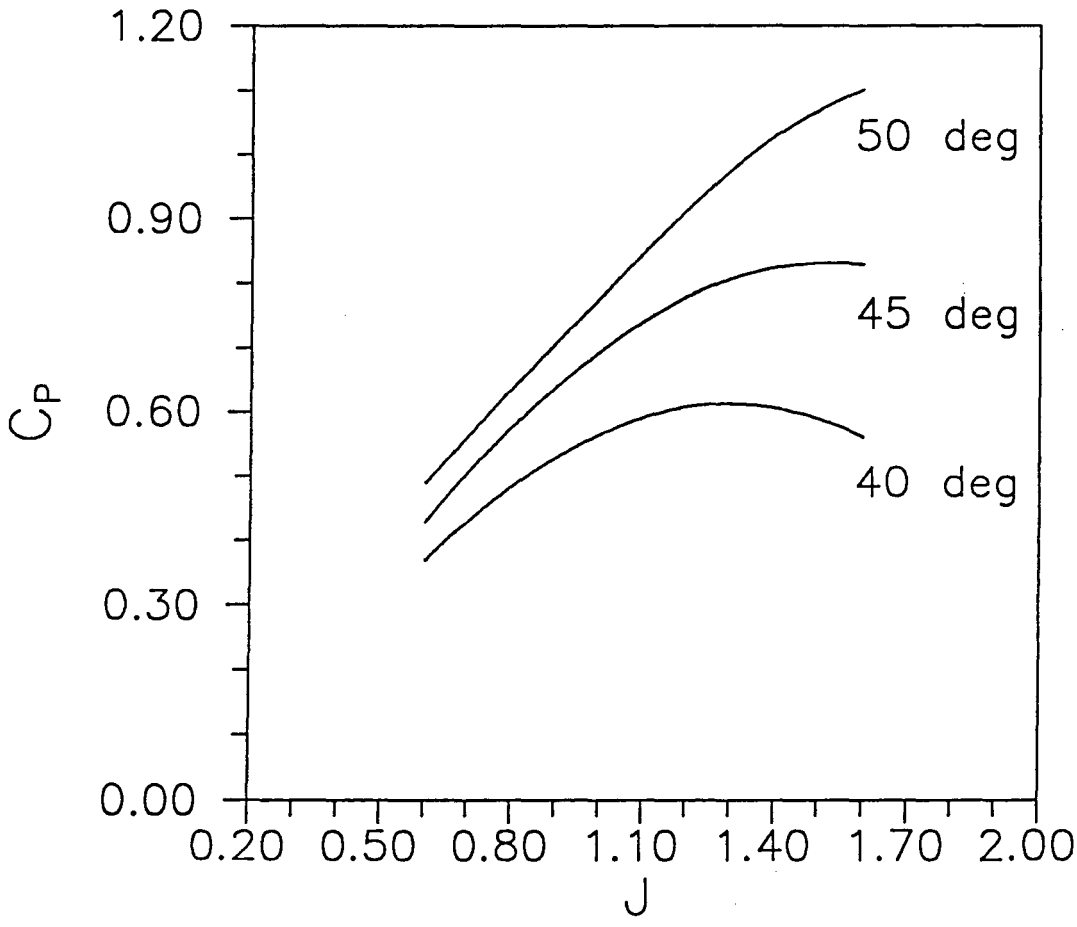

Figure 32. Total 4 × 4 Blade Experimental Propeller Power Coefficient Variation with Advance Ratio at 40°, 45°, and 50° Blade Tip Angle.

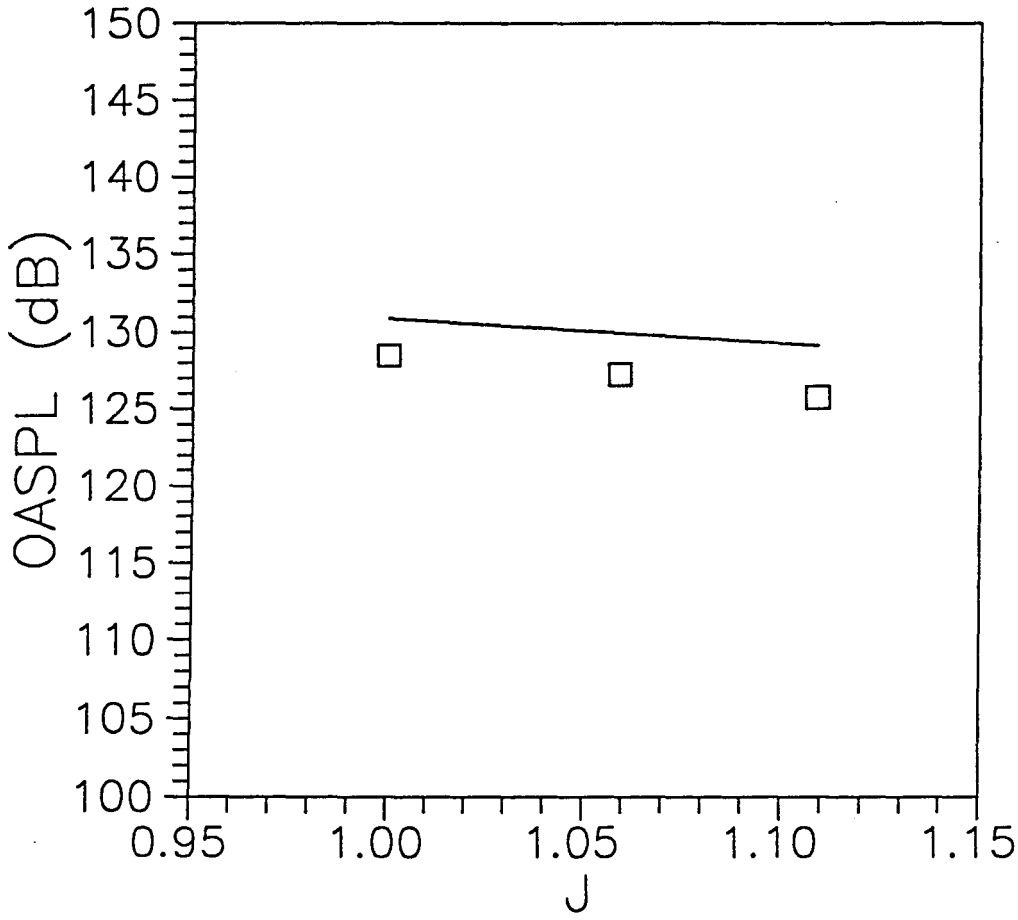

Figure 33. Comparison of Theoretical and Experimental Noise Level Variation with Advance Ratio; 4 × 4 Blades; 40° Blade Tip Angle; X-microphone; P_{ref} = 20 μ Pa.

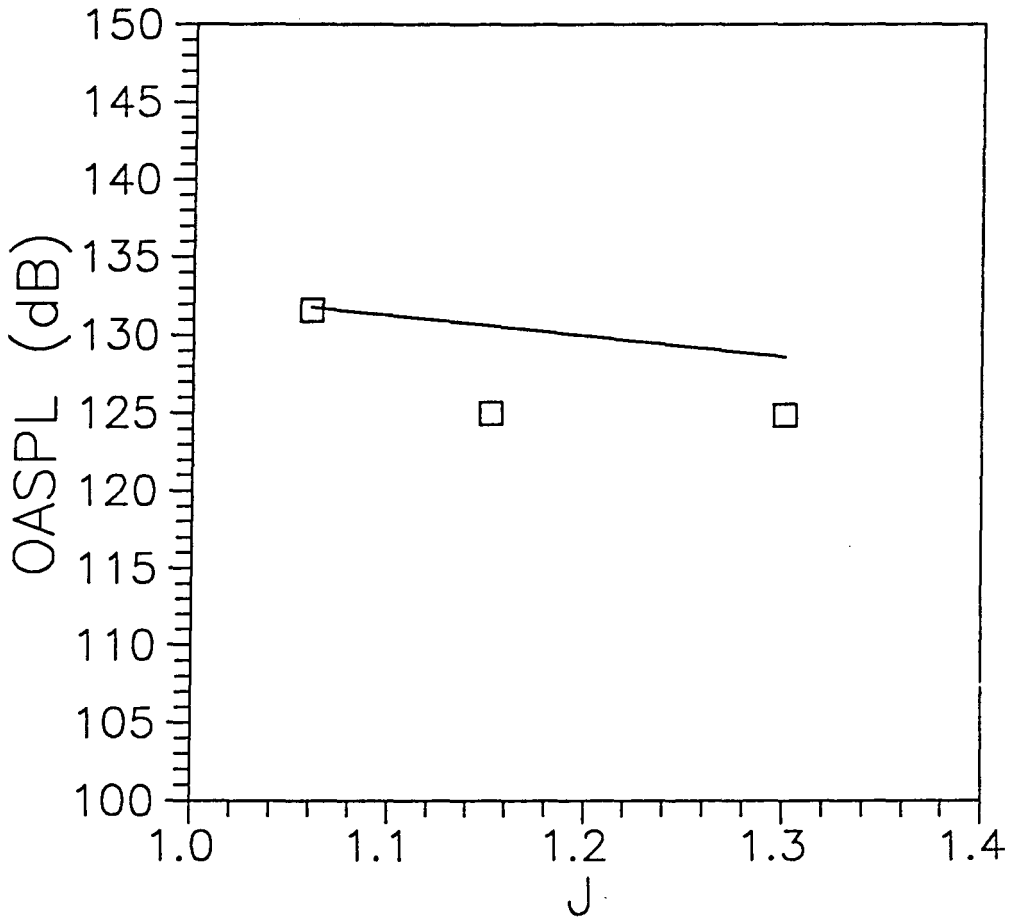

Figure 34. Theoretical and Experimental Noise Level Variation with Advance Ratio; 4×4 Blades; 45° Blade Tip Angle; X-microphone; $P_{ref} = 20\ \mu$ Pa.

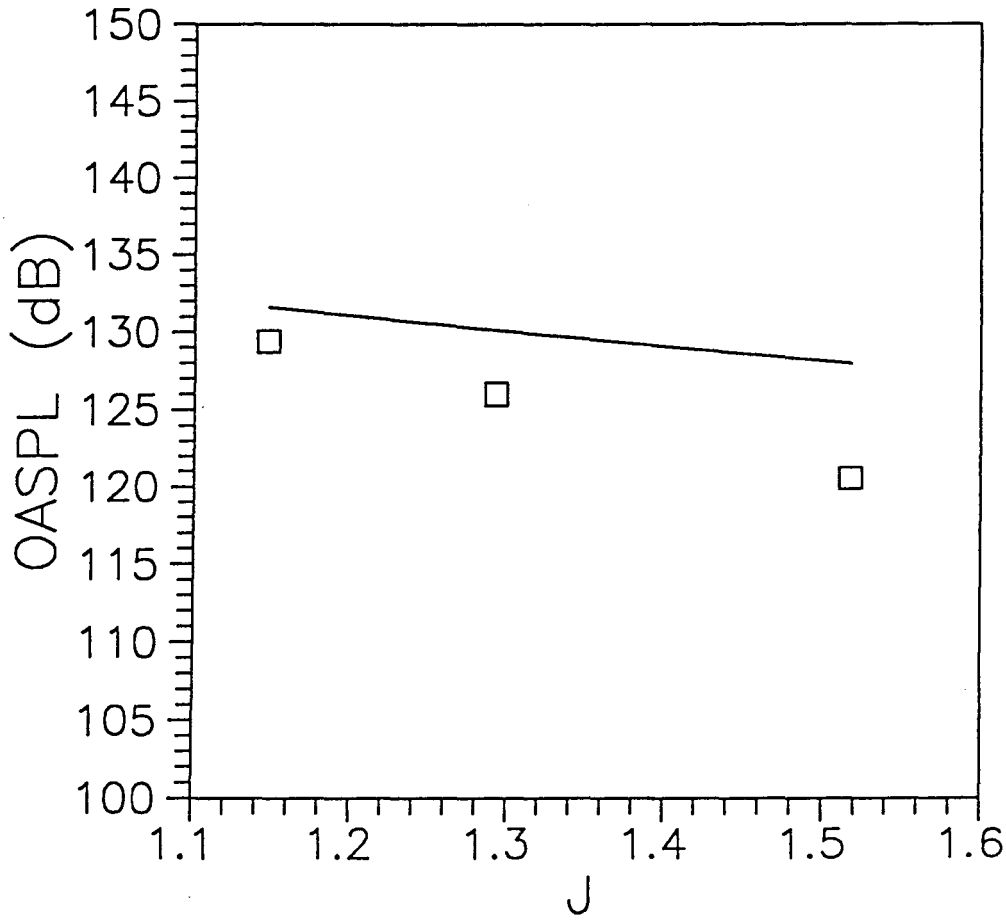

Figure 35. Theoretical and Experimental Noise Level Variation with Advance Ratio; 4×4 Blades; 50° Blade Tip Angle; X-microphone; $P_{ref} = 20\ \mu$ Pa.

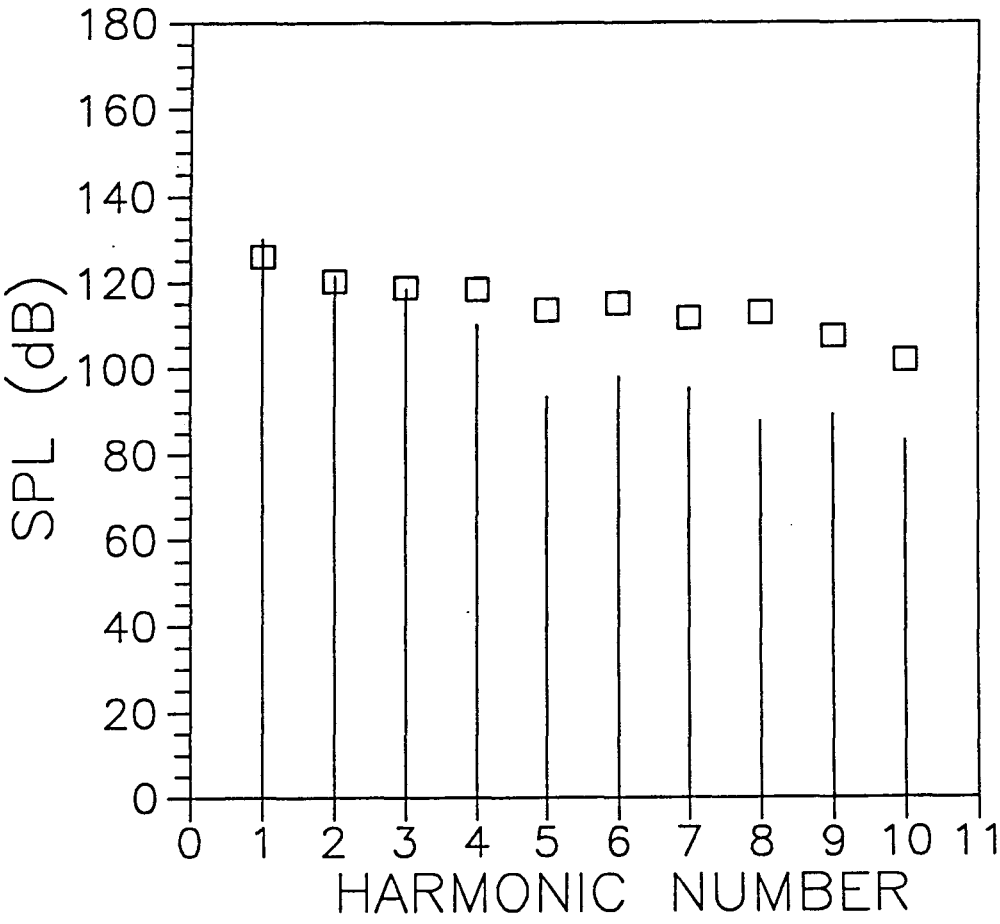

Figure 36. Theoretical and Experimental Frequency Spectra of 4 × 4 Blades Propeller; J=0.861; 40° Blade Tip Angle; X-microphone; $P_{ref} = 20\ \mu$ Pa.

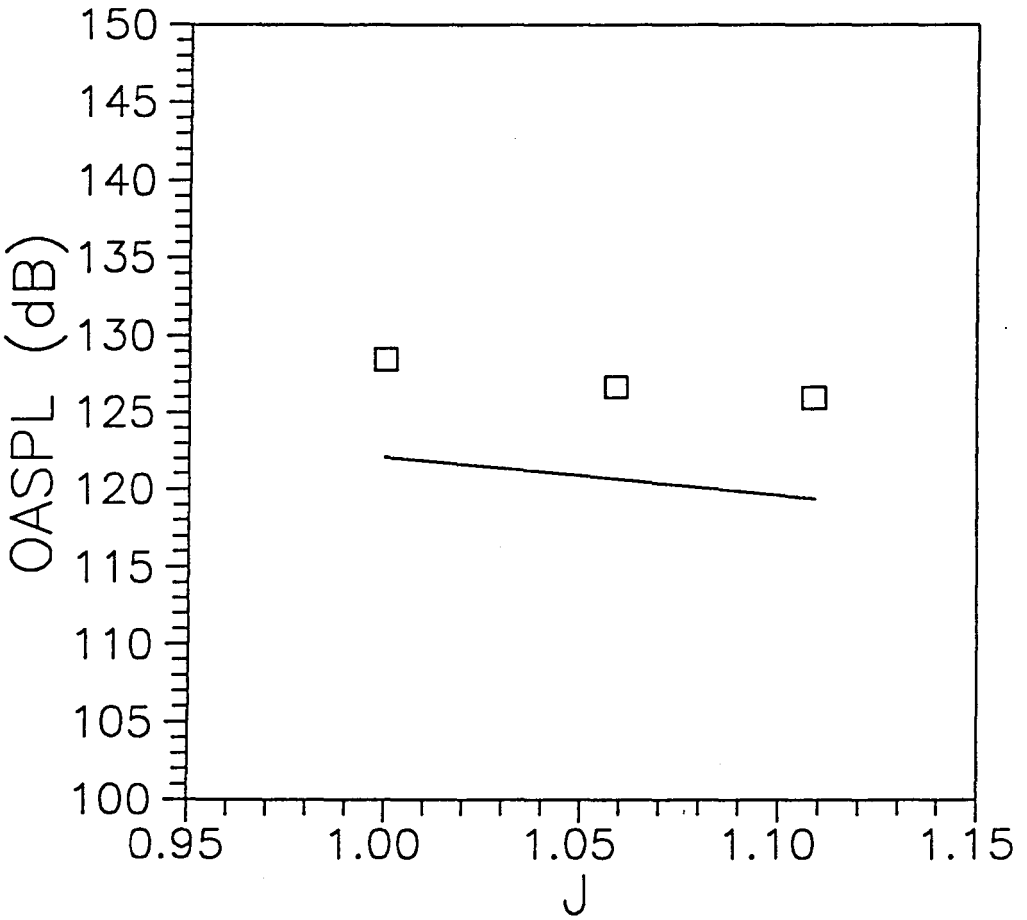

Figure 37. Theoretical and Experimental Noise Level Variation with Advance Ratio; 4×4 Blades; 40° Blade Tip Angle; Y-microphone; $P_{ref} = 20\ \mu$ Pa.

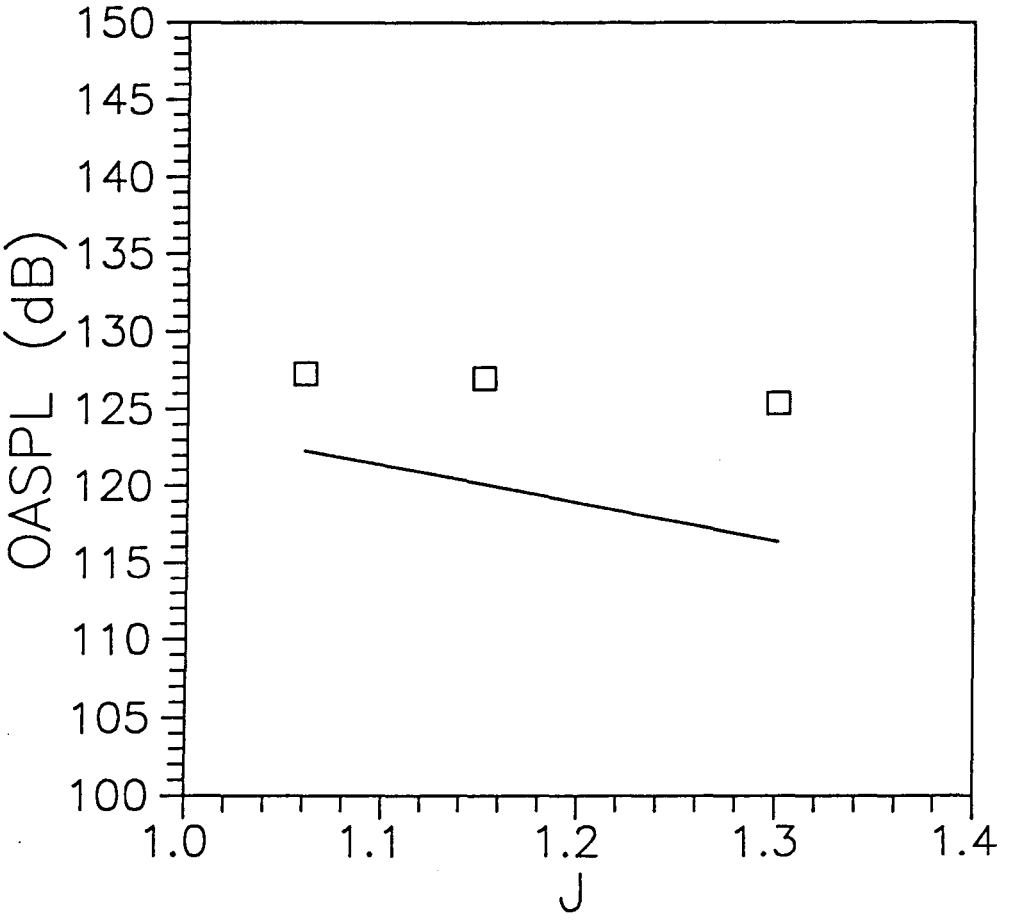

Figure 38. Theoretical and Experimental Noise Level Variation with Advance Ratio; 4×4 Blades; 45° Blade Tip Angle; Y-microphone; $P_{ref} = 20\ \mu$ Pa.

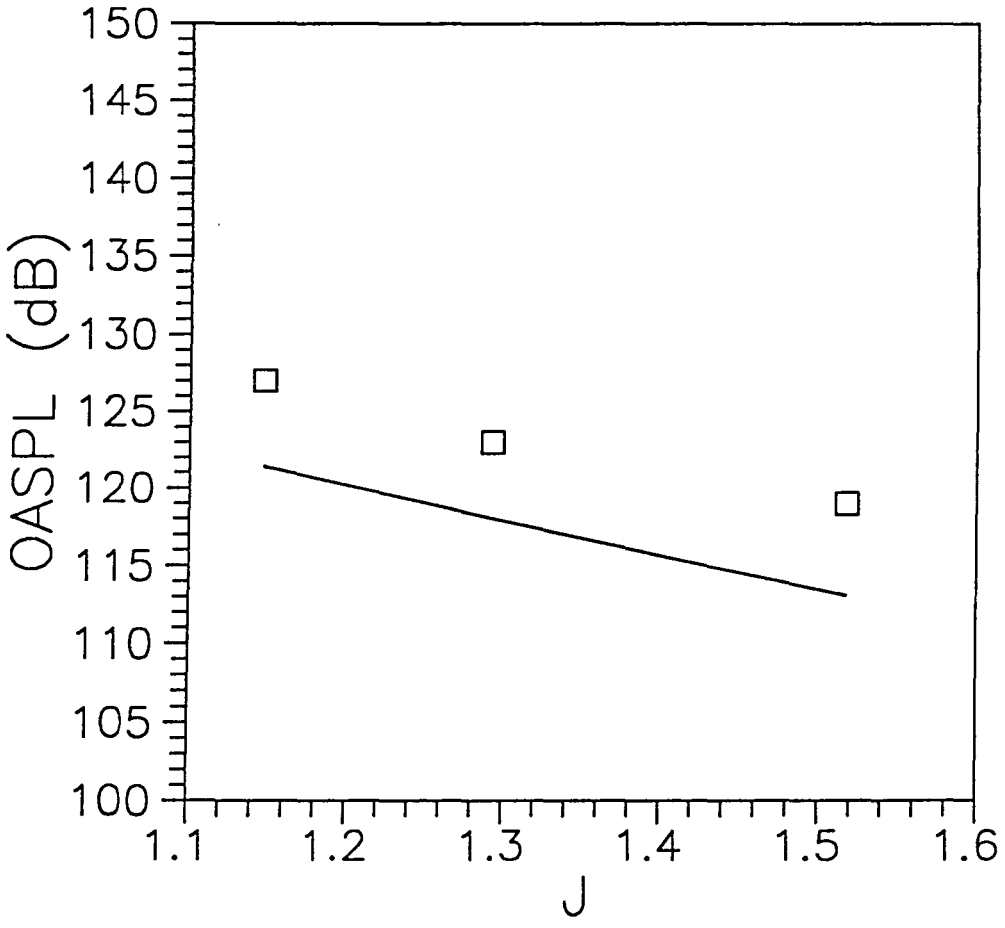

Figure 39. Theoretical and Experimental Noise Level Variation with Advance Ratio; 4×4 Blades; 50° Blade Tip Angle; Y-microphone; $P_{ref} = 20\ \mu$ Pa.

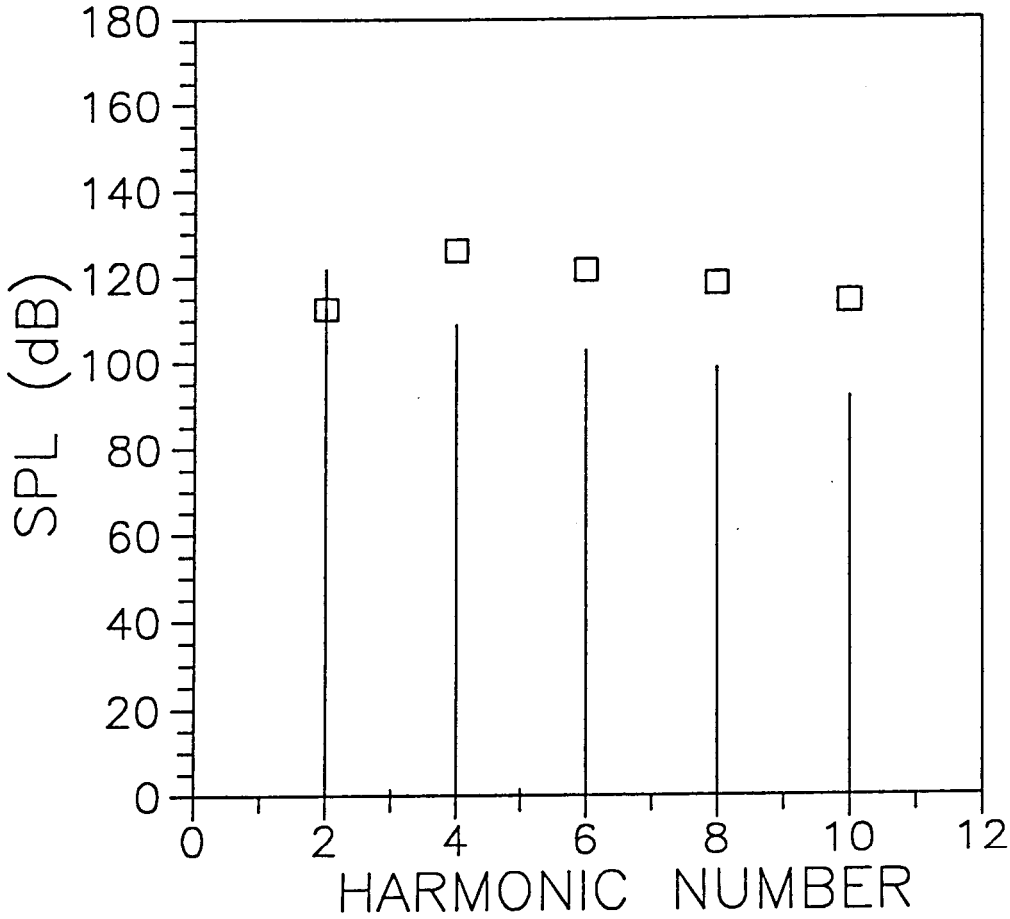

Figure 40. Theoretical and Experimental Frequency Spectra of 4 × 4 Blades Propeller; J=0.861; 40° Blade Tip Angle; Y-microphone; $P_{ref} = 20\ \mu$ Pa.

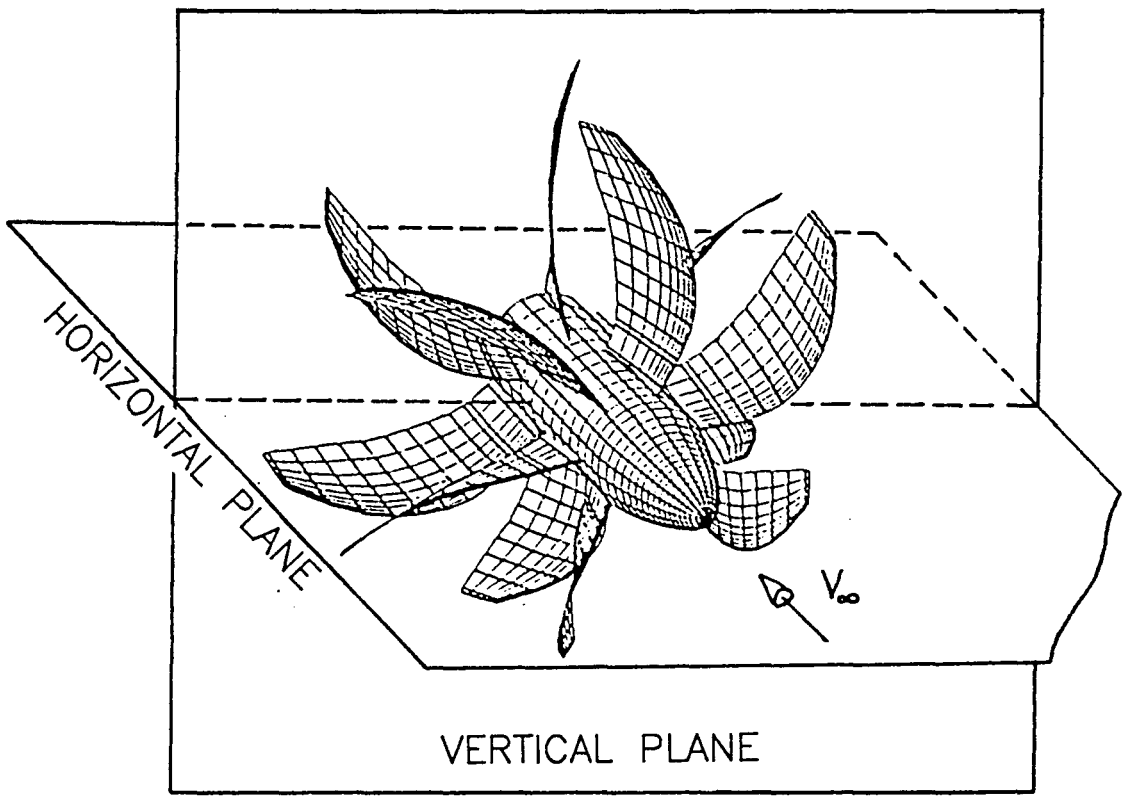

Figure 41. Horizontal and Disk Planes of Counterrotating Propeller Configuration.

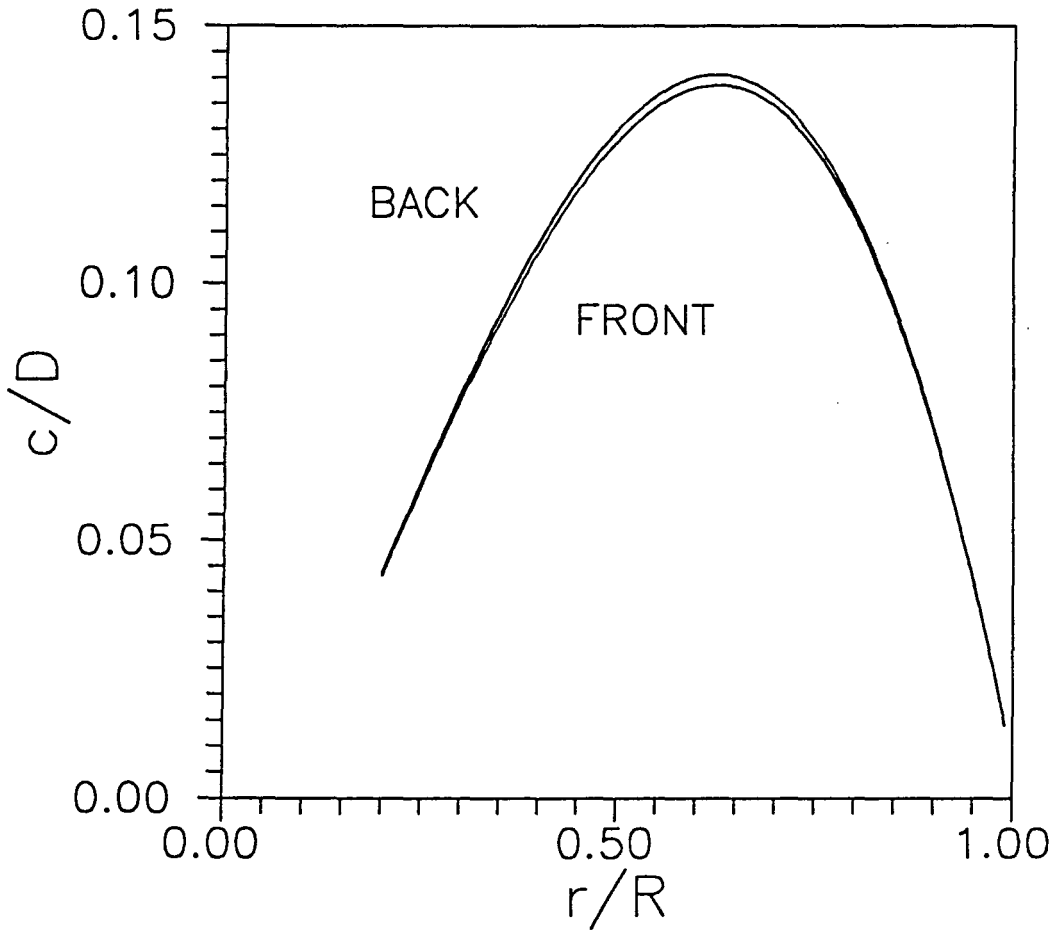

Figure 42. Radial Chord-to-Diameter Ratio Distribution of Commuter-Class Configuration Propeller Blades.

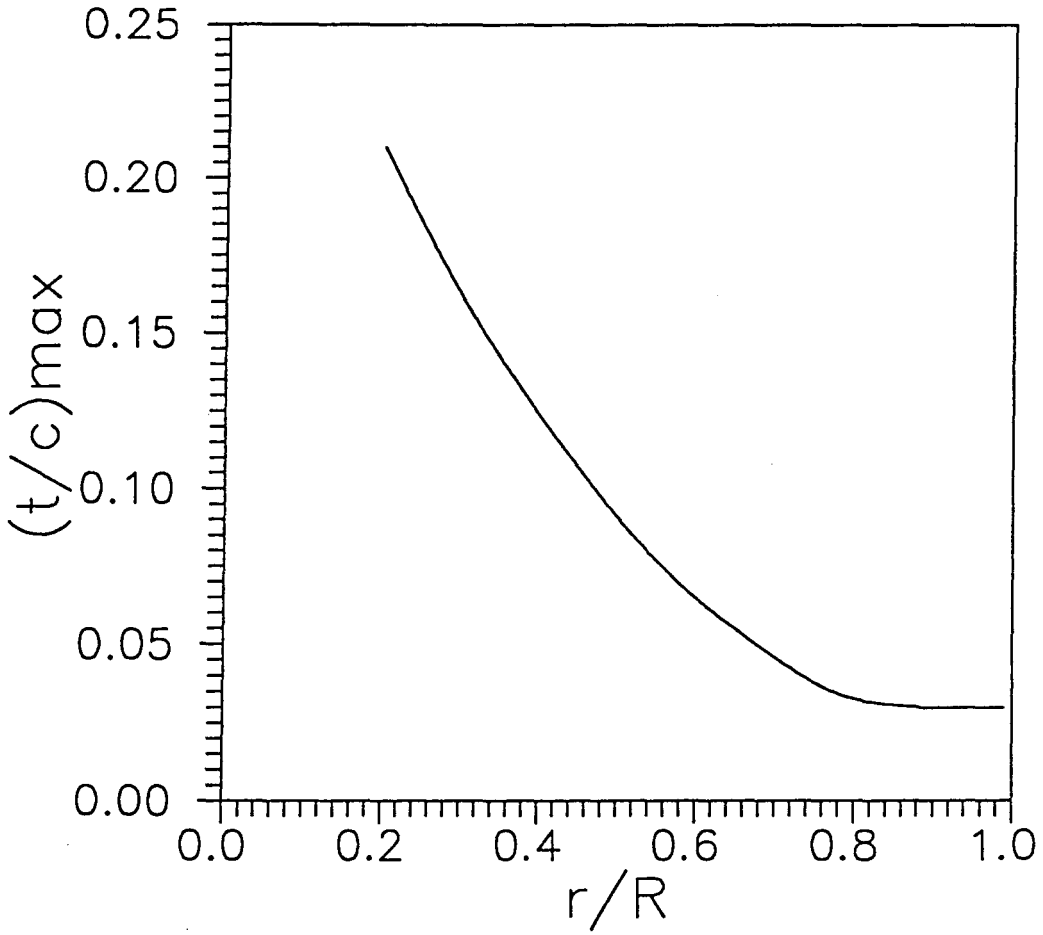

Figure 43. Radial Maximum Thickness-to-Chord Ratio Distribution of Commuter-Class Configuration Propeller Blades.

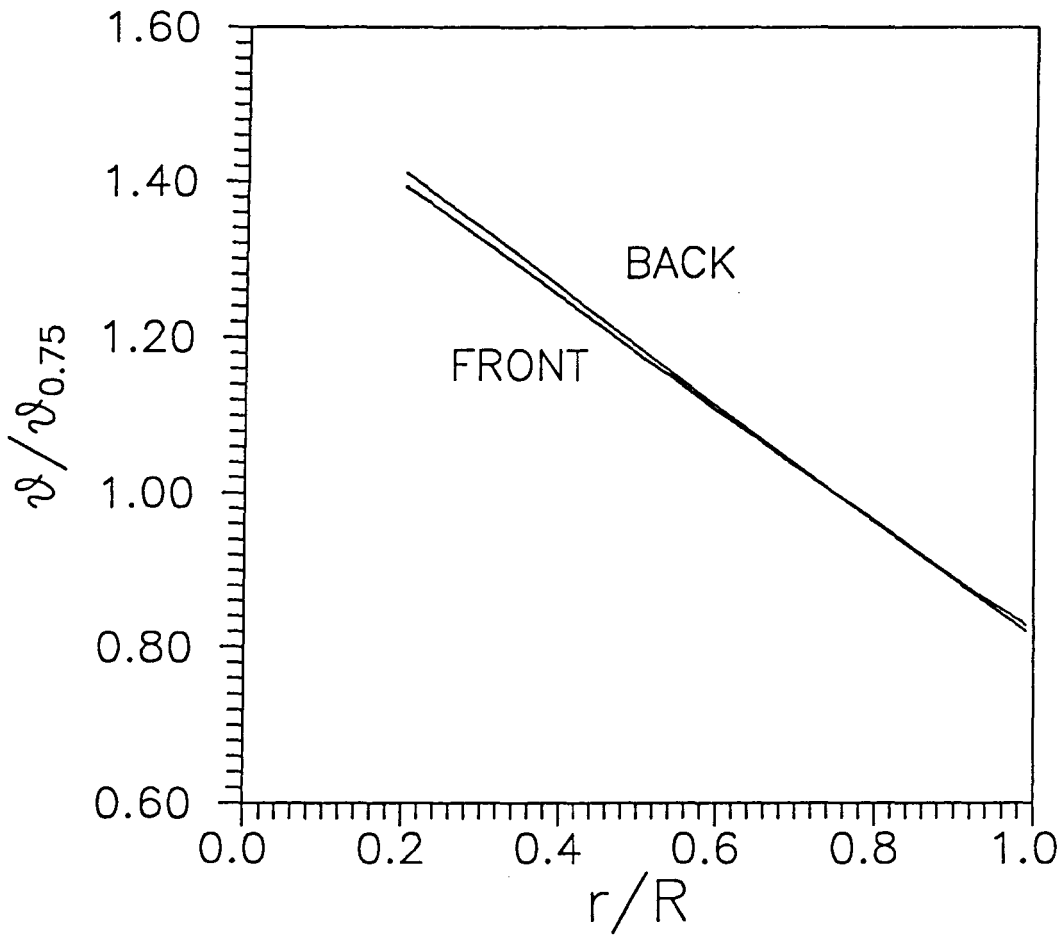

Figure 44. Radial Blade Twist Distribution of Commuter-Class Configuration Propeller Blades Nondimensionalized by the Blade Twist at the 75 % Location.

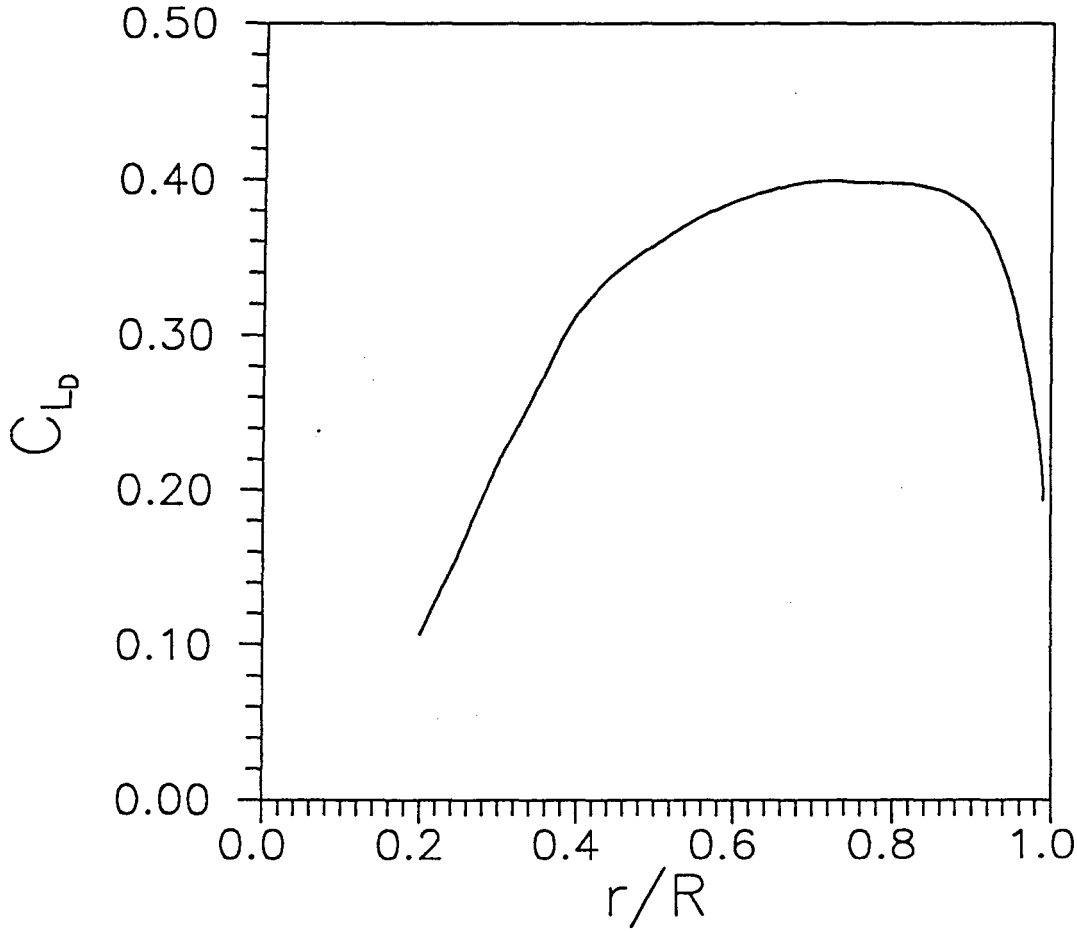

Figure 45. Radial Design Lift Coefficient Distribution of Commuter-Class Propeller Blades.

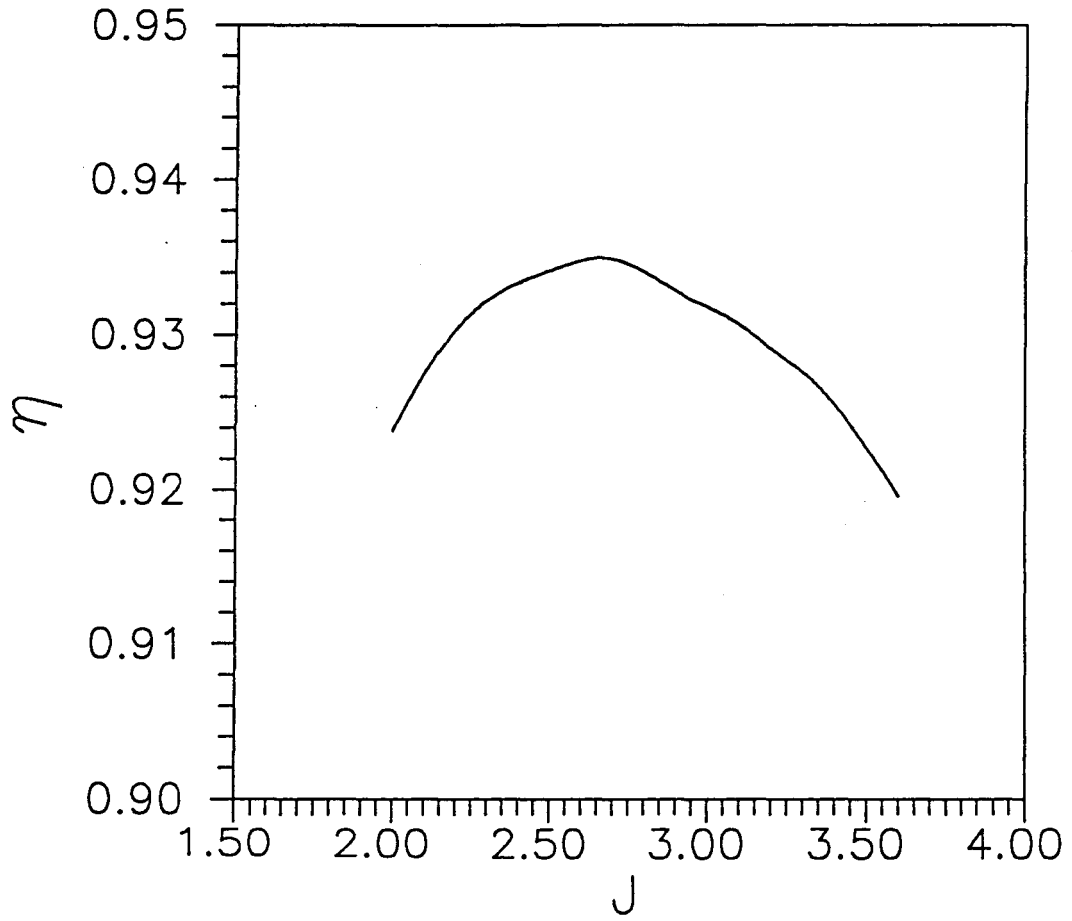

Figure 46. Total Commuter-Class Propeller Efficiency Variation with Advance Ratio.

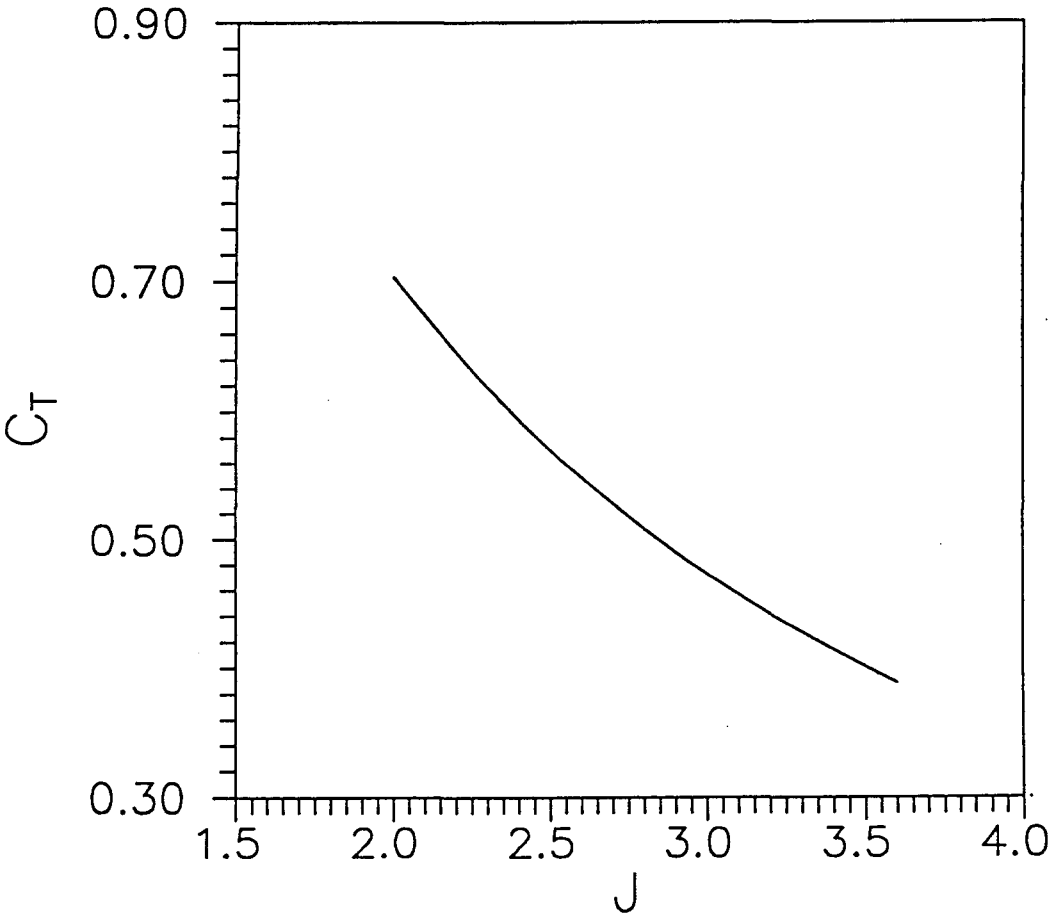

Figure 47. Total Commuter-Class Propeller Thrust Coefficient Variation with Advance Ratio.

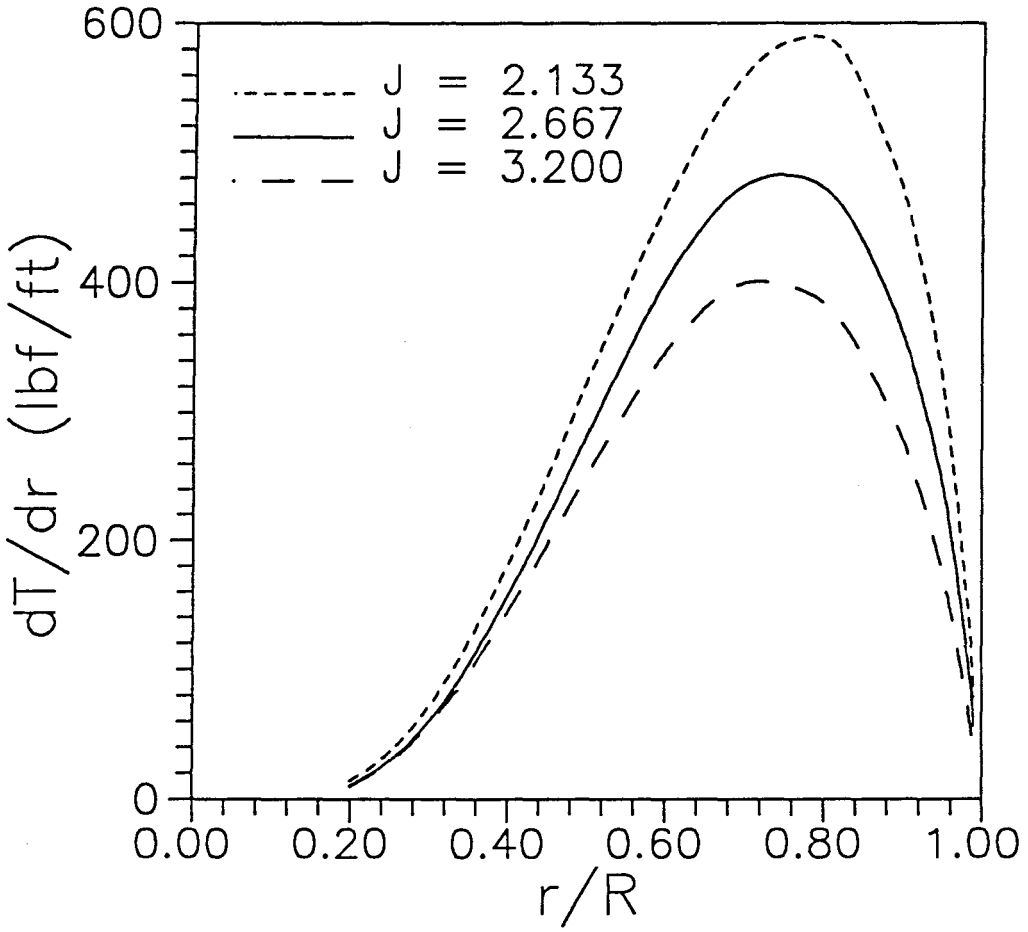

Figure 48. Radial Variation of Differential Thrust with Advance Ratio on Front Propeller of Commuter-Class Propeller Configuration.

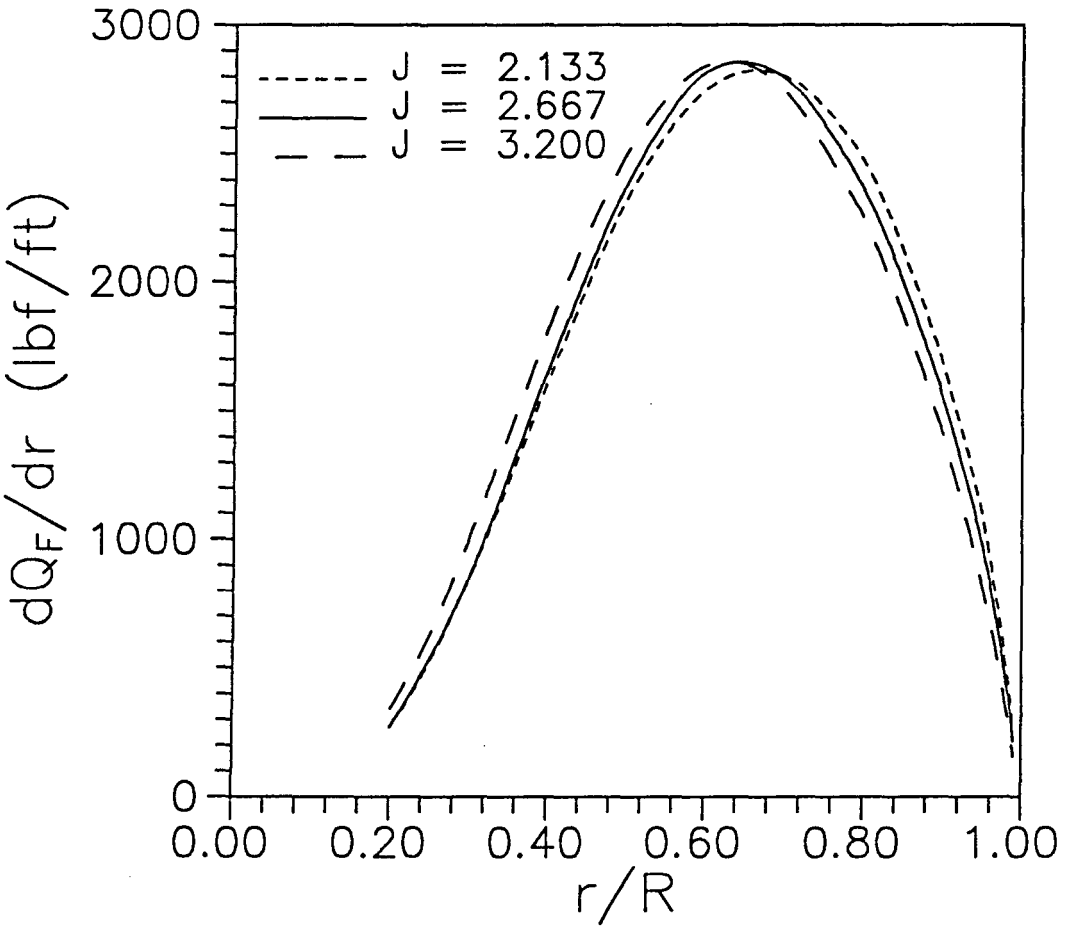

Figure 49. Radial Variation of Differential Torque-Force with Advance Ratio on Front Propeller of Commuter-Class Propeller Configuration.

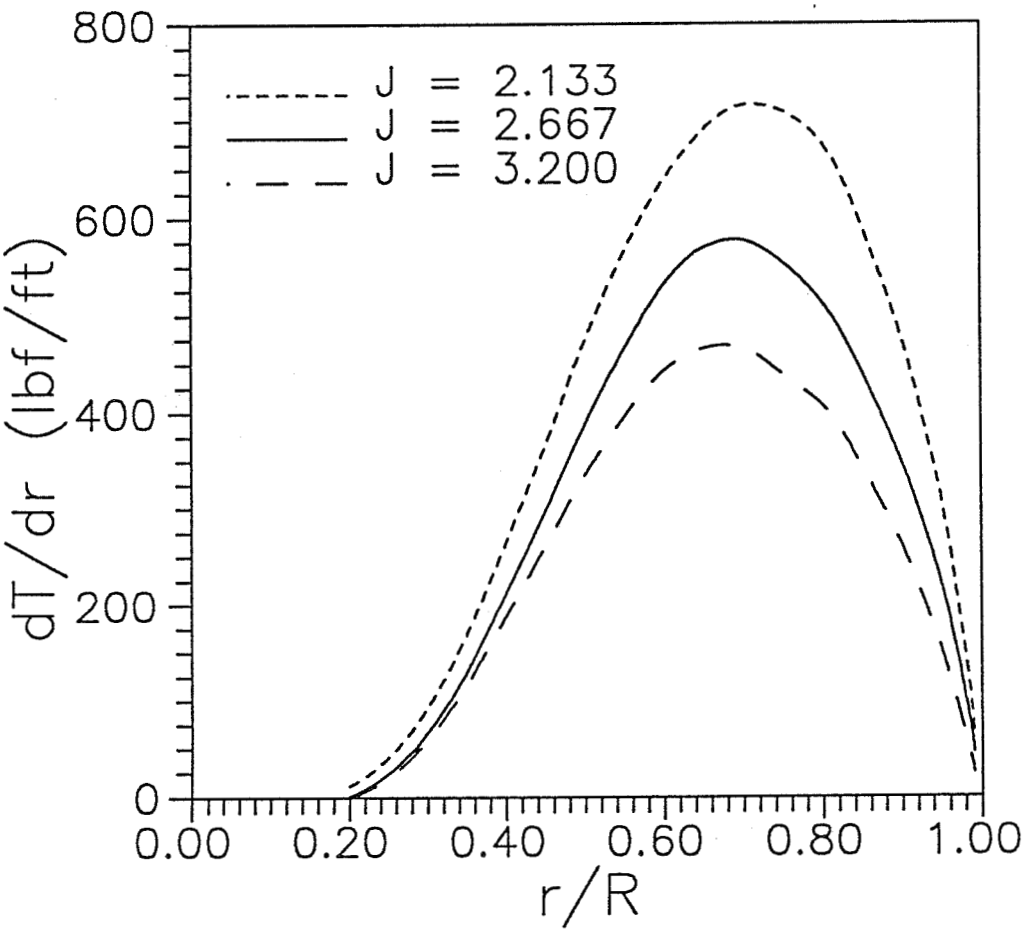

Figure 50. Radial Variation of Differential Thrust with Advance Ratio on Back Propeller of Commuter-Class Propeller Configuration.

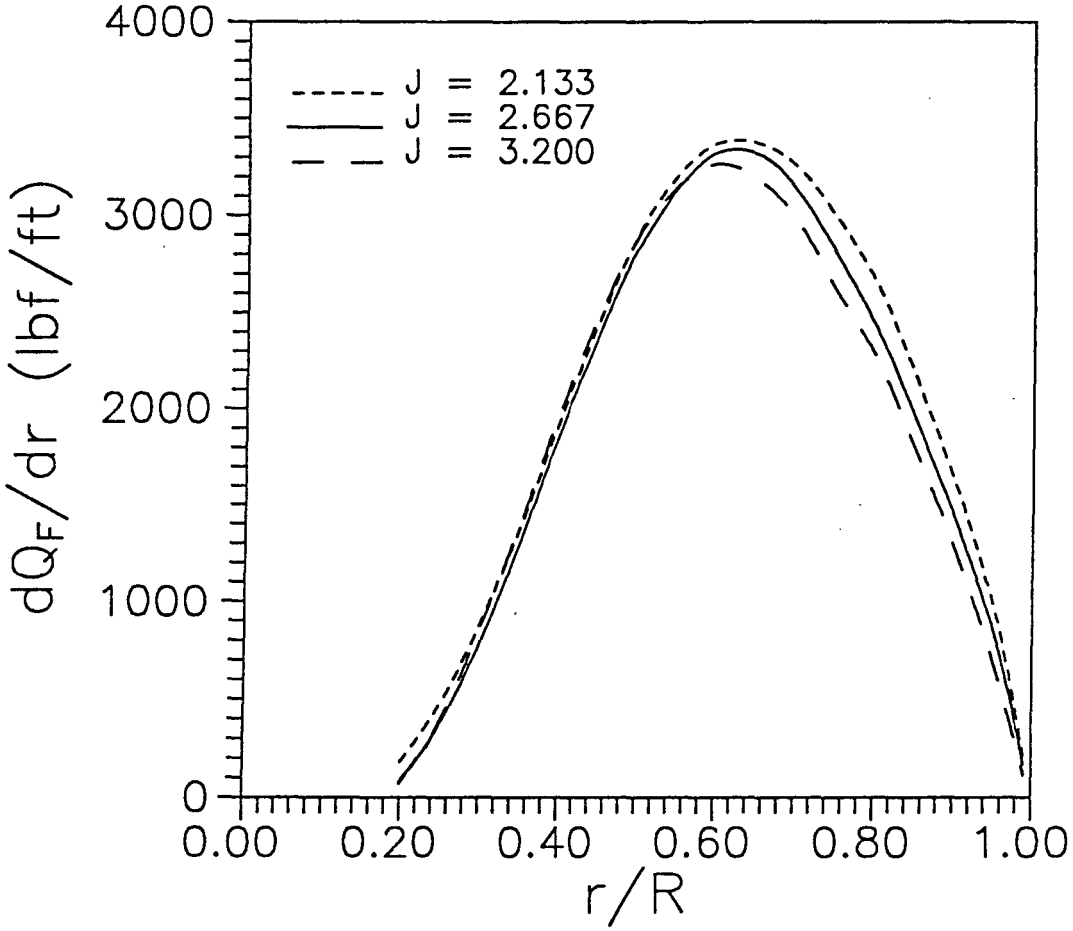

Figure 51. Radial Variation of Differential Torque-Force with Advance Ratio on Back Propeller of Commuter-Class Propeller Configuration.

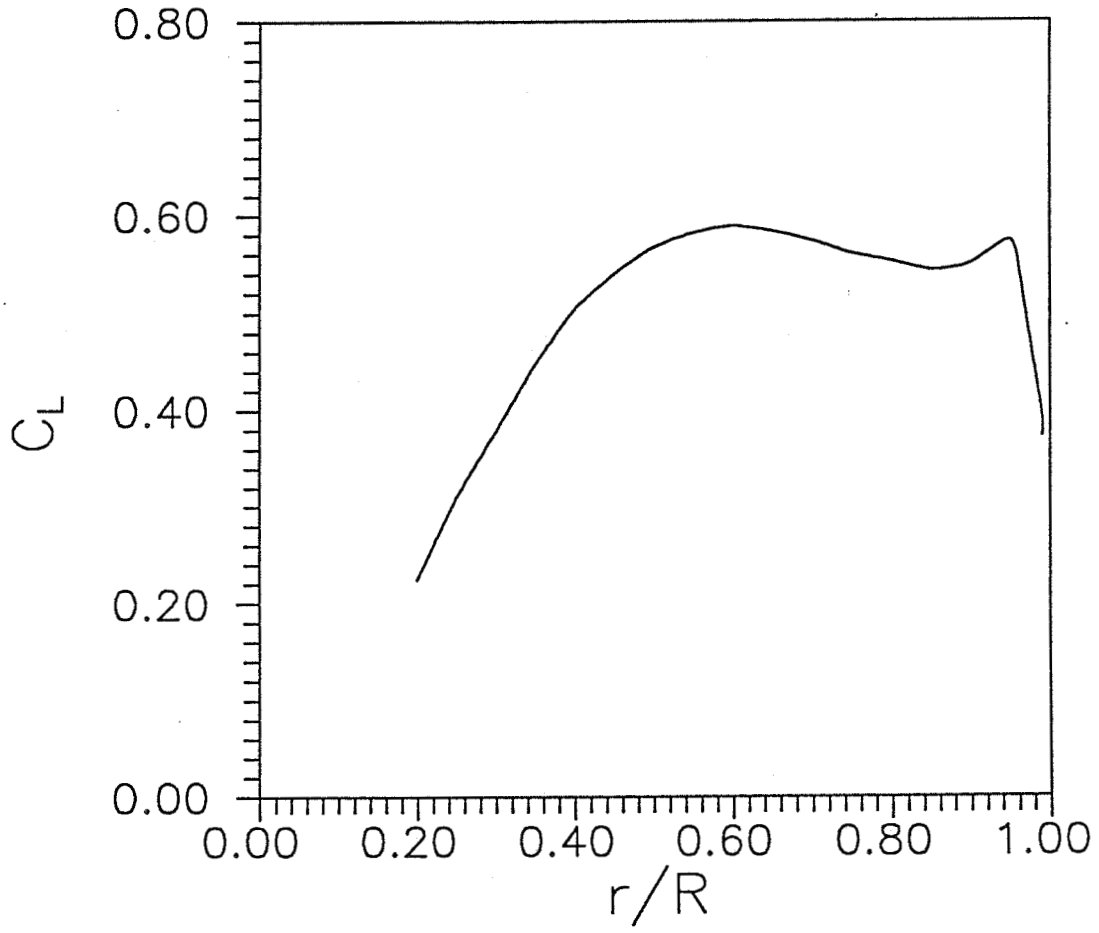

Figure 52. Radial Variation of Lift Coefficient on Front Propeller of Commuter-Class Propeller Configuration; J=2.67.

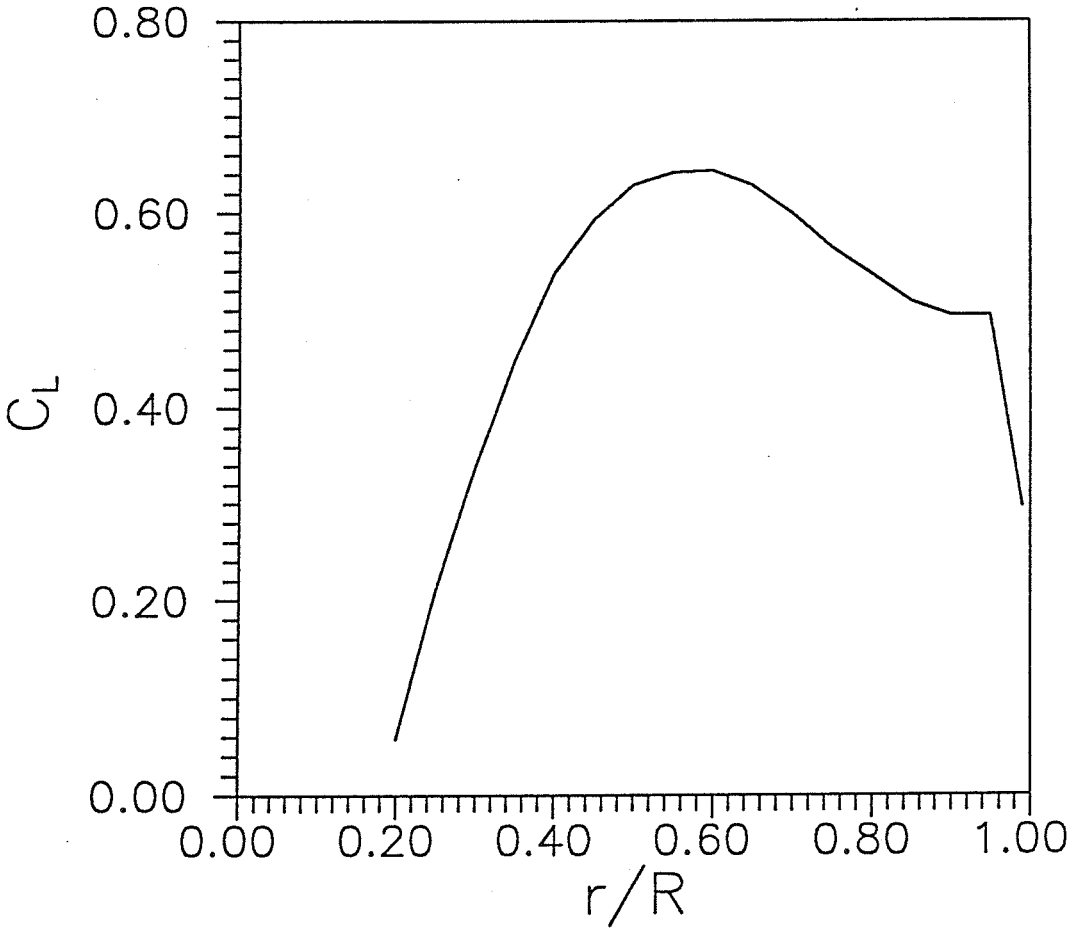

Figure 53. Radial Variation of Lift Coefficient on Back Propeller of Commuter-Class Propeller Configuration; J=2.67.

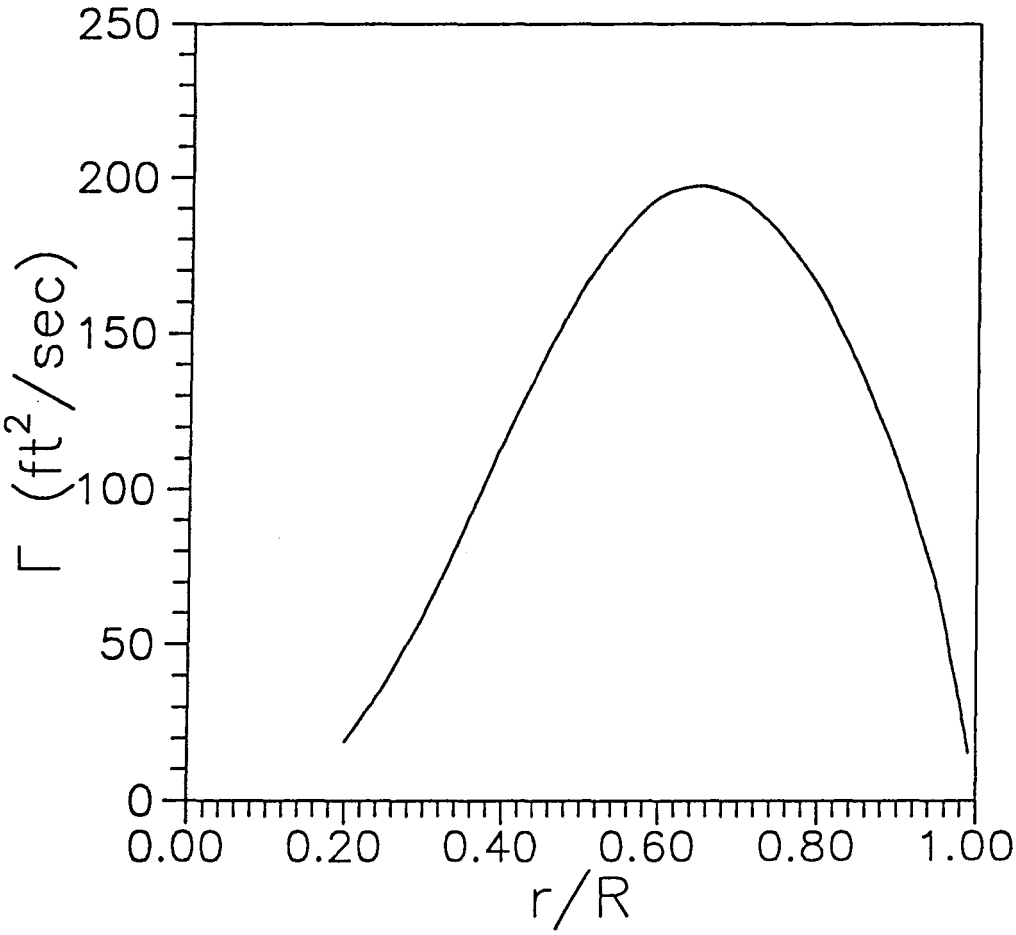

Figure 54. Radial Variation of Circulation Strength with Advance Ratio on Front Propeller of Commuter-Class Propeller Configuration.

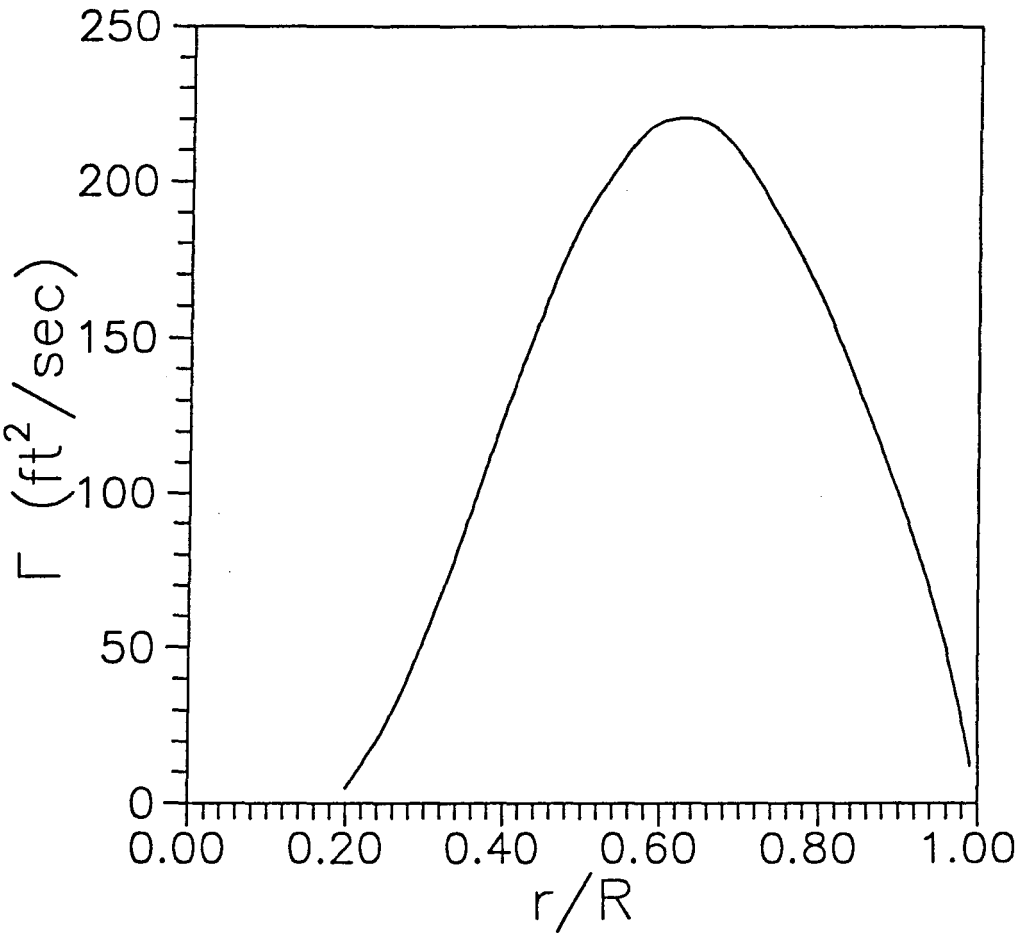

Figure 55. Radial Variation of Circulation Strength with Advance Ratio on Front Propeller of Commuter-Class Propeller Configuration.

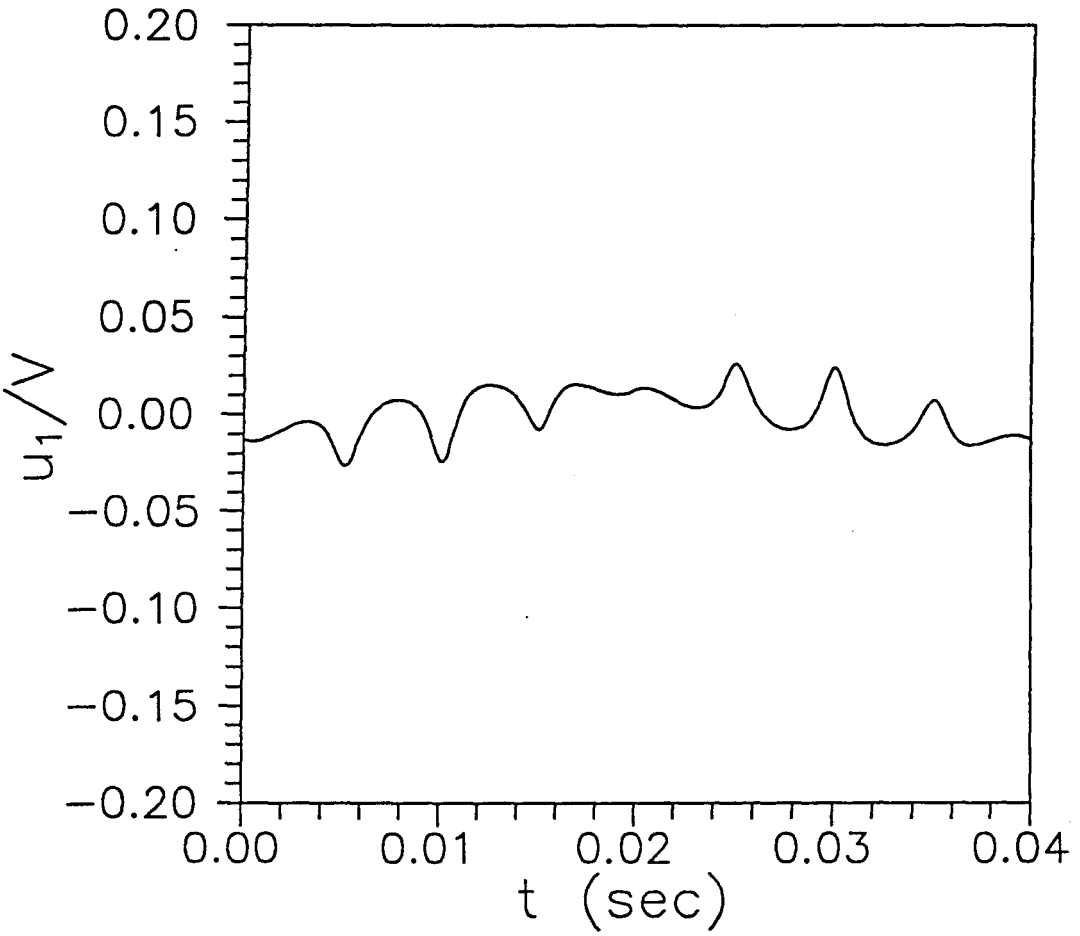

Figure 56. Induced Velocity Ratio in X-direction at 75 % Radial Station of Front Propeller During One Blade Revolution; J=2.67.

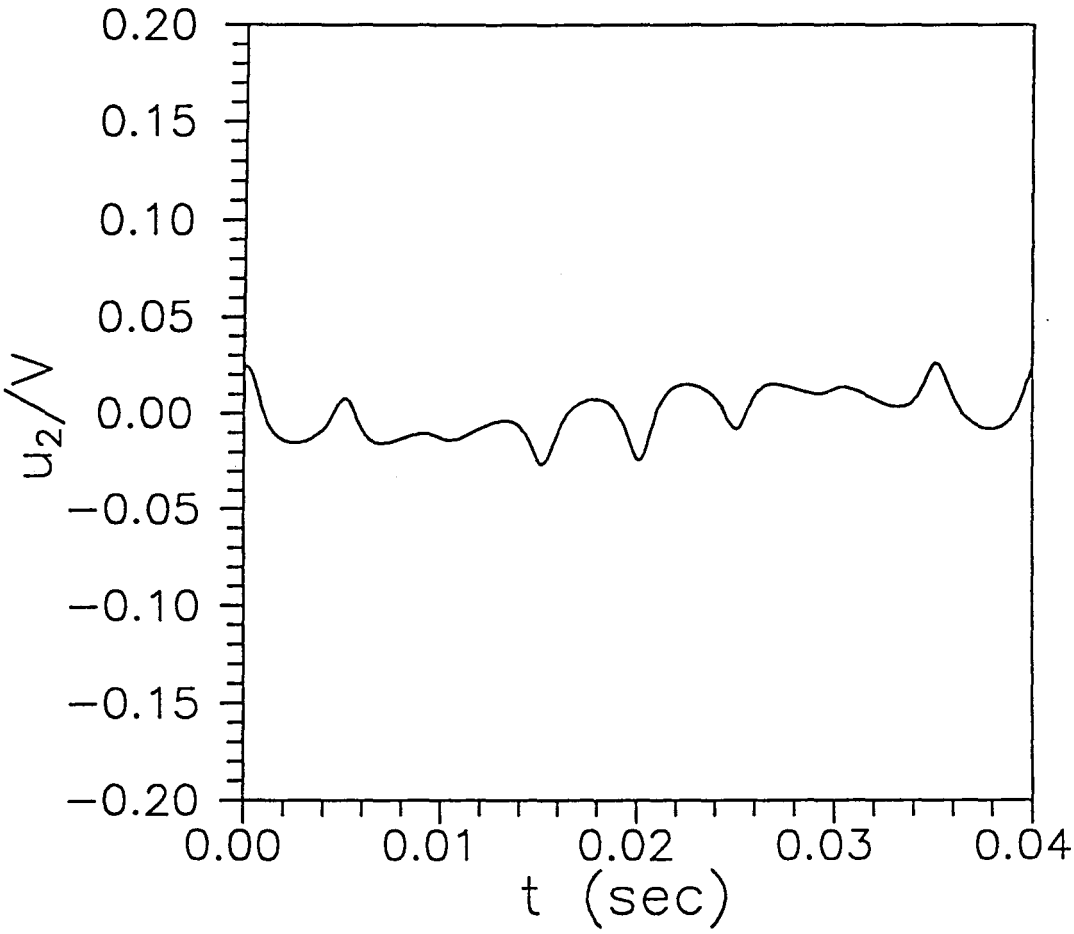

Figure 57. Induced Velocity Ratio in Y-direction at 75 % Radial Station of Front Propeller During One Blade Revolution; J=2.67.

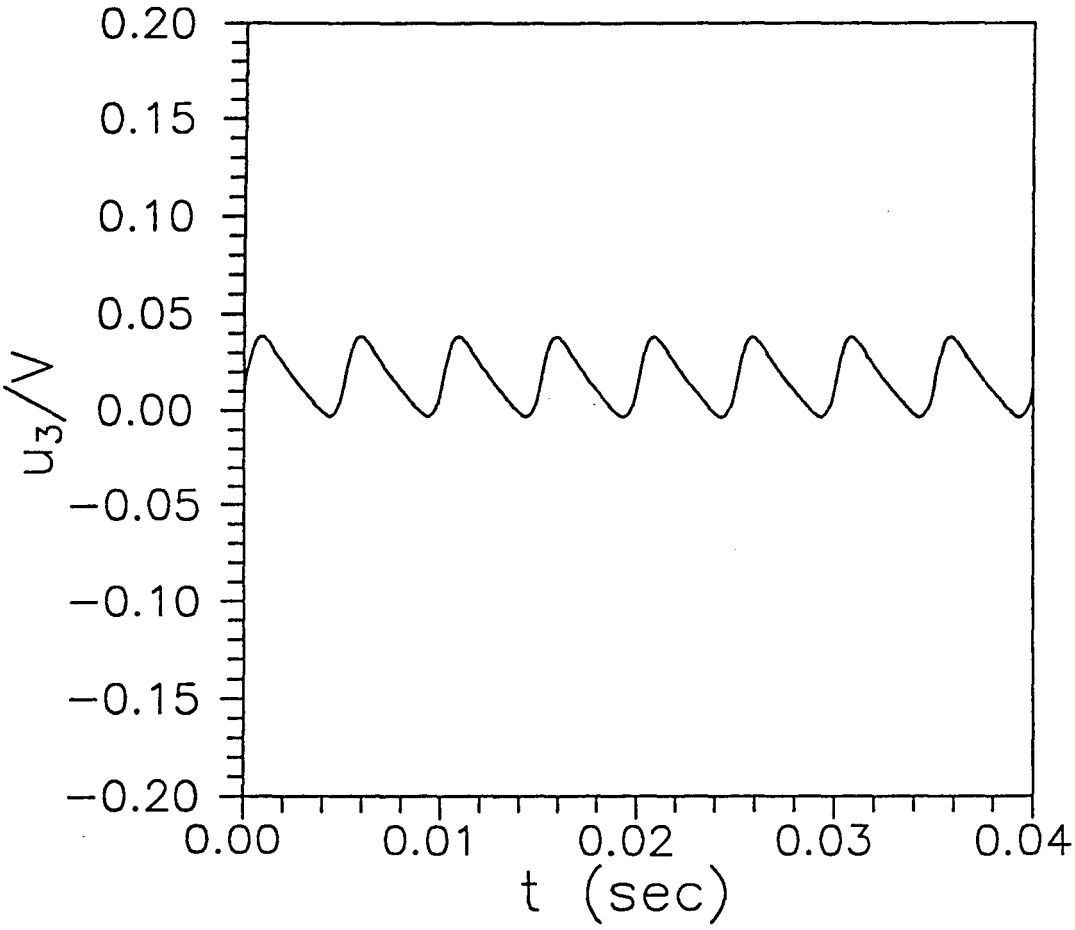

Figure 58. Induced Velocity Ratio in Z-direction at 75 % Radial Station of Front Propeller During One Blade Revolution; J=2.67.

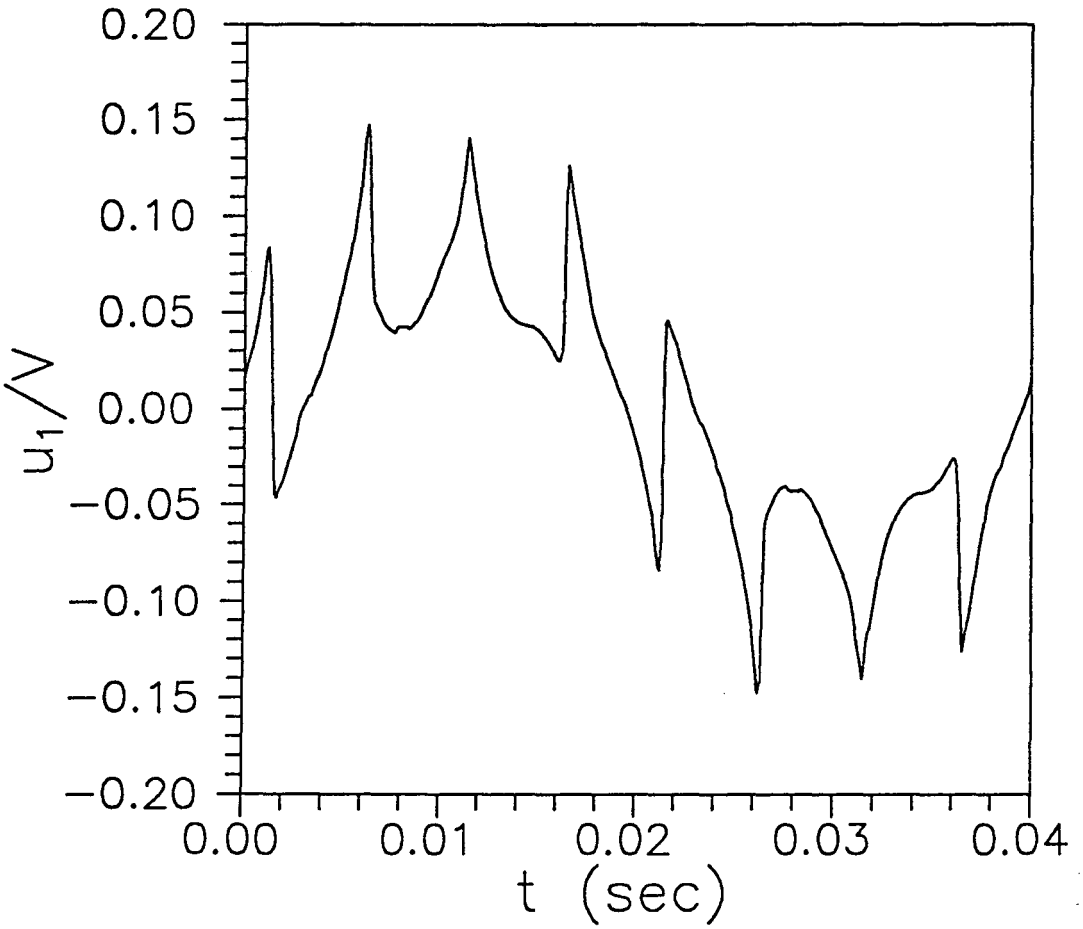

Figure 59. Induced Velocity Ratio in X-direction at 75 % Radial Station of Back Propeller During One Blade Revolution; J=2.67.

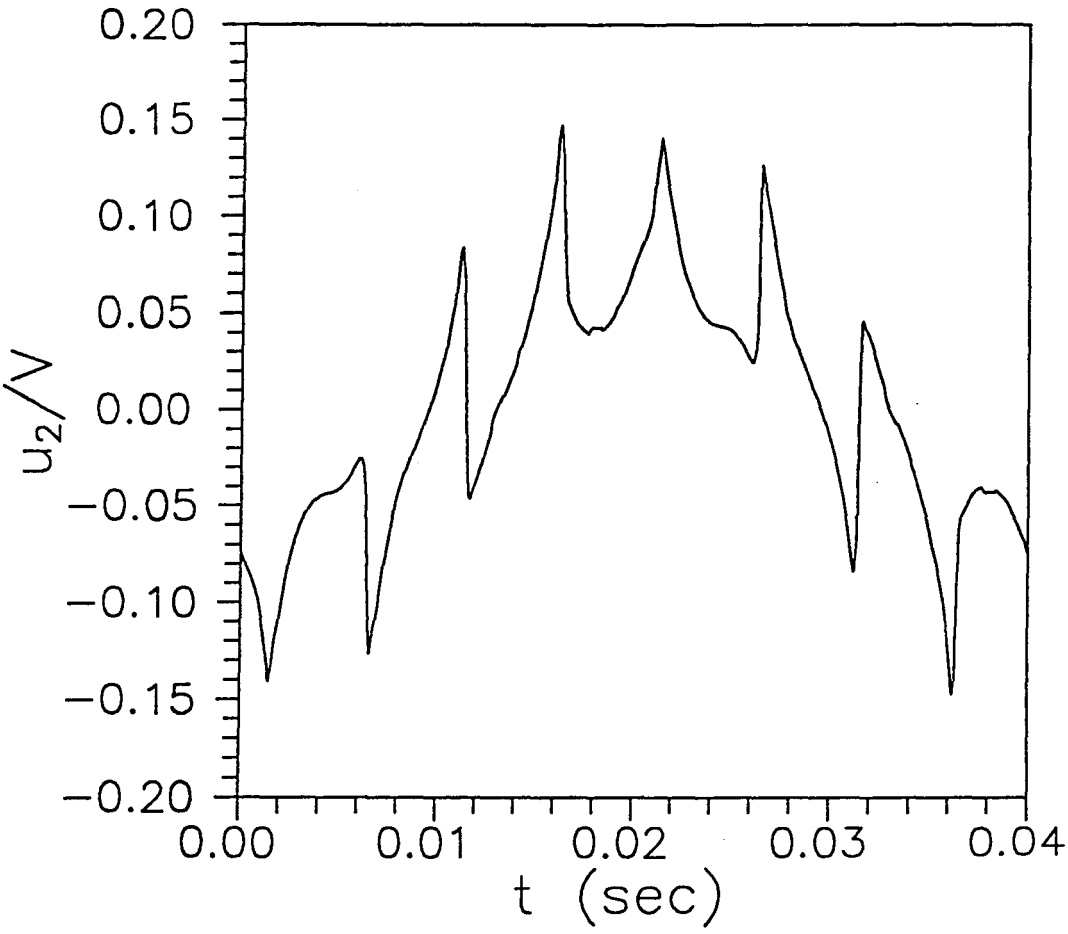

Figure 60. Induced Velocity Ratio in Y-direction at 75 % Radial Station of Back Propeller During One Blade Revolution; J=2.67.

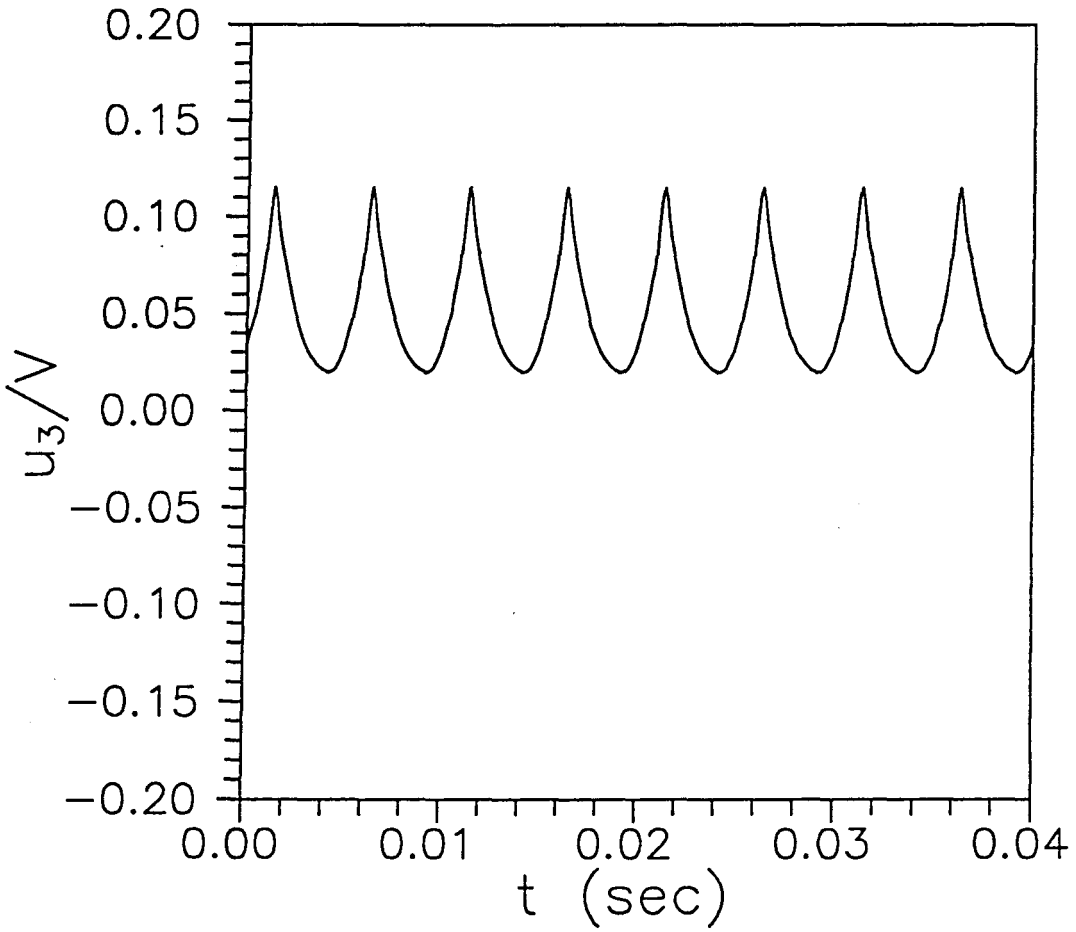

Figure 61. Induced Velocity Ratio in Z-direction at 75 % Radial Station of Back Propeller During One Blade Revolution; J=2.67.

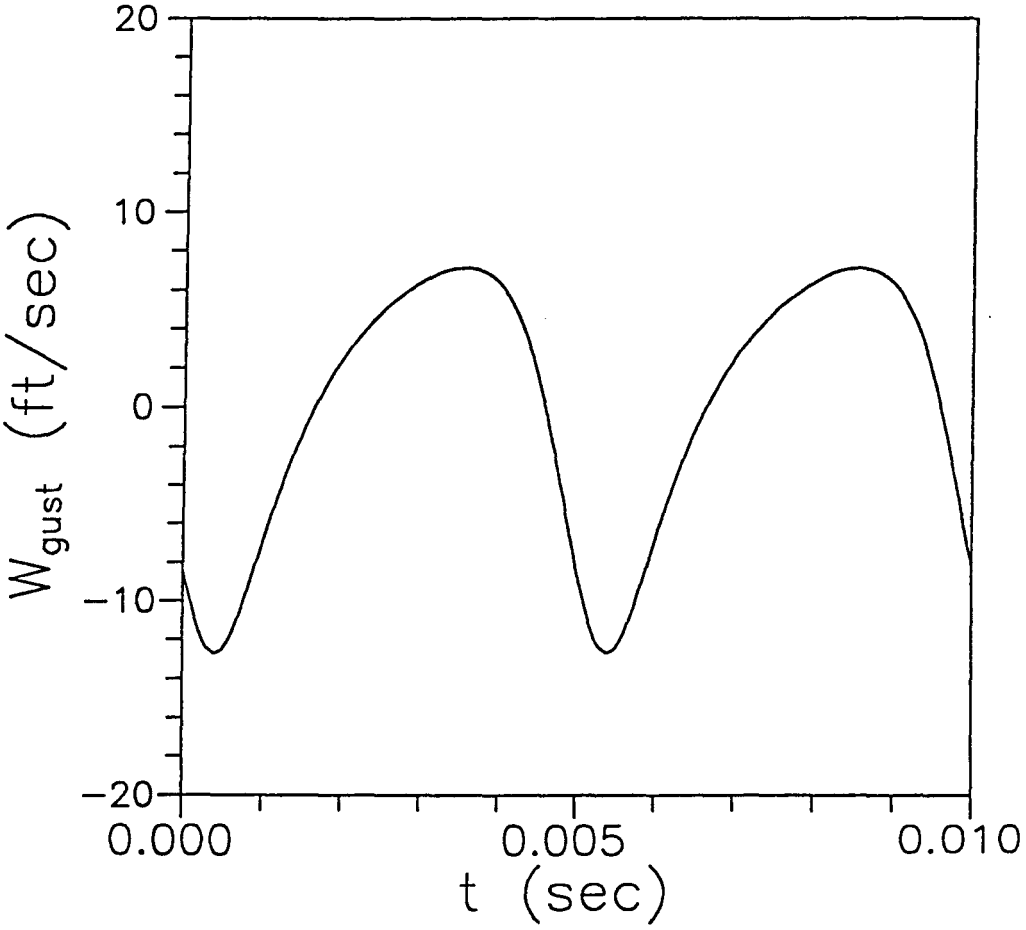

Figure 62. Vertical Gust Velocity at 75 % Radial Station of Front Propeller During One Blade Passing Period.

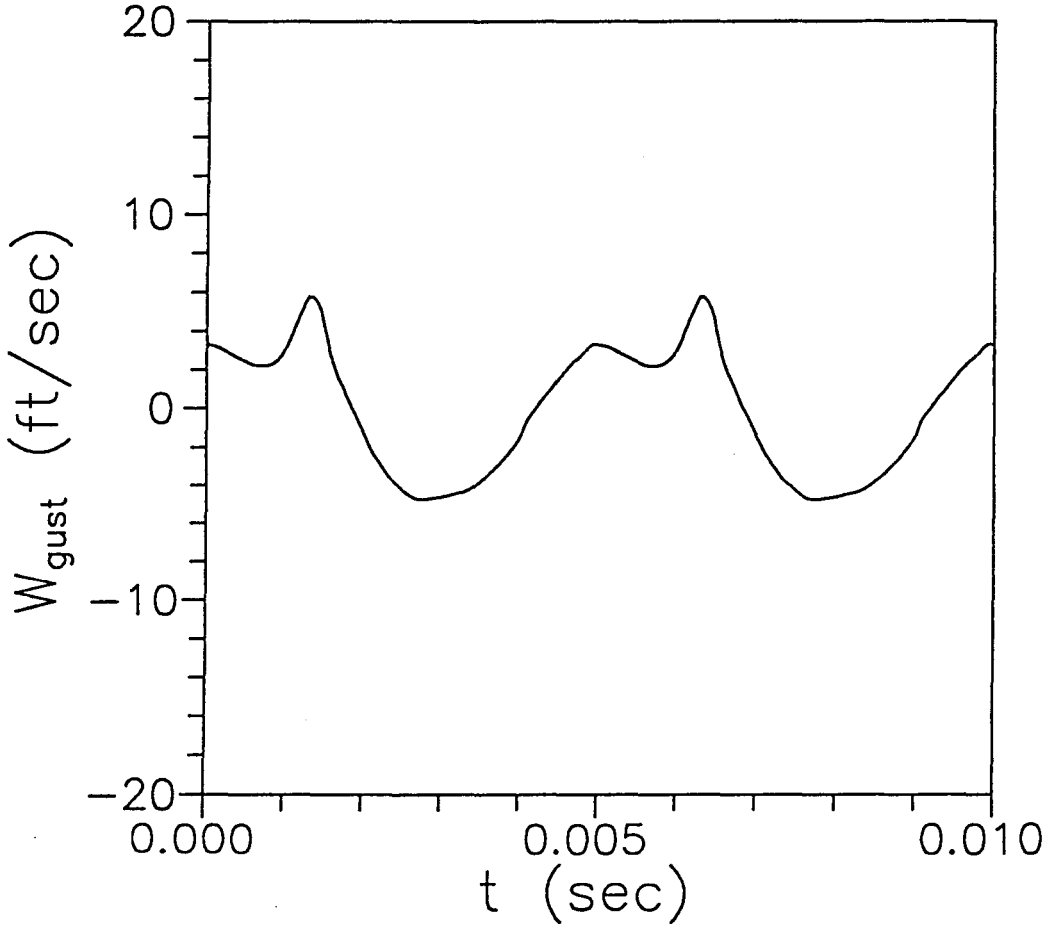

Figure 63. Vertical Gust Velocity at 75 % Radial Station of Back Propeller During One Blade Passing Period.

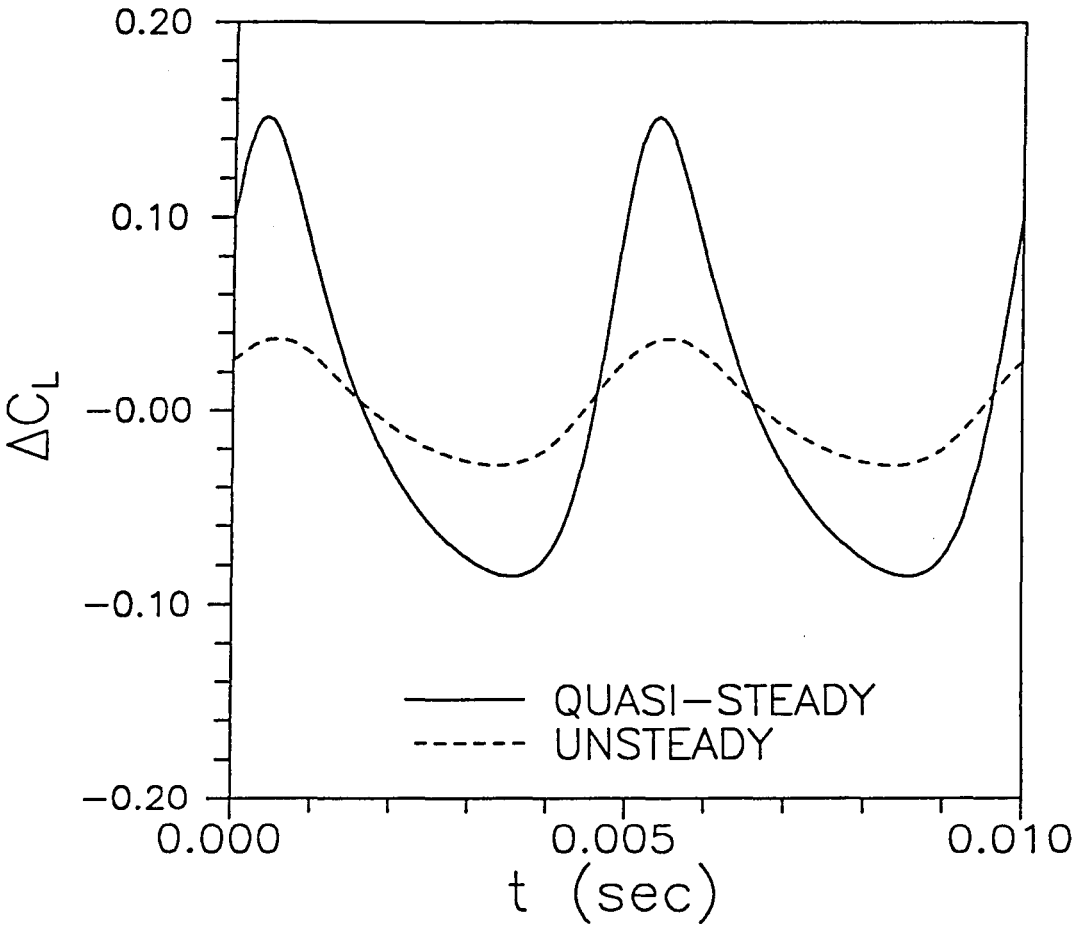

Figure 64. Quasi-Steady and Unsteady Lift Coefficient at 75 % Radial Station of Front Propeller During One Blade Passing Period.

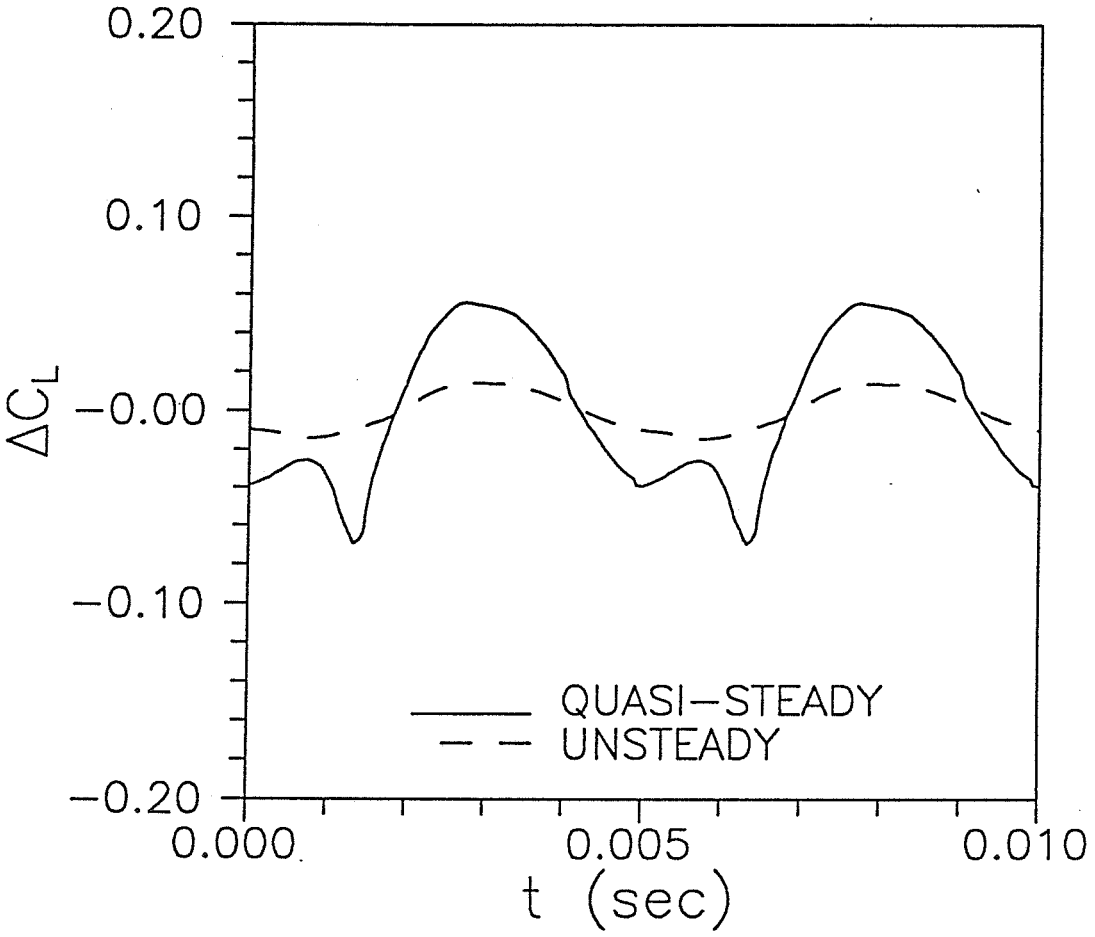

Figure 65. Quasi-Steady and Unsteady Lift Coefficient at 75 % Radial Station of Back Propeller During One Blade Passing Period.

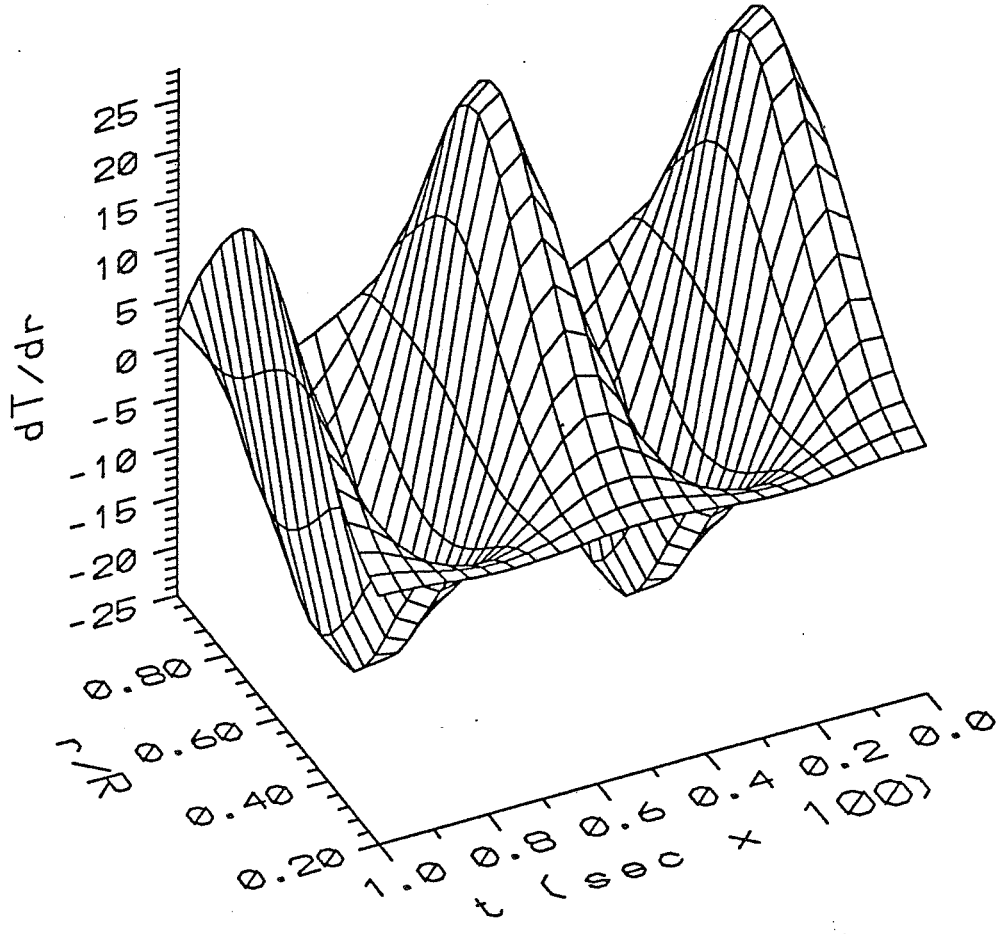

Figure 66. Radial Variation of Differential Thrust on Front Propeller Blade During One Blade Passing Period.

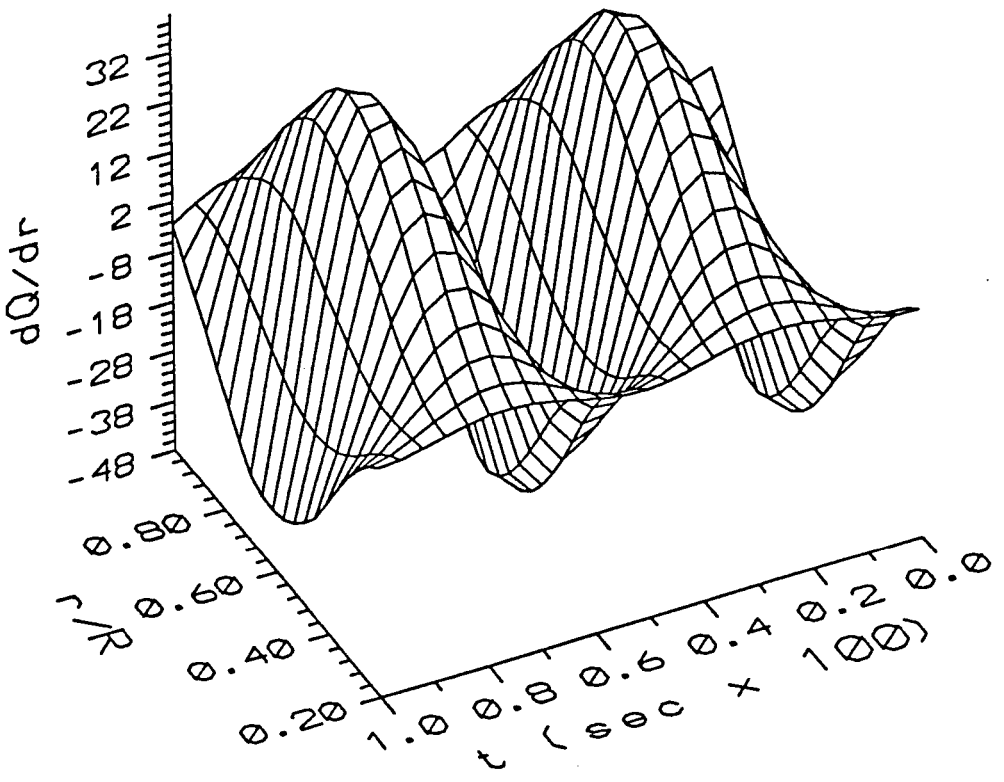

Figure 67. Radial Variation of Differential Torque-Force on Front Propeller Blade During One Blade Passing Period.

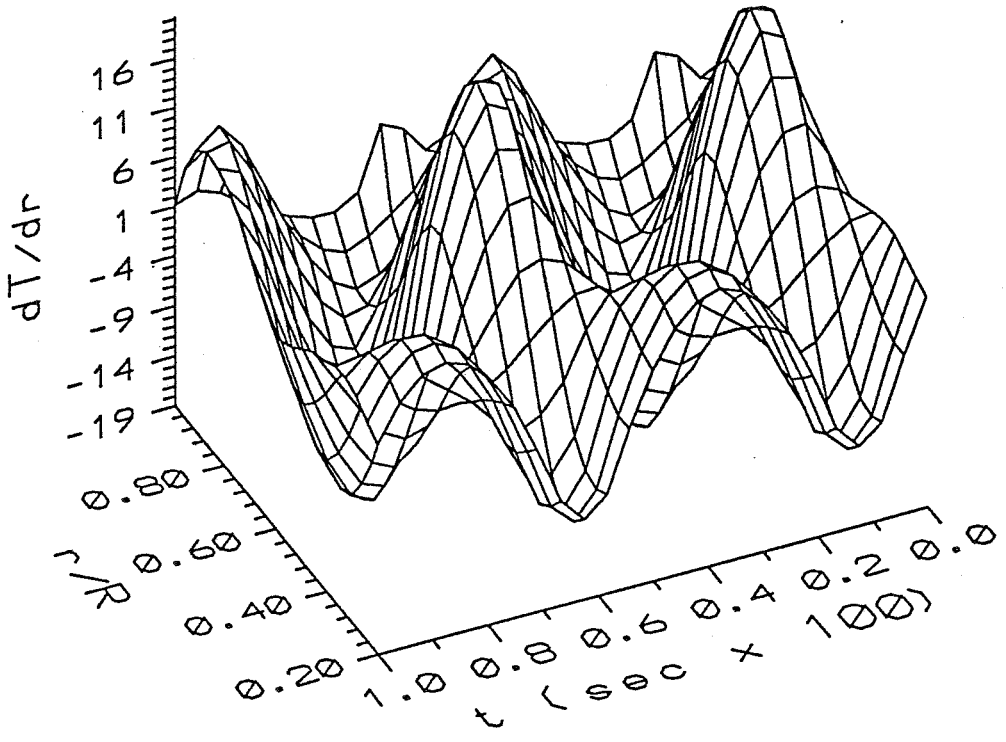

Figure 68. Radial Variation of Differential Thrust on Back Propeller Blade During One Blade Passing Period.

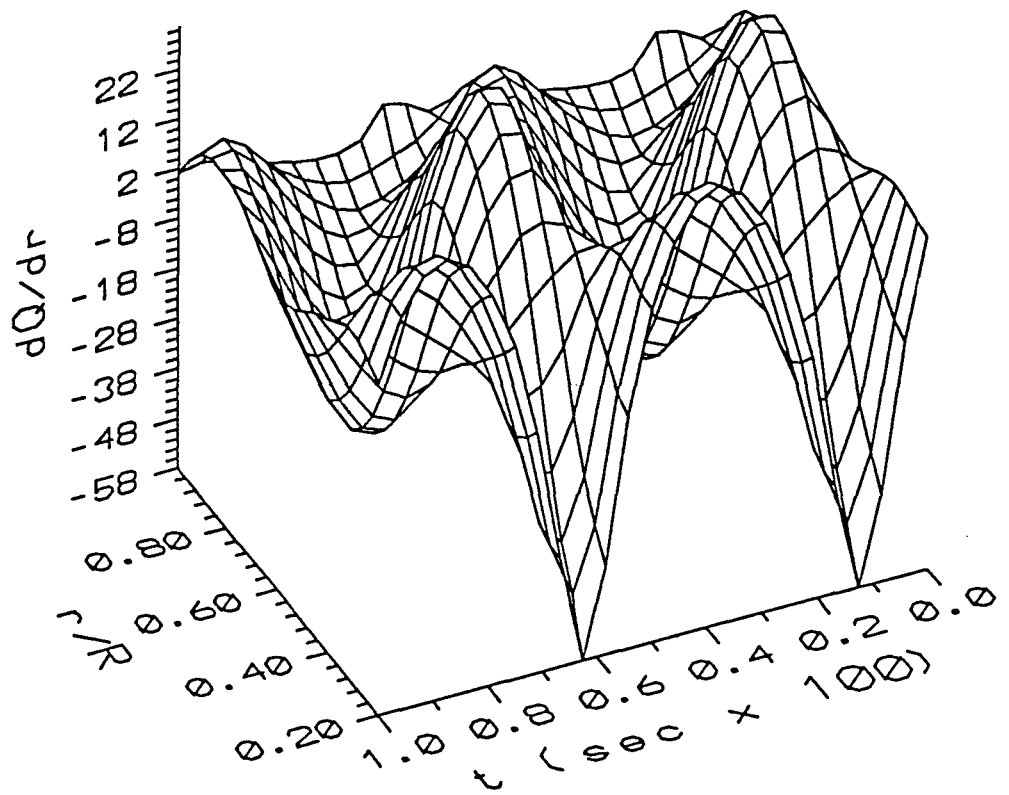

Figure 69. Radial Variation of Differential Torque-Force on Back Propeller Blade During One Blade Passing Period.

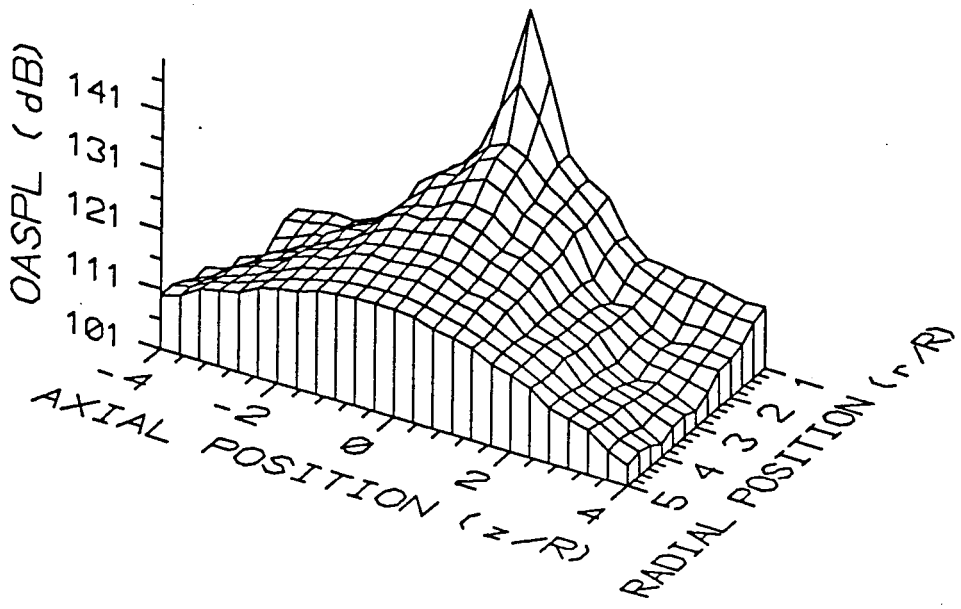

Figure 70. OASPL in Region Near the Configuration from One To Five Blade Radii Radially, and from Four Blade Radii Upstream To Four Blade Radii Downstream; J=2.13; Propeller at $(z, r) = (0, 0)$; $P_{ref} = 20\ \mu$ Pa.

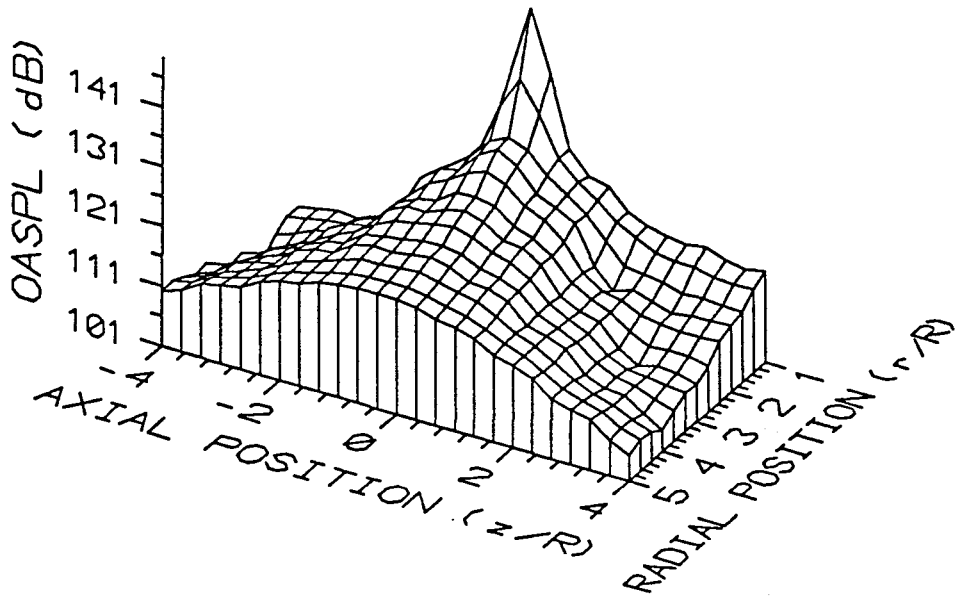

Figure 71. OASPL in Region Near the Configuration from One To Five Blade Radii Radially, and from Four Blade Radii Upstream To Four Blade Radii Downstream; J=2.67; Propeller at $(z, r) = (0, 0)$; $P_{ref} = 20\ \mu$ Pa.

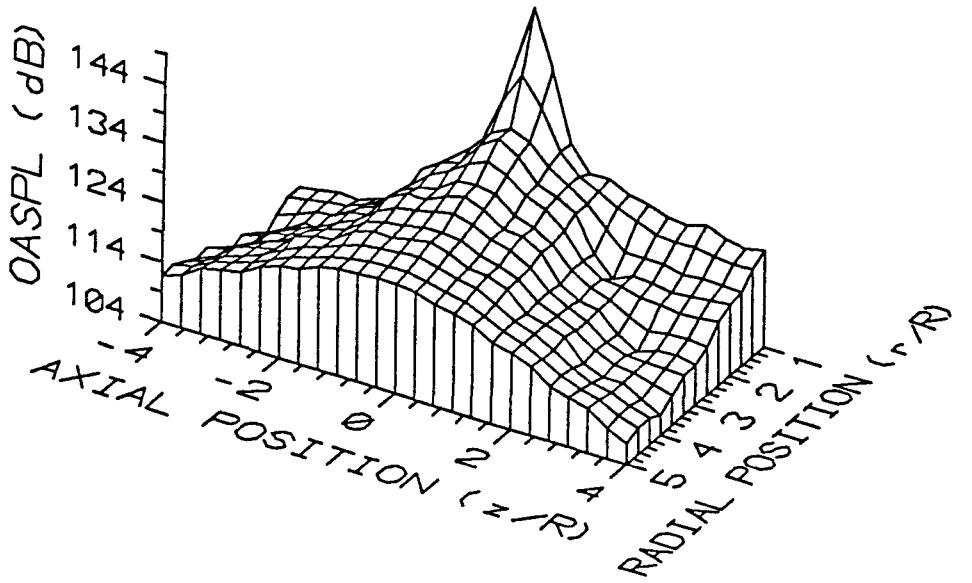

Figure 72. OASPL in Region Near the Configuration from One To Five Blade Radii Radially, and from Four Blade Radii Upstream To Four Blade Radii Downstream; J=3.20; Propeller at $(z, r) = (0, 0)$; $P_{ref} = 20\ \mu$ Pa.

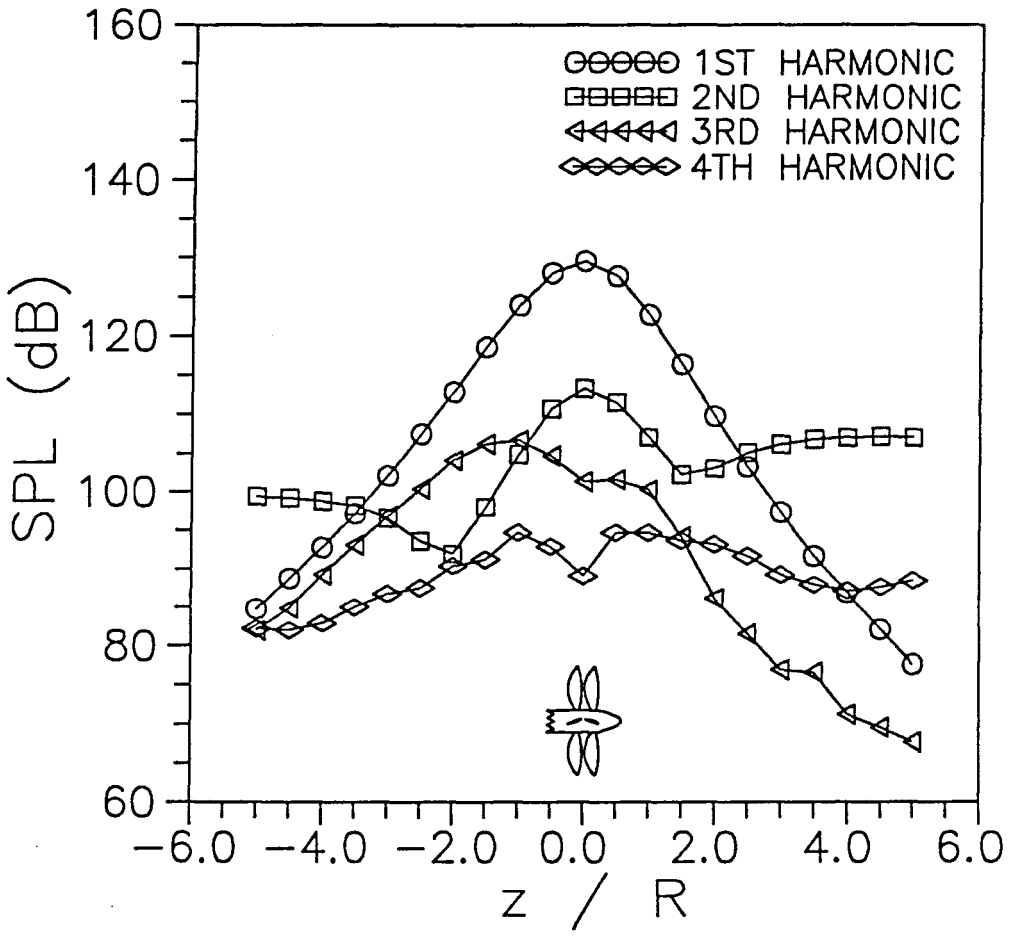

Figure 73. First Four Harmonics Along Line One Propeller Diameter from Axis of Rotation from Four Radii Upstream To Four Radii Downstream; J=2.13; P_{ref} = 20 μ Pa.

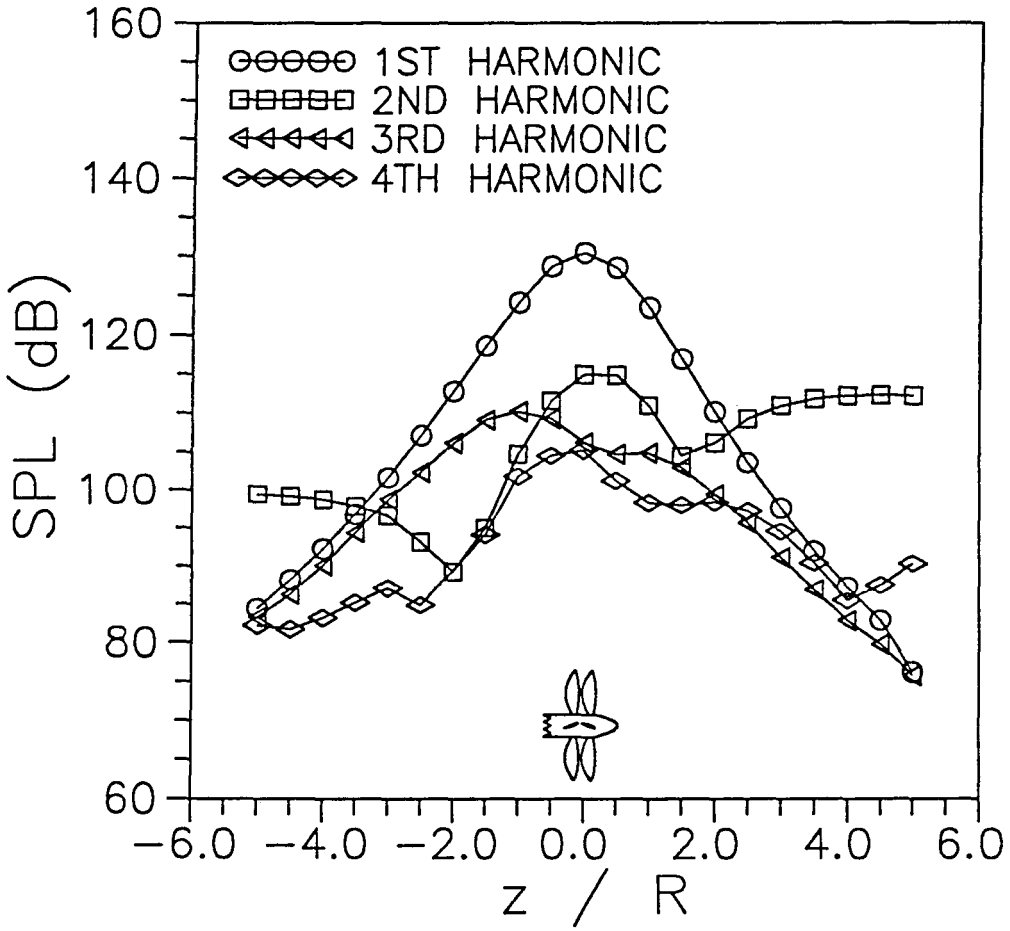

Figure 74. First Four Harmonics Along Line One Propeller Diameter from Axis of Rotation from Four Radii Upstream To Four Radii Downstream; J=2.67; P_{ref} = 20 μ Pa.

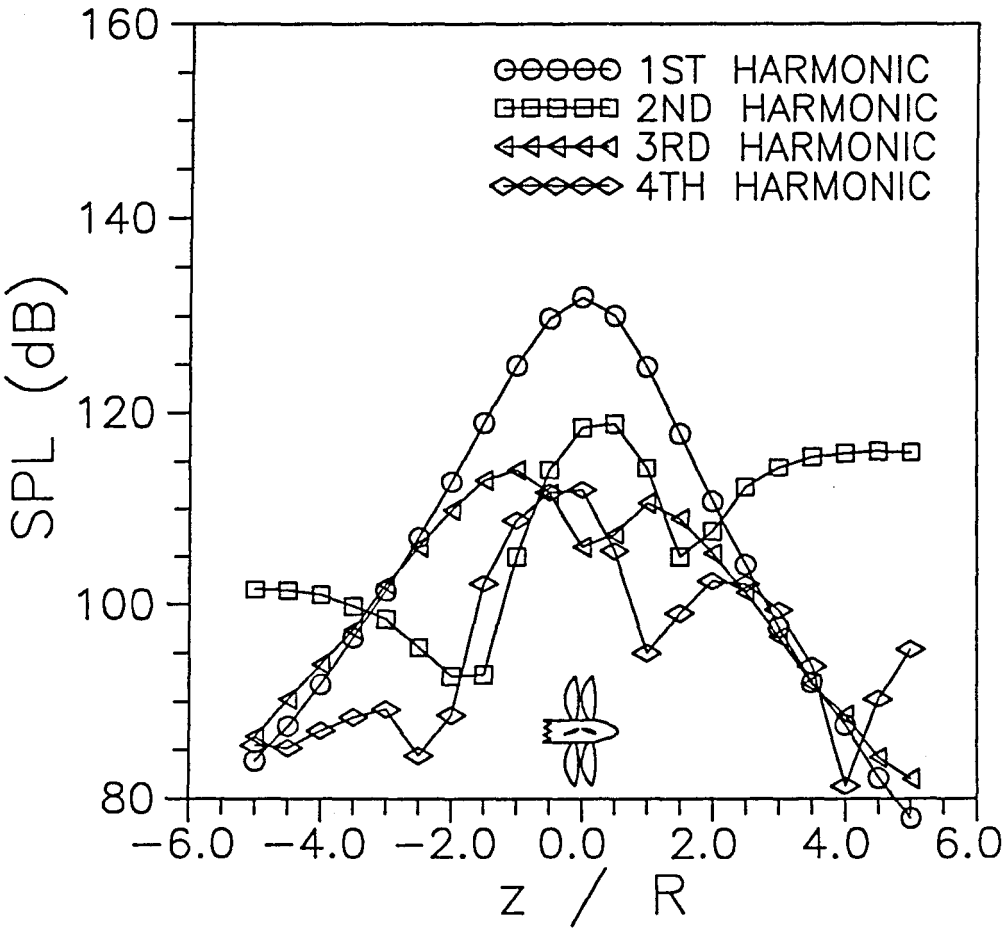

Figure 75. First Four Harmonics Along Line One Propeller Diameter from Axis of Rotation from Four Radii Upstream To Four Radii Downstream; J=3.20; P_{ref} = 20 μ Pa.

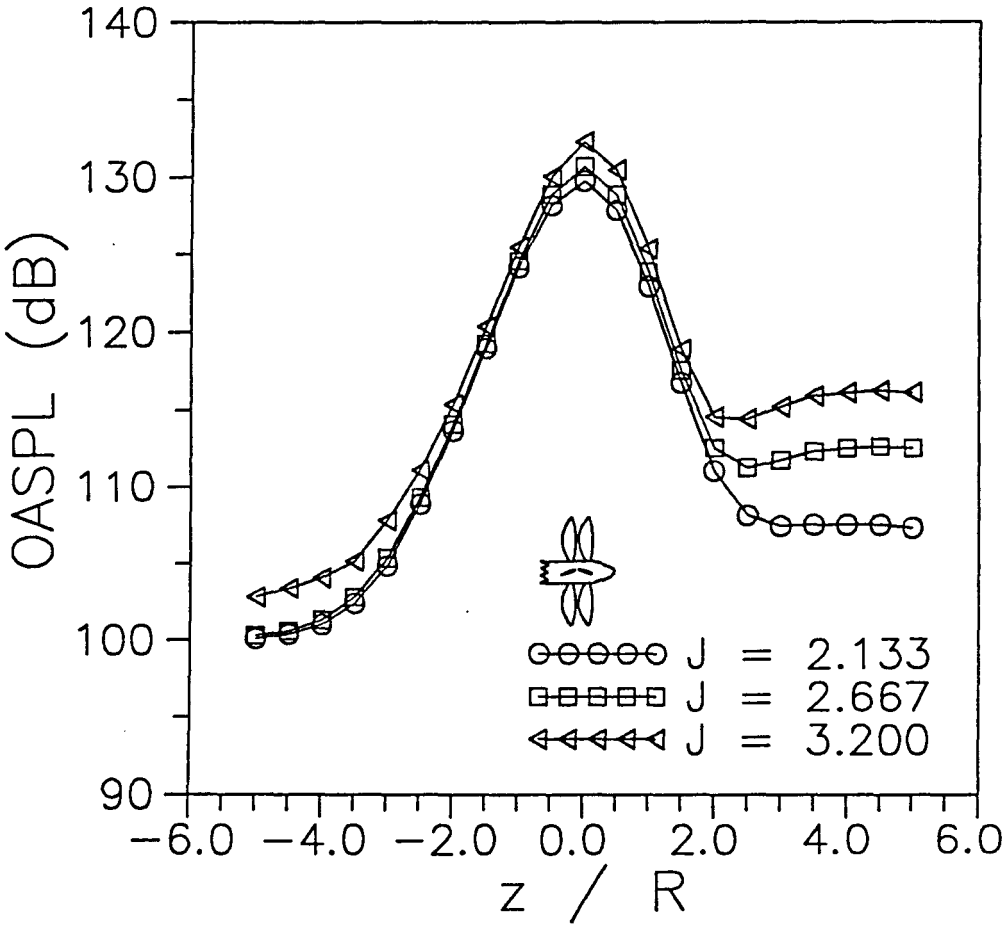

Figure 76. OASPL Along Line One Propeller Diameter from Axis of Rotation from Four Radii Upstream To Four Radii Downstream at Three Advance Ratios; $P_{ref} = 20\ \mu$ Pa.

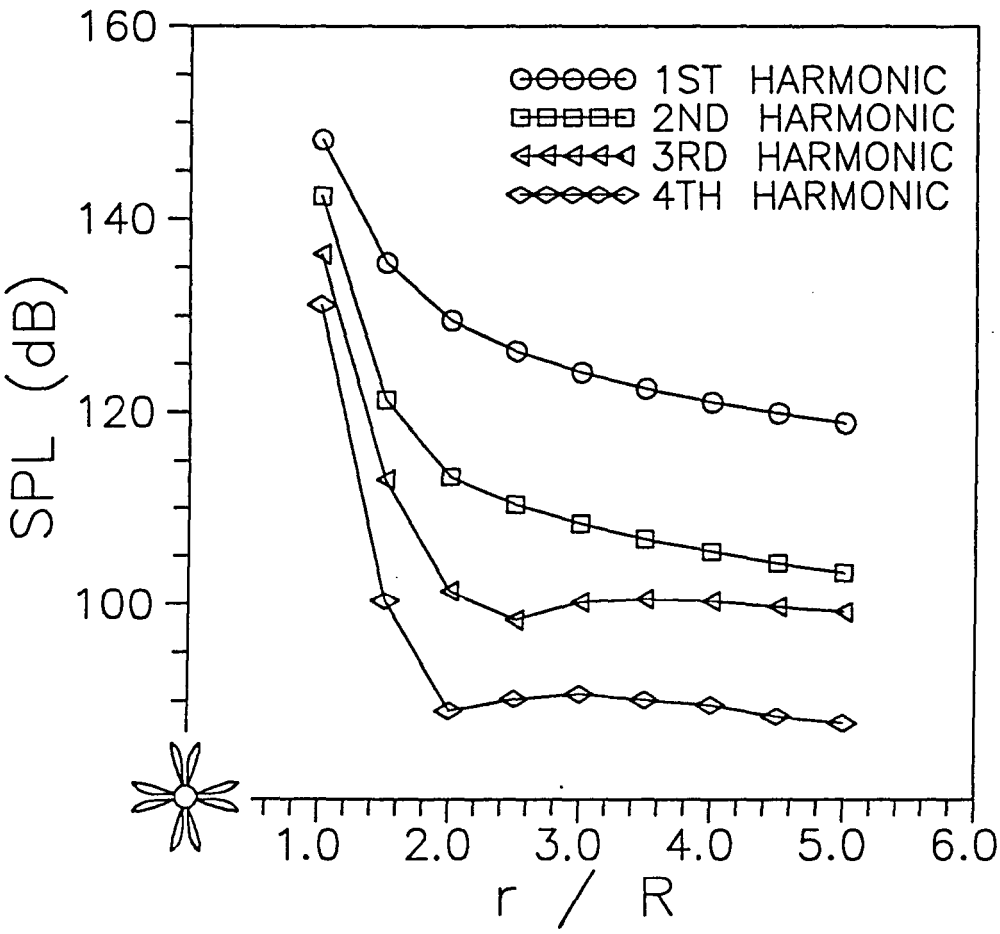

Figure 77. First Four Harmonics in the Disk Plane from One To Five Propeller Radii Distance from the Axis of Rotation; J=2.13; $P_{ref} = 20\ \mu$ Pa.

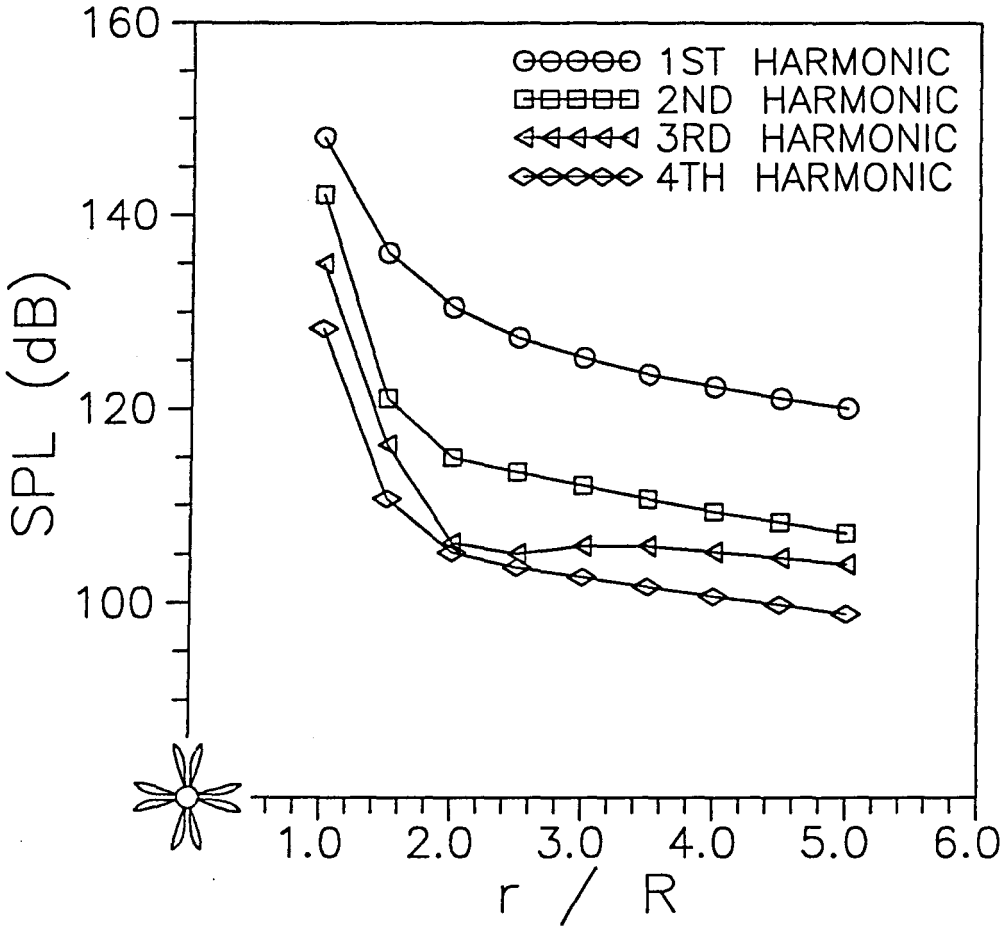

Figure 78. First Four Harmonics in the Disk Plane from One To Five Propeller Radii Distance from the Axis of Rotation; J=2.67; $P_{ref} = 20 \mu$ Pa.

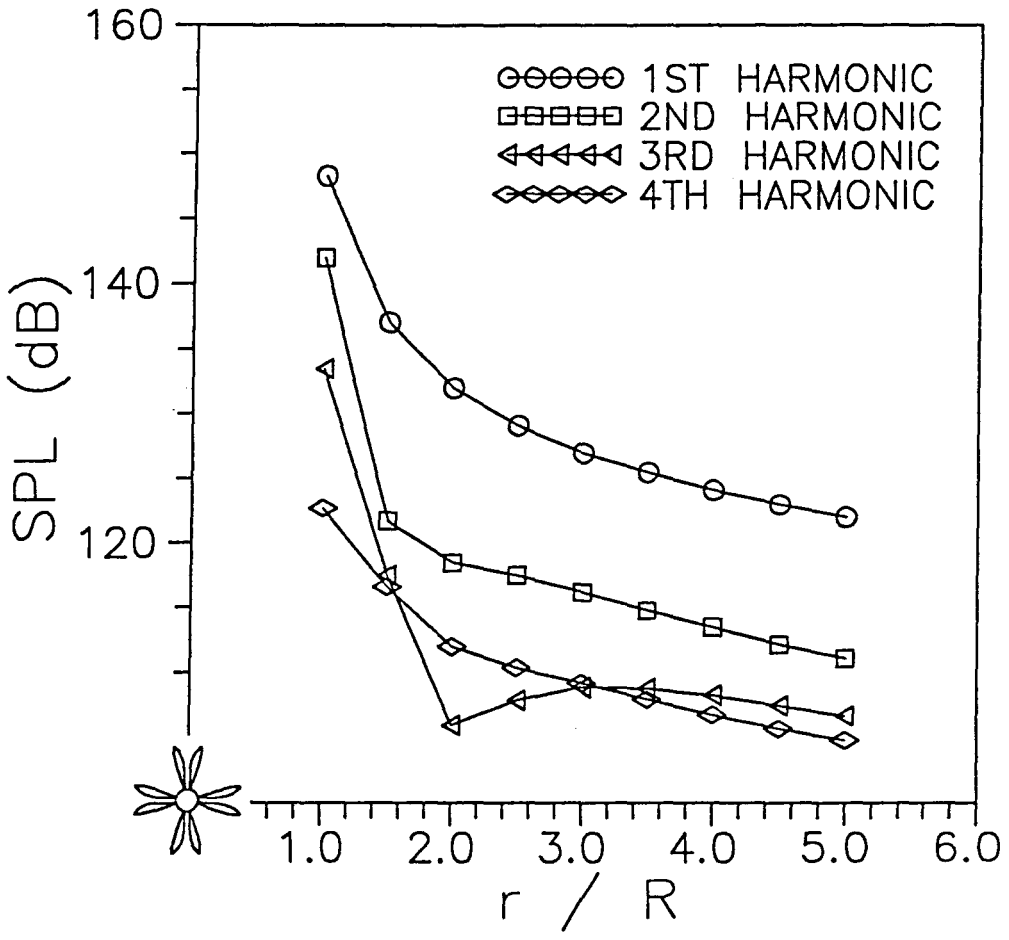

Figure 79. First Four Harmonics in the Disk Plane from One To Five Propeller Radii Distance from the Axis of Rotation; J=3.20; $P_{ref} = 20\ \mu$ Pa.

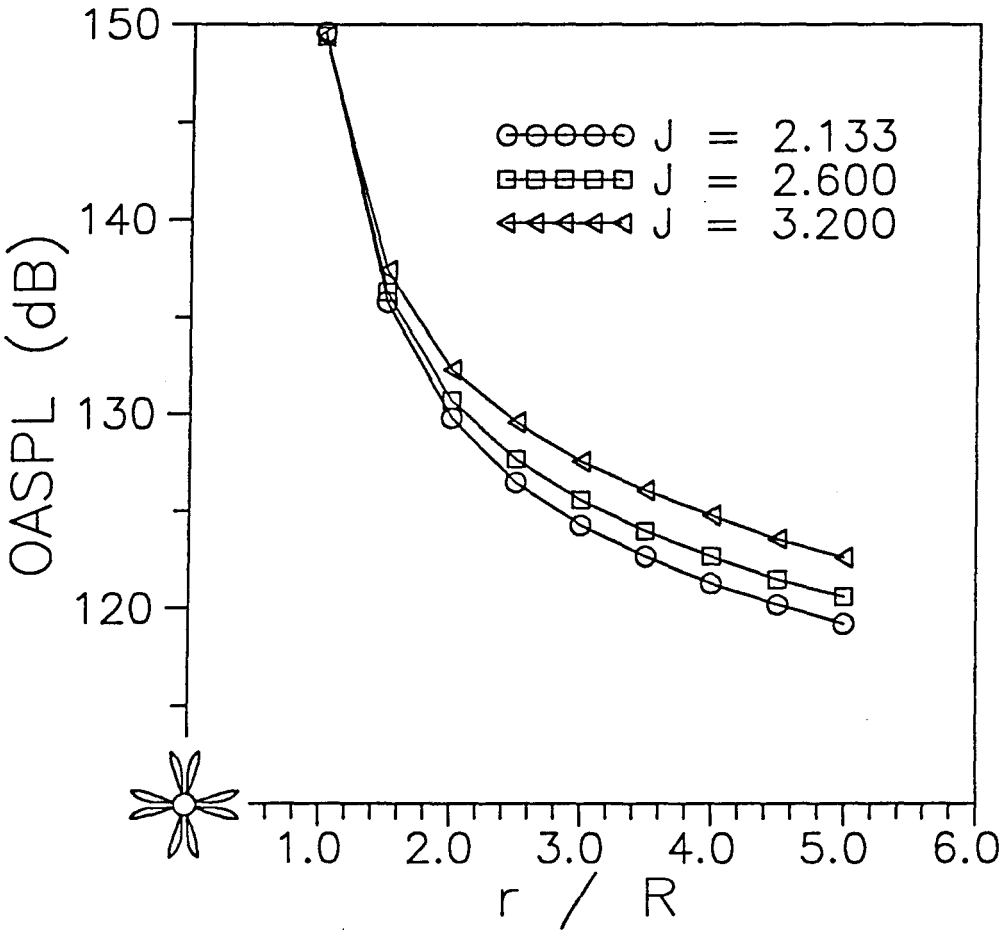

Figure 80. OASPL in the Disk Plane from One To Five Propeller Radii Distance from the Axis of Rotation; J=3.20; P_{ref} = 20 μ Pa.

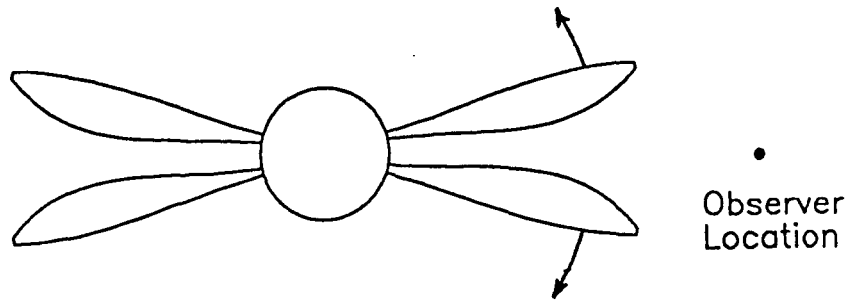

(a) In–Phase Blade Passage

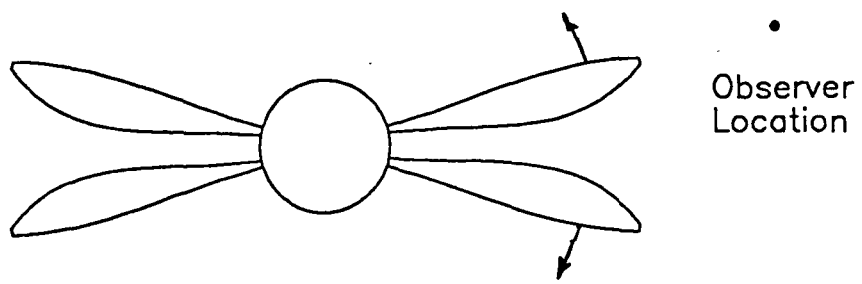

(b) Out–of–Phase Blade Passage

Figure 81. Effect of Observer Azimuthal Angle on Blade Passage Phase Relationship; $P_{ref} = 20\ \mu$ Pa.

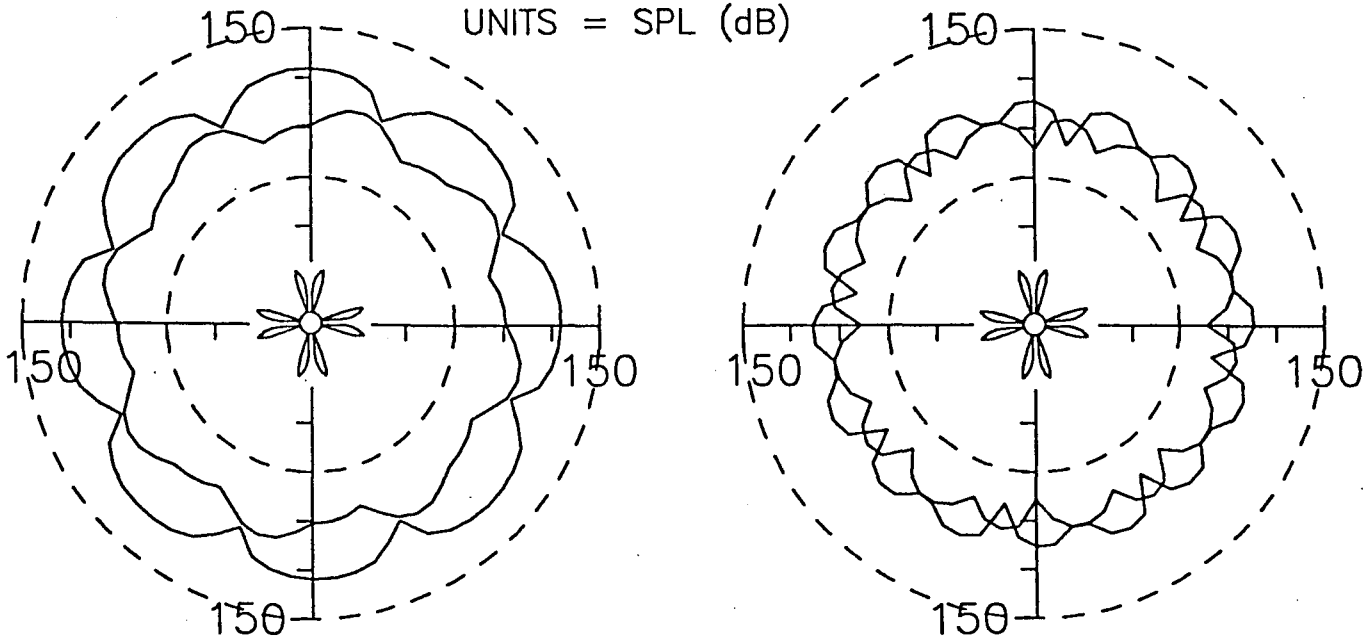

Figure 82. Azimuthal Variation of First Four Harmonics in the Disk Plane at One Propeller Diameter; J=2.13; $P_{ref} = 20\ \mu$ Pa.

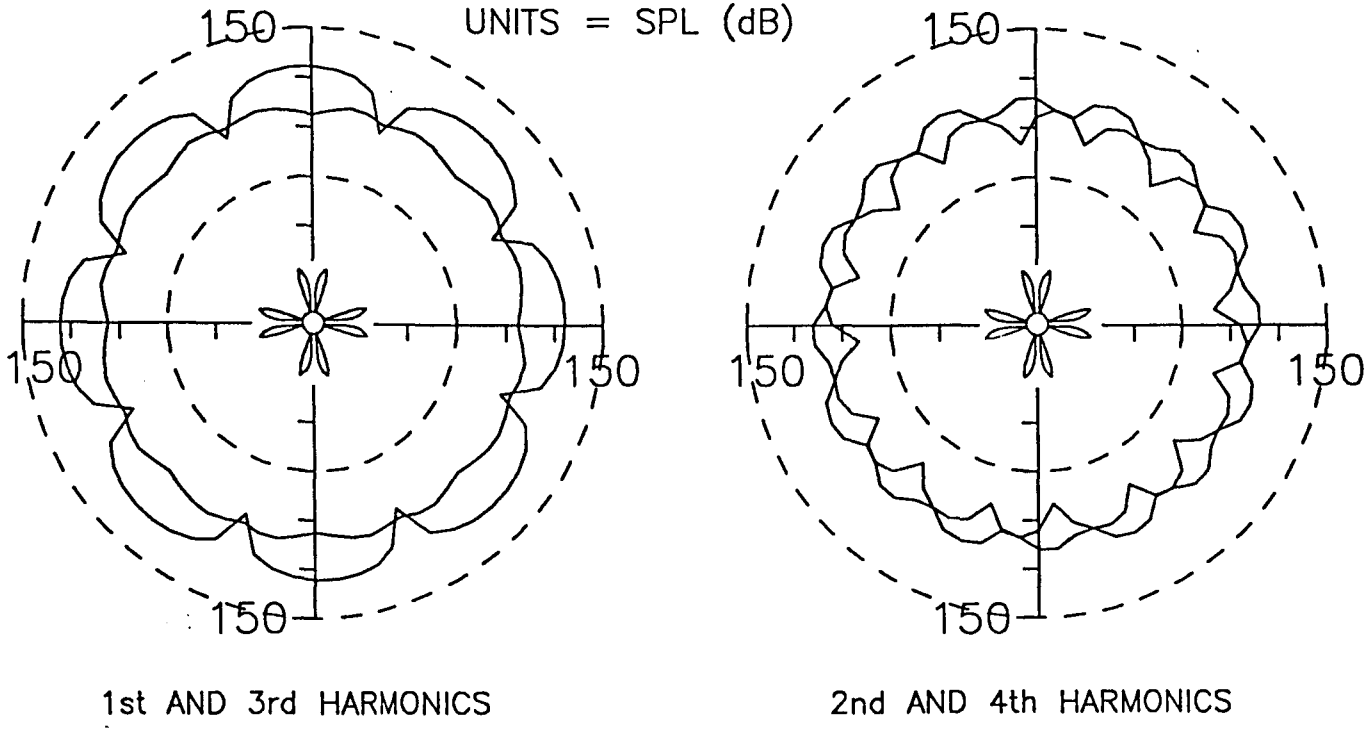

Figure 83. Azimuthal Variation of First Four Harmonics in the Disk Plane at One Propeller Diameter; J=2.67; $P_{ref} = 20\ \mu$ Pa.

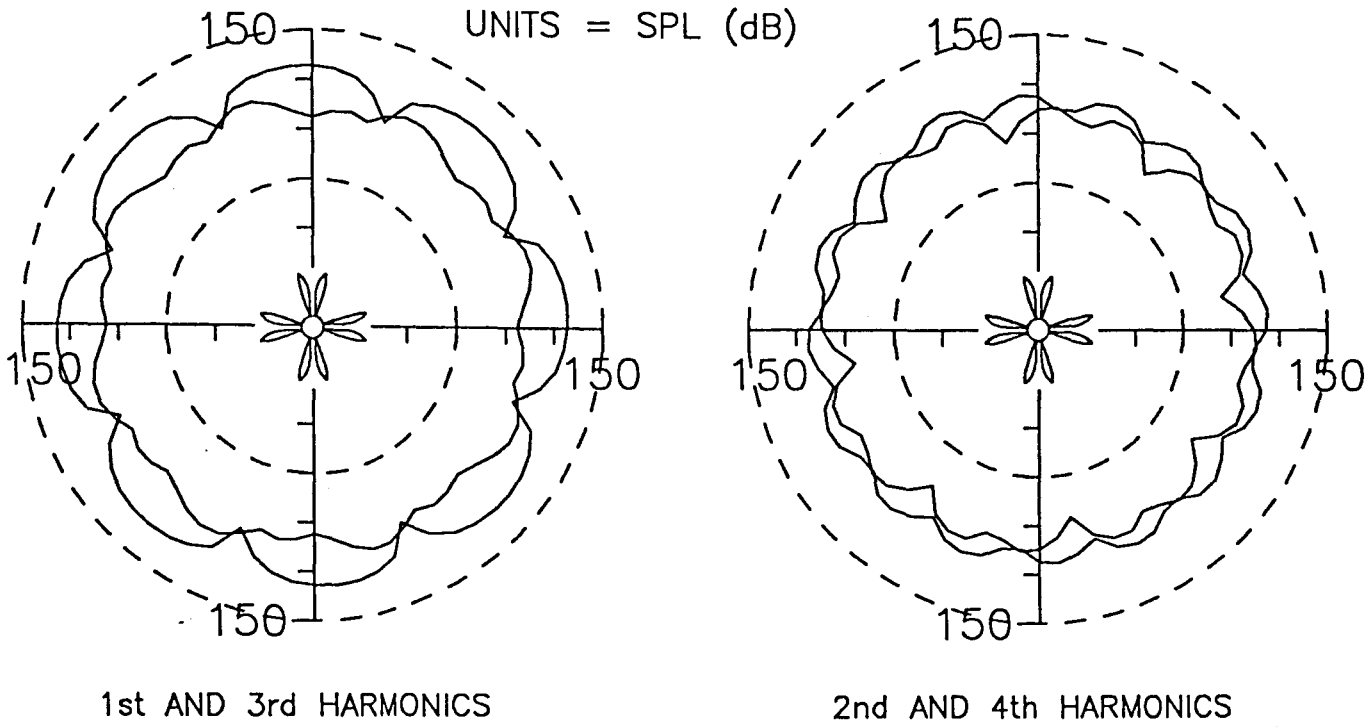

Figure 84. Azimuthal Variation of First Four Harmonics in the Disk Plane at One Propeller Diameter; J=3.20; $P_{ref} = 20\ \mu$ Pa.

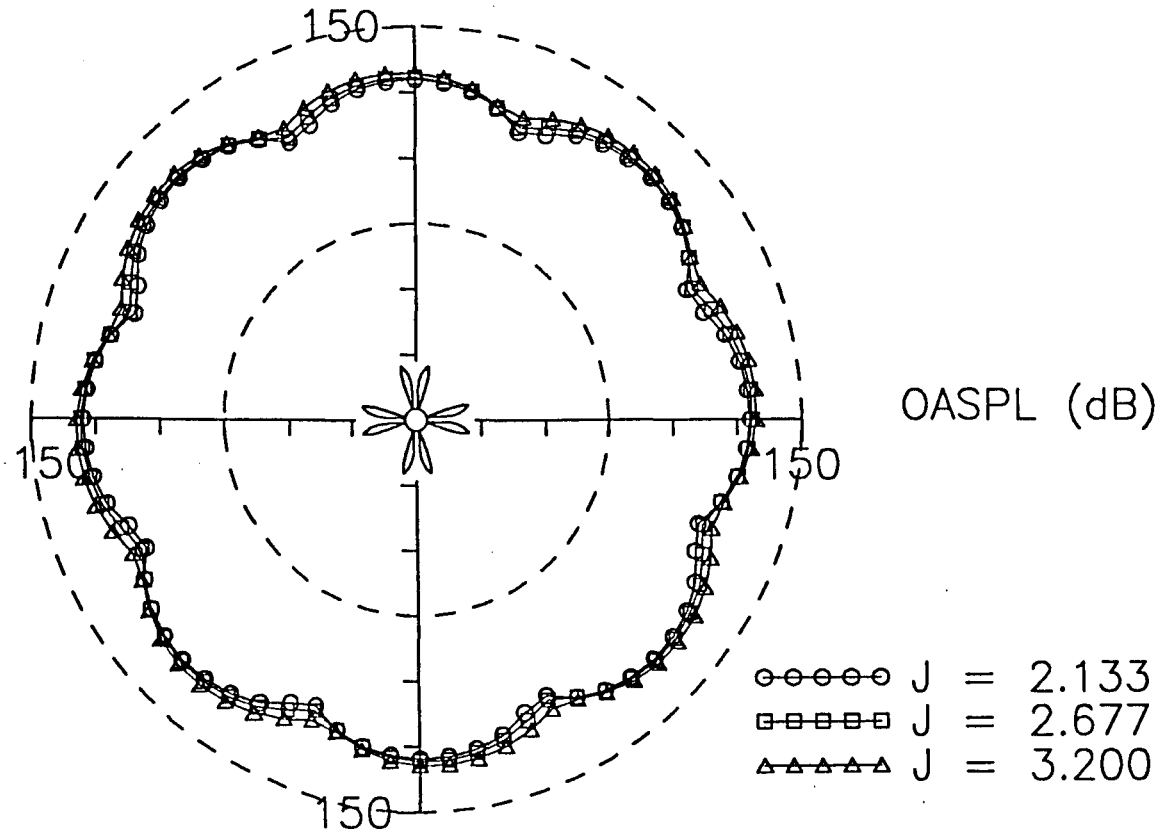

Figure 85. Azimuthal Variation of OASPL in the Disk Plane at One Propeller Diameter; $P_{ref} = 20\ \mu$ Pa.

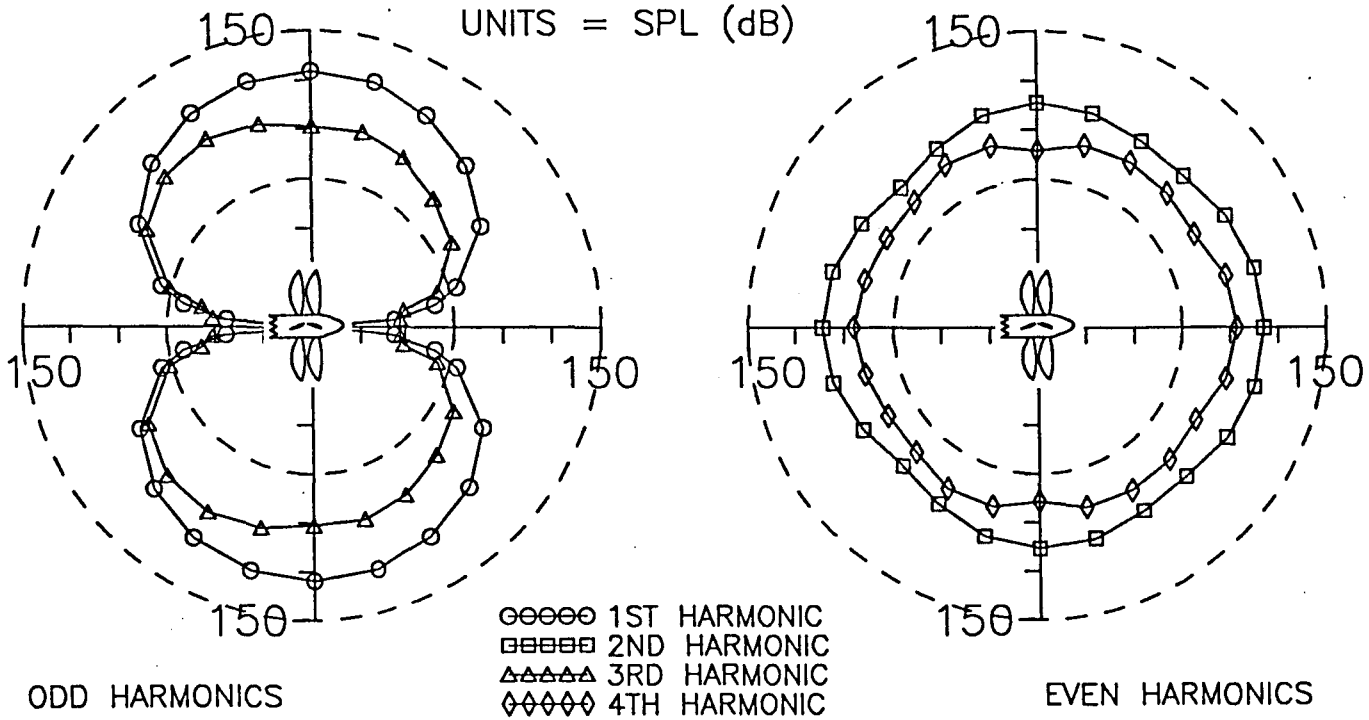

Figure 86. Azimuthal Variation of First Four Harmonics in the Horizontal Plane at One Propeller Diameter; J=2.13; $P_{ref} = 20\ \mu$ Pa.

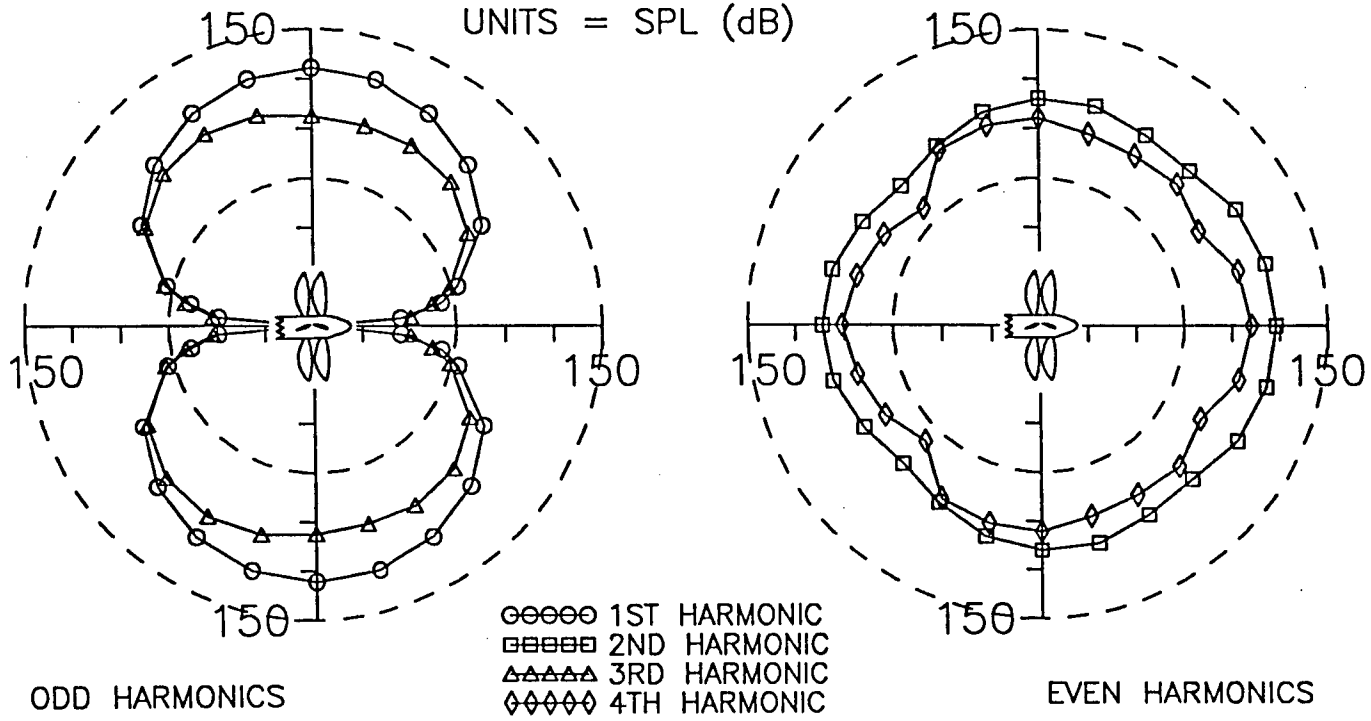

Figure 87. Azimuthal Variation of First Four Harmonics in the Horizontal Plane at One Propeller Diameter; J=2.67; $P_{ref} = 20\ \mu$ Pa.

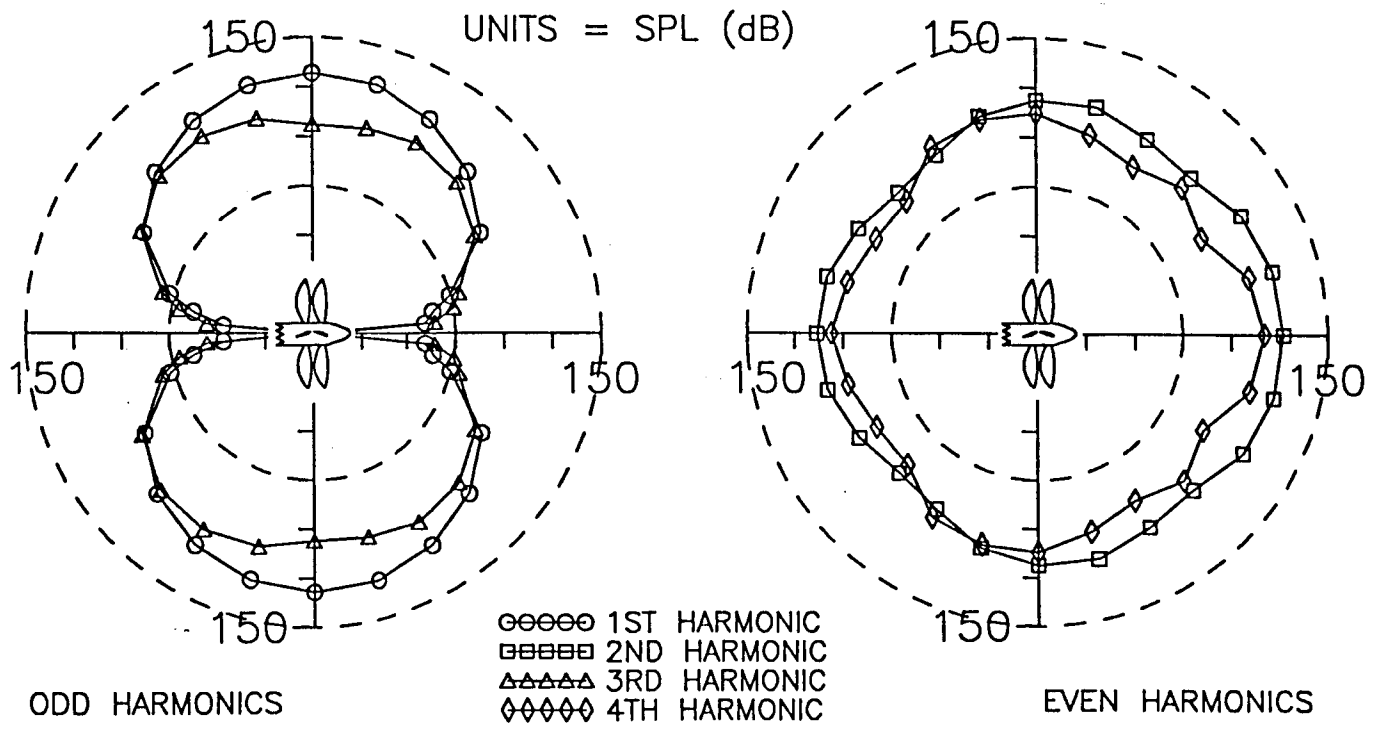

Figure 88. Azimuthal Variation of First Four Harmonics in the Horizontal Plane at One Propeller Diameter; J=3.20; $P_{ref} = 20\ \mu$ Pa.

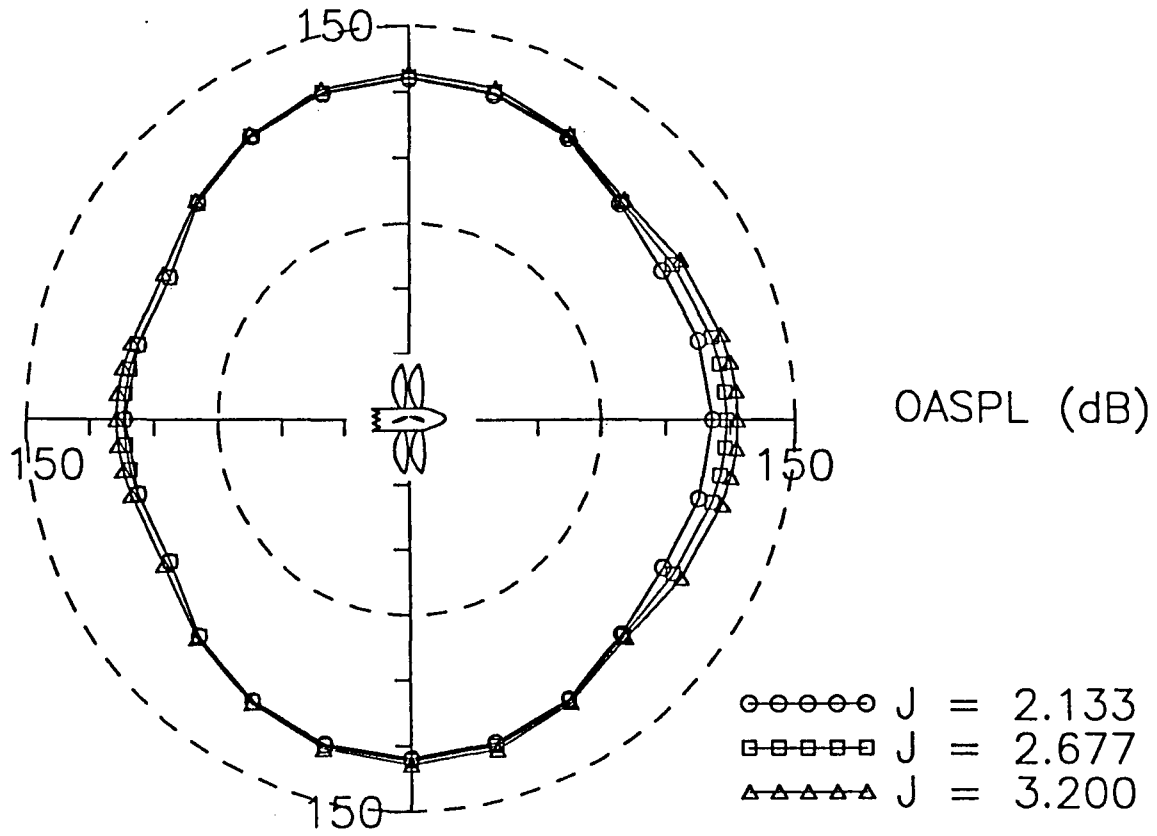

Figure 89. Azimuthal Variation of OASPL in the Horizontal Plane at One Propeller Diameter; $P_{ref} = 20\ \mu$ Pa.

VITA

Brett William Denner was born on [redacted] in [redacted], and lived in several states and foreign countries. He graduated from Burkburnett High School in Burkburnett, Texas in 1982, and entered the College of Engineering at Texas A&M University in the Fall. He received his Bachelor of Science degree in Aerospace Engineering from Texas A&M University in December, 1986.

Mr. Denner has accepted employment with General Dynamics, Fort Worth Division, and communication may be made through the following address:

4804 Threechopt Rd

Hampton, VA, 23666